1-28-2015

# Structural Elucidation of the Interaction Between Neurodegenerative Disease-Related Tau Protein with Model Lipid Membranes

Emmalee Jones

Emmalee M. Jones

*Candidate*

Nanoscience and Microsystems Engineering

*Department*

This dissertation is approved, and it is acceptable in quality and form for publication:

*Approved by the Dissertation Committee:*

Eva Chi Chairperson

Steven Graves

Andrew Shreve

Deborah Evans

**STRUCTURAL ELUCIDATION OF THE INTERACTION BETWEEN NEURODEGENERATIVE DISEASE-RELATED TAU PROTEIN WITH MODEL LIPID MEMBRANES**

**BY**

**EMMALEE M. JONES**

B.S., Applied Physics, Brigham Young University, 2009

M.S., Nanoscience and Microsystems Engineering,

University of New Mexico, 2013

DISSERTATION

Submitted in Partial Fulfillment of the

Requirements for the Degree of

Doctor of Philosophy

Nanoscience and Microsystems Engineering

The University of New Mexico

Albuquerque, New Mexico

**December, 2014**

## ACKNOWLEDGMENTS

I wish to gratefully acknowledge the support of my academic advisor, Dr. Eva Y. Chi of the Department of Chemical and Nuclear Engineering. She is an inspiring and patient mentor who has devoted many hours to me. In addition to benefitting from her own background and expertise, she has made it possible for me to work with dedicated research scientists at Los Alamos National Laboratories, Argonne National Laboratories, and HASYLAB DESY (Hamburg, Germany). These experiences and research opportunities have been very rewarding, and would not have been possible without Dr. Chi and her dedication to my education and development.

Additionally, I wish to express thanks to the committee members, Dr. Andrew Shreve, Dr. Deborah Evans and Dr. Steven Graves. Each of them is a wonderful educator, and each has taken a personal interest in me. They were very gracious in agreeing to serve as committee members.

I have also benefitted from funding and support provided by the Alzheimer's Association (NIRG-09-132478), Dr. Chi's NSF CAREER grant (CBET-1150855), the National Cancer Institute, NSF IGERT funding through the Nanoscience and Microsystems program, the Oak Ridge Associated Universities Ralph E. Powe Junior Faculty Award to Dr. Chi, and the University of New Mexico Research Allocation Committee.

My sincere appreciation also goes to my fellow members, past and present, of the Chi Research Group. It has been a pleasure to work with each of them.

And finally to my family. I really couldn't do this without you.

**STRUCTURAL ELUCIDATION OF THE INTERACTION BETWEEN NEURODEGENERATIVE DISEASE-RELATED TAU PROTEIN WITH MODEL LIPID MEMBRANES**

**by**

**Emmalee M. Jones**

**B.S., APPLIED PHYSICS, BRIGHAM YOUNG UNIVERSITY, 2009**

**M.S., NANOSCIENCE AND MICROSYSTEMS ENGINEERING,**

**UNIVERSITY OF NEW MEXICO, 2013**

**DOCTOR OF PHILOSOPHY**

**NANOSCIENCE AND MICROSYSTEMS ENGINEERING**

**THE UNIVERSITY OF NEW MEXICO**

**ALBUQUERQUE, NEW MEXICO**

## ABSTRACT

A protein's sequence of amino acids determines how it folds. That folded structure is linked to protein function, and misfolding to dysfunction. Protein misfolding and aggregation into β-sheet rich fibrillar aggregates is connected with over 20 neurodegenerative diseases, including Alzheimer's disease (AD). AD is characterized in part by misfolding, aggregation and deposition of the microtubule associated tau protein into neurofibrillary tangles (NFTs). However, two questions remain: What is tau's fibrillization mechanism, and what is tau's cytotoxicity mechanism?

Tau is prone to heterogeneous interactions, including with lipid membranes. Lipids have been found in NFTs, anionic lipid vesicles induced aggregation of the microtubule binding domain of tau, and other protein aggregates induced ion permeability in cells. This evidence prompted our investigation of tau's interaction with model lipid membranes to elucidate the structural perturbations those interactions induced in tau protein and in the membrane.

We show that although tau is highly charged and soluble, it is highly surface active and preferentially interacts with anionic membranes. To resolve molecular-scale structural details of tau and model membranes, we utilized X-ray and neutron scattering techniques. X-ray reflectivity indicated tau aggregated at air/water and anionic lipid membrane interfaces and penetrated into membranes. More significantly, membrane interfaces induced tau protein to partially adopt a more compact conformation with density similar to folded protein and ordered structure characteristic of β-sheet formation. This suggests possible membrane-based mechanisms of tau aggregation.

Membrane morphological changes were seen using fluorescence microscopy, and X-ray scattering techniques showed tau completely disrupts anionic membranes, suggesting an aggregate-based cytotoxicity mechanism. Further investigation of protein constructs and a “hyperphosphorylation” disease mimic helped clarify the role of the microtubule binding domain in anionic lipid affinity and demonstrated even “hyperphosphorylation” did not prevent interaction with anionic membranes. Additional studies investigated more complex membrane models to increase physiological relevance.

These insights revealed structural changes in tau protein and lipid membranes after interaction. We observed tau’s affinity for interfaces, and aggregation and compaction once

tau partitions to interfaces. We observed the beginnings of β-sheet formation in tau at anionic lipid membranes. We also examined disruption to the membrane on a molecular scale.

## TABLE OF CONTENTS

## LIST OF FIGURES

## LIST OF TABLES

**NOMENCLATURE**

| | |
|---|---|
| Amyloid beta | Aβ |
| X-ray reflectivity | XR |
| Neutron reflectometry | NR |
| Amyloid precursor protein | APP |
| Alzheimer's disease | AD |
| Intrinsically disordered protein | IDP |
| Paired helical filament | PHF |
| Grazing-incidence X-ray diffraction | GIXD |
| Human galectin-1 | hGal-1 |
| Cationic phenylene ethylene oligomer | OPE |
| Cationic phenylene ethylene polymer | CPE |
| Fluorescence microscopy | FM |
| Surface pressure | π |
| Scattering length density | SLD |
| Electron density | ρ |
| Liquid-condensed | LC |
| Liquid-expanded | LE |
| Radius of gyration | Rg |
| 1,2-Dimyristoyl-sn-Glycero-3-Phosphocholine | DMPC |
| Anionic 1,2-Dimyristoyl-sn-Glycero-3-[Phospho-rac-(1-glycerol)] | DMPG |
| Cationic 1,2- Dimyristoyl-3-Trimethylammonium-Propane | DMTAP |
| Zwitterionic Dipalmitoylphosphatidylcholine | DPPC |
| Texas Red 1,2-dihexadecanoyl 3-phosphoethanolamine | TR-DHPE |

| | |
|---|---|
| Microtubules | MT |
| High performance liquid chromatography | HPLC |
| Large unilamellar vesicles | LUVs |

# CHAPTER 1 INTRODUCTION

## 1.1 Intrinsically disordered proteins

### 1.1.1 *Protein structure-function paradigm*

It has long been noted that a folded protein's 3-dimensional structure determined its function. A protein consists of a sequence of amino acids; this sequence would then define how the protein will fold, and the folded structure would determine the protein's function (Daughdrill et al., 2008; Dunker et al., 2001; Dyson & Wright, 2005; Fischer, 1894; Uversky et al., 2008).

Intrinsically disordered proteins (IDPs) are a class of proteins abundant in nature which, under physiological conditions, lack stable secondary and tertiary structure (Dunker et al., 2001; Dyson & Wright, 2005; Uversky et al., 2008). IDPs challenge the long-held structure-function paradigm, as they are biologically active though intrinsically disordered. Instead, their disorder allows structural plasticity. IDPs fulfill critical functions when they transition from ordered to disordered formations upon binding to physiological partners (Daughdrill et al., 2008; Dunker et al., 2001; Dyson & Wright, 2005; Uversky & Dunker, 2010). IDPs are also found to be excessively connected to protein-associated diseases, including neurodegenerative diseases, cancers, amyloidosis, diabetes mellitus and cardiovascular diseases (Arispe et al., 1994; Demuro et al., 2005; Goedert et al., 2010; Iakoucheva et al., 2002; Khemtemourian et al., 2008; Selkoe, 2000; Soto, 2003; Uversky et al., 2008).

### 1.1.2 *Protein misfolding*

Misfolding or completely denaturing a protein can prevent it from performing its normal physiological function (Chi et al., 2008; Meredith, 2005; Soto, 2003). In addition to this loss of function, it is possible that accumulated misfolded proteins form toxic aggregates. Research has found that many neurological and systemic diseases are likely caused by such dysfunction of proteins (Clavaguera et al., 2013; Goedert et al., 2010; Meredith, 2005; Soto, 2003; Uversky et al., 2008; Walker et al., 2013). These protein conformational disorders cover a wide range, from the more common neurodegenerative diseases such as Alzheimer's disease to rare inherited diseases such as Pick's disease.

The largest group of these protein conformational disorders is related to a class of proteins known to form amyloid fibrils - highly ordered, insoluble, filamentous protein aggregates (Uversky et al., 2008). Once the proteins are converted from their functional state to the diseased fibril state, they accumulate and deposit into various organs and tissues. Protein fibrils are observed in a range of neurodegenerative disorders including Alzheimer's disease, Parkinson's disease, amyotrophic lateral sclerosis (ALS), Huntington's disease, and prion diseases (Figure 1.1). Although the specific protein involved differs, misfolding and aggregation of protein is present in all cases (Soto, 2003).

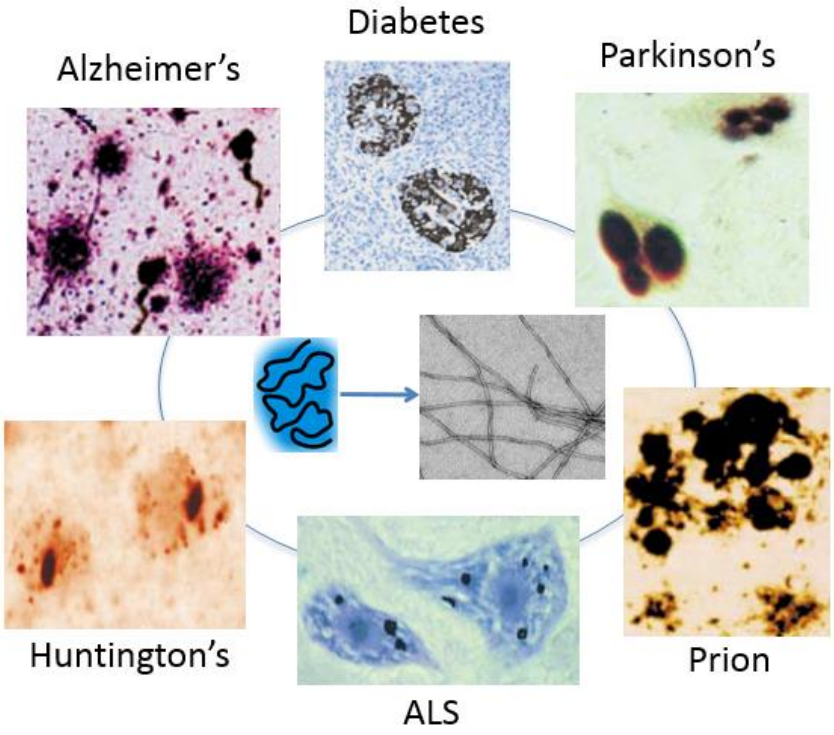


Figure 1.1 Aggregates in neurodegenerative diseases.

Protein aggregates are found in many diseases. Extracellular amyloid plaques and intracytoplasmic neurofibrillary tangles are pathological hallmarks of Alzheimer's disease. In spite of the different protein compositions across the range of diseases, the ultrastructure of these deposits seems to be similar and composed mainly of a network of fibrillar polymers (center) (Soto, 2003).

## 1.2 Alzheimer's disease as a representative protein misfolding disorder

### 1.2.1 *Alzheimer's disease*

The most common protein misfolding neurodegenerative disease, Alzheimer's disease (AD), affects over 5 million people in the U.S. alone: 3-8% of those over the age of 65 and 50% of those over 85. The estimated cost of AD care in 2014 is over

$200 billion, and is expected to reach $1.1 trillion by the year 2050 ("Treatments and Research," 2014). There is currently no known cure, prevention or treatment to slow the progression of AD. Currently available prescription medications such as anti-depressants for mood or anxiolytics for anxiety treat symptoms only, without modification of the underlying neurodegenerative process ("Treatments and Research," 2014). In AD, two IDPs, amyloid beta (Aβ) and tau, aggregate to form plaques (Figure 1.1) and neurofibrillary tangles (NFTs) (Figure 1.1), respectively. β sheet-rich insoluble fibrils are known to be associated with neurodegeneration in AD (Ghanta et al., 1996; Kim et al., 2003; Kim, Muresan, Lee, & Murphy, 2004; Kim & Murphy, 2004; Kremer & Murphy, 2003; Mandelkow et al., 2007; Marx, 2007; Meredith, 2005; Soto, 2003).

### 1.2.2 *Amyloid beta and tau proteins*

Amyloid beta (Aβ) is a protein produced by the amyloid precursor protein (APP), whose main physiologic function is not well understood (Hiltunen et al., 2009). After cleavage from APP by the β- and γ-secretases, Aβ becomes an extracellular protein. Aβ denotes peptides of 36–43 amino acids. In a diseased state, Aβ proteins aggregate into amyloid plaques. These extracellular plaques have long been observed in AD (Ghanta et

al., 1996; Selkoe, 2000). The most common isoform of Aβ contains 40 residues (Figure 1.2, top) and was used exclusively in our studies. The Aβ42 isoform is more hydrophobic and the most amyloidogenic, but the central sequence KLVFFAE which most likely forms the core of the amyloid fibril also occurs in Aβ40 (De Groot, 2006).

However, the role of tau protein and its aggregates, NFTs, in AD has not been as clear as the role of Aβ. Different, and sometimes even contradictory, conclusions have been drawn (Ballatore et al., 2007). In tauopathies like AD, the equilibrium of tau is upset and unbound proteins begin to accumulate in the cytosolic environment. A number of pathogenic events may contribute to the subsequent hyperphosphorylation, misfolding and aggregation of tau. Several tau mutations, including those that can cause frontotemporal dementia with parkinsonism linked to chromosome 17 (Goedert et al., 1996), may lead to mutants which are: prone to rapid tau fibrillization (Goedert, 2005; Goedert & Jakes, 2005), more readily phosphorylated or less prone to dephosphorylation (Alonso Adel et al., 2004), or which exhibit impaired MT binding (Hong et al., 1998; Nacharaju et al., 1999). A study which found that decreasing tau levels can block Aβ-induced cognitive impairments in AD mouse models (Berger et al., 2007) exhibited that tau abnormalities alone may cause neurodegeneration, strengthening the hypothesis that tau plays a critical role in AD pathogenesis.

The tau protein (Figure 1.2, bottom) is an IDP normally involved in the stabilization of microtubules to facilitate intracellular transport. It naturally undergoes a cycle of phosphorylation and dephosphorylation as it detaches from and attaches to microtubules. Its misfolding and aggregation have been linked to over 20 diseases such as hereditary

frontotemporal dementia and parkinsonism linked to chromosome 17 (FTDP-17), collectively termed tauopathies, including AD (Lee et al., 2001).

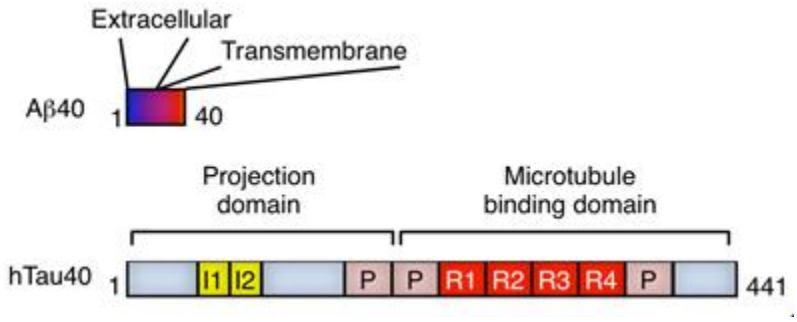


Figure 1.2 Schematics of amyloid beta (Aβ) 40 (top) and wild type tau protein (bottom).

### 1.2.3 *Tau structural compaction and membrane disruption*

The physiological factors and conditions that trigger tau misfolding and aggregation into fibrils, called paired helical filaments (PHFs), are currently unknown. The tau protein is soluble and rich in charged and hydrophilic residues which results in less likelihood of aggregate formation. In order for tau to form β-sheet rich fibrils *in vitro*, polyanionic cofactors such as heparin or anionic micelles must be introduced. This suggests that tau aggregation proceeds through a nucleation-controlled polymerization pathway. Whether the cofactors also induce conformational changes to the tau is unknown. Physiological factors which trigger tau fibrils to form *in vivo* are also unclear. We wish to address this knowledge gap.

Several lines of investigation suggest that interaction of tau with plasma membranes may be involved in tau aggregation. Research has shown tau interacts at least

indirectly with the plasma membrane through its aminoterminal projection domain (Figure 1.2, bottom) and that it is present in detergent-resistant membrane microdomains (Kawarabayashi et al., 2004; Williamson et al., 2008). Membrane glycolipids have been found to be associated with PHFs isolated from AD brains (Gray et al., 1987). More recently, membrane-associated chimeric tau has been shown to seed the formation of PHFs from full length tau protein (Campos-Pena et al, 2009), and anionic lipid vesicles have been shown to promote the aggregation of the MT binding domain of tau (K18) at sub-micromolar concentrations (Elbaum-Garfinkle et al., 2010). Thus, plasma membrane-mediated tau misfolding and aggregation may serve as an *in vivo* mechanism by which the protein nucleates and grows into PHFs. As such, even if the membrane-bound tau is only a small fraction of the protein population, it may be capable of seeding the growth of mature fibrils.

## 1.3 Lipid membranes

### 1.3.1 *Structure of biological membranes*

Physiological cell membranes form a continuous protective barrier which is selectively impermeable to the entrance of substances into and out of the cell. These membranes are complex structures composed of a phospholipid bilayer with globular proteins, receptors, transmembrane channels, and glycoproteins floating in the lipid structure (Butterfield & Lashuel, 2010) (Figure 1.3A). The membrane interacts with

structures inside and outside of the cell including the cytoskeleton, a dynamic network of protein fibers including microtubules, involved in cellular functions such as transport and structure. Because of the hypothesized link between membrane lipids and the microtubule-associated protein tau's misfolding and aggregation, we wish to investigate the membrane's interaction with tau.

(A)

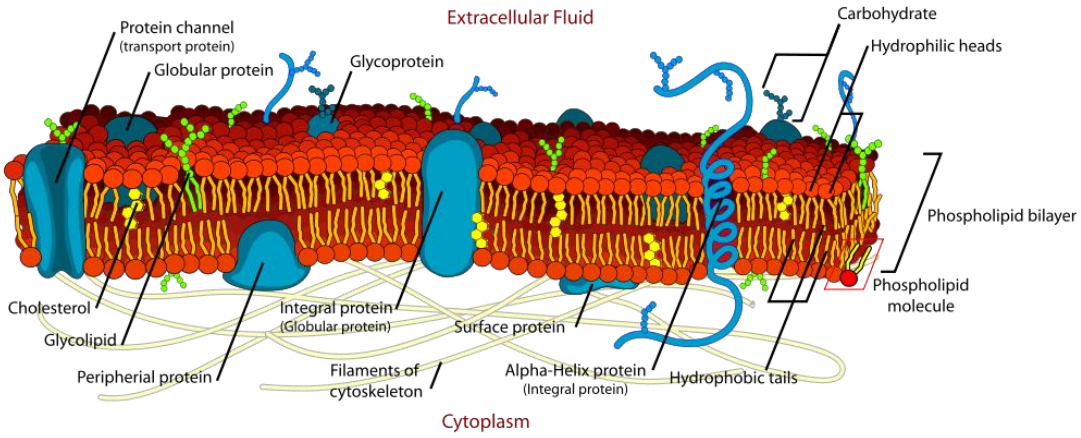


(B)

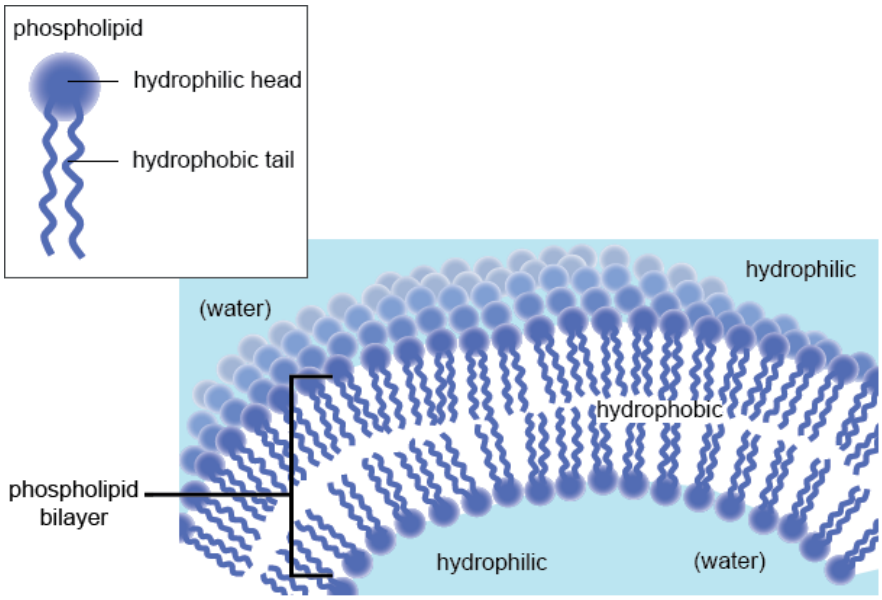


Figure 1.3 (A) Illustration of a biological cell membrane including many of its complexities (Skou, 1965) and (B) basic schematic of a phospholipid bilayer (Team, 2008) with inset of individual phospholipid.

Due to the inherent complexity of cell membranes, researchers commonly employ simplified model lipid membranes (Figure 1.3B) in their experiments wherein components of the system can be individually modified and tested. A simplified membrane consisting of either a lipid monolayer or bilayer, as we utilized in our experiments, is formed from pure phospholipids. Phospholipids are amphiphilic and consist of two main regions, the hydrophilic phosphate group "head" and the hydrophobic fatty acid "tails" (Figure 1.4A). The head contains a choline, phosphate and glycerol group while the tail is composed of two hydrocarbon chains. Because of their amphiphilic nature, in an aqueous environment phospholipids spontaneously form structures which limit the contact of the hydrophobic tails with water, either micelles (single layer spheres) or bilayers (two layer spheres and films) (Skou, 1965). Formation of these structures shields the hydrophobic tails from contacting the aqueous environment and exposes the hydrophilic heads to the polar water molecules. Bilayers function to separate an internal aqueous environment from the surrounding outer environment.

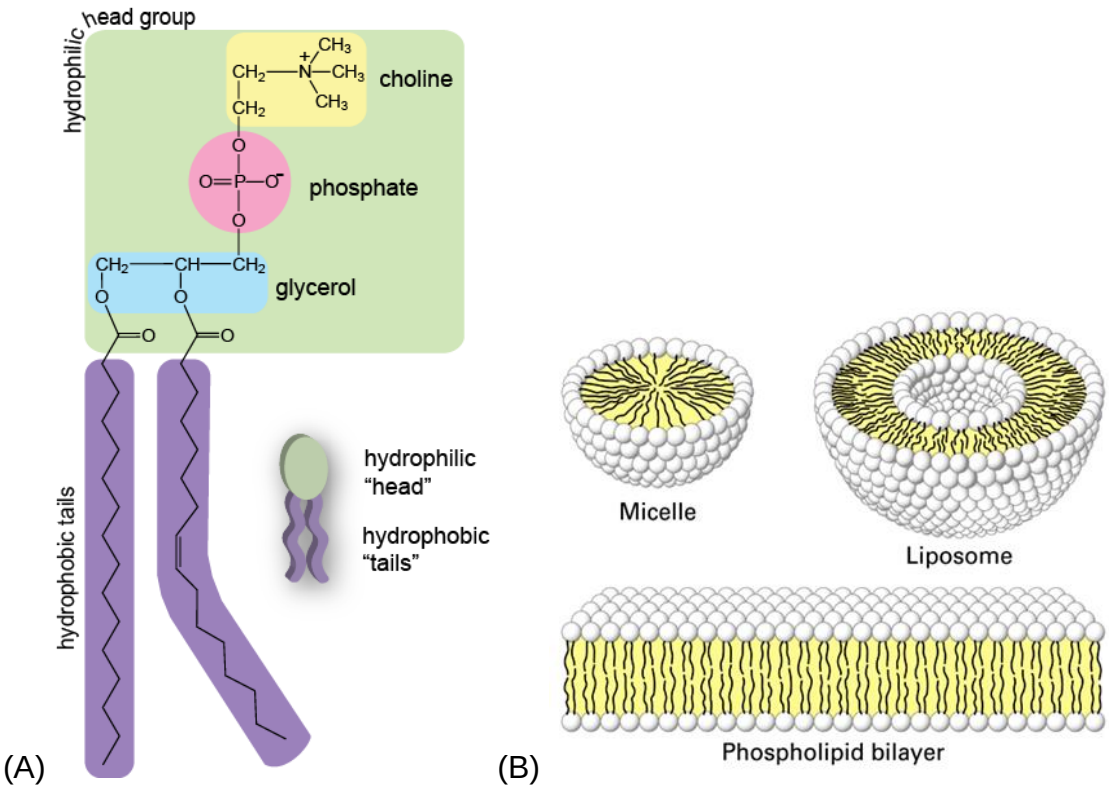


Figure 1.4 A detailed schematic of a phospholipid's basic structure and structures formed in aqueous solutions.

As illustrated in Figure 1.4, the phospholipid is composed of a hydrophilic "head" group and two hydrophobic "tails" (Team, 2008); and (B) structures formed by phospholipids in aqueous solutions (Skou, 1965).

### 1.3.2 *Properties of cell membranes*

A phospholipid bilayer cell membrane forms a semipermeable protective membrane which is permeable to lipid-soluble materials but impermeable to all but the smallest water-soluble materials. Transport of polar or ionic materials across a cell

membrane is highly regulated by specialized transport proteins located in the membrane. In general, there are three ways that material can cross a membrane. First is by diffusion, with molecules dispersing from an area of lower concentration to an area of higher concentration. Small lipid-soluble materials like $CO_2$ or $O_2$ can rapidly cross the lipid membrane in this manner. Second is by facilitated diffusion, whereby large polar molecules cross *via* specialized protein channels in response to a concentration gradient. Third is active transport, in which the cell uses energy to pump a molecule against the concentration gradient (low to high) (Skou, 1965). Disruption of cell membranes deregulates transport, ultimately leading to imbalances that cause cell death.

### 1.3.3 *Modeling cell membranes*

#### 1.3.3.1 Fluid mosaic and lipid raft models

In 1972, Singer proposed the fluid-mosaic model of cell membrane structure. In this model, the phospholipid membrane can be considered a two-dimensional fluid (Singer, 1972; Singer & Nicolson, 1972) through which lipid and protein molecules diffuse easily. Lipids are constantly moving laterally along the surface, while a large number of proteins lend more structure to the membrane. The class of integral membrane proteins pass through the bilayer to facilitate ionic transport across the membrane. Disruption of the membrane can destroy the gradient and lead to cell death. More recent membrane models extend this understanding (Korade & Kenworthy, 2008; Pike, 2008; Simon & Ehehalt, 2002). The lipid membrane is no longer seen to be a homogeneous fluid, but instead to contain lipid assemblies, or rafts, rich in cholesterol and sphingomyelin which complex with internal structures and proteins in the cell. The phospholipids within a bilayer or monolayer may

also form microdomains with varying packing density depending on lipid composition and surface pressure (Rajendran & Simons, 2005; Goodsaid-Zalduondo et al., 1982).

#### 1.3.3.2 Phospholipid phase behavior

Phase behavior of a bilayer references the relative fluidity of the bilayer's constituent lipid molecules and how this is influenced by changes in temperature and/or pressure (Silvius, 1982; Berg, 1993). This behavior of phospholipids may be modeled similarly to phase behavior when transitioning from gas to liquid to solid state by using monolayers in Langmuir troughs (Feigenson, 2006; Kaganer et al., 1999). In the gas phase, lipids in a monolayer are very dilute, with an area per molecule in the range of hundreds of $Å^2$/molecule. As pressure is increased, the area per molecule decreases and the monolayer enters what is termed the liquid-expanded (LE or $L_1$) state. Further pressure increase leads to the liquid-compressed (LC or $L_2$) state, where the area per molecule has decreased to about 25 $Å^2$/molecule. As this LC lipid packing density is reported to be comparable to a lipid bilayer under physiological conditions (Seelig, 1987), lipid monolayers in the LC state are frequently used as membrane models. Our studies employed both lipid monolayers and bilayers to model the interaction of proteins and lipid membranes. In this way we could test for changes in the structure of both the protein and membrane, which we hypothesize may lead to either protein misfolding or membrane disruption.

### 1.3.4 *IDPs such as tau and interaction with lipid membranes*

Several IDPs, including tau, have been shown to interact with lipid membranes (Arispe et al., 1993; Arispe et al., 1994; Simakova & Arispe, 2007; Uversky et al., 2008). Because of the presence of charged groups, tau in particular is prone to heterogeneous interactions, including with the lipid membrane. Such interaction of tau with the lipid membrane could induce structural changes in the protein itself and also affect membrane integrity. We propose that interactions between tau and interfaces such as the cell membrane can induce disordered-to-ordered transitions in the protein, lowering the activation free energy of aggregation. We hypothesize that IDPs like tau are highly susceptible to abnormal binding to interfaces due to their unique combination of high specificity and low affinity for coupled binding-and-folding events. Such interaction can induce transitions from a disordered but non-aggregate-forming conformation to a conformation that is aggregation-competent, which can then template the assembly of tau into highly ordered fibrils.

We also propose that tau-induced membrane disruption may serve as a pathway by which the protein exerts toxicity. We hypothesize that tau will cause changes to both the order and integrity of anionic lipid membranes, which will result in death of the cell. Lipid membrane damage will lead to ion dysregulation, which can serve as a method of cytotoxicity *in vivo.*

## 1.4 Neutron and X-ray scattering studies give structural information about membrane and tau upon their interaction

Several scattering techniques in recent years, including neutron and X-ray reflectivity (NR or XR) and grazing incidence X-ray diffraction (GIXD) have been used to study the surface properties of thin films ( Als-Nielsen et al., 1994; Als-Nielsen & Kjaer, 1989; Eisenberger & Feldman, 1981; Feidenhans'l, 1989; Russell, 1990). These techniques, which can provide information about molecular scale composition and ordering of molecules at interfaces, utilize the wave characteristics of the probe (neutron or X-ray in this case) near the condition of perfect reflection. After being incident upon the atoms, X-rays are scattered from the electrons while neutrons are scattered from nuclei (Dubey et al., 2011; Majewski et al., 2000; Russell, 1990). These X-rays or neutrons are then incident upon a detector. The resulting signals from the detector give valuable and detailed information about the molecular composition and ordering of the films. X-ray reflectivity provides the electron density composition of the film and GIXD provides information about the in-plane ordering of the film. NR provides information about the chemical composition of the film (Als-Nielsen & Kjaer, 1989; Pedersen & Hamley, 1994). This data cannot be gathered from other experimental assays such as Langmuir trough pressure/area assays or fluorescence imaging of a model membrane.

### 1.4.1 *Neutron scattering*

Neutron reflectivity (NR) studies result in information about membrane perturbation of model lipid bilayers, including from tau's interaction with the lipid

membrane (Figure 1.5). Analysis of NR data provides knowledge of coherent scattering length density (SLD) distribution in a model lipid bilayer sample. SLD is a value unique to a particular chemical composition and is the sum of coherent scattering lengths of constituent elements divided by the volume they occupy. Structural changes of a bilayer upon interaction with tau protein can be easily observed using neutron scattering (Als-Nielsen et al., 1984; Pedersen & Hamley, 1994).

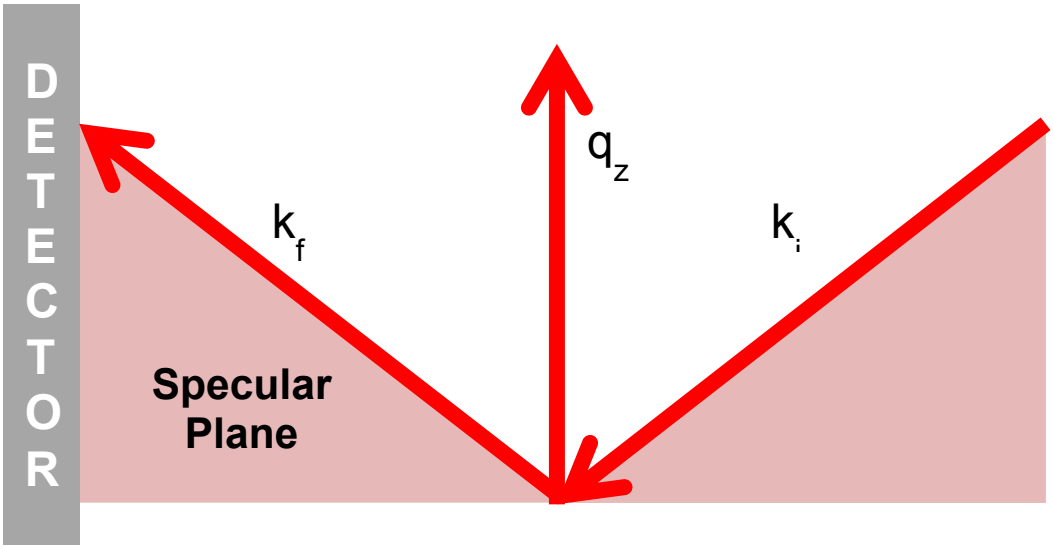


Figure 1.5 A typical scattering geometry for neutron reflectometry.

In Figure 1.5, $k_i$ and $k_f$ are the incident and reflected neutron wave vectors, respectively, and $q_z$ is the z component of the momentum transfer vector.

### 1.4.2 *X-ray scattering*

#### 1.4.2.1 Grazing incidence X-ray diffraction

Grazing incidence X-ray diffraction (GIXD) provides information about the disruption of lipid ordering on a molecular scale. In GIXD, the angle GIXD data give structural information on the in-plane (*i.e.*, in the plane of the monolayer) ordered (hence diffracting) portion of the film (Figure 1.6). Presence of Bragg peaks in GIXD data indicates 2D ordered structures.

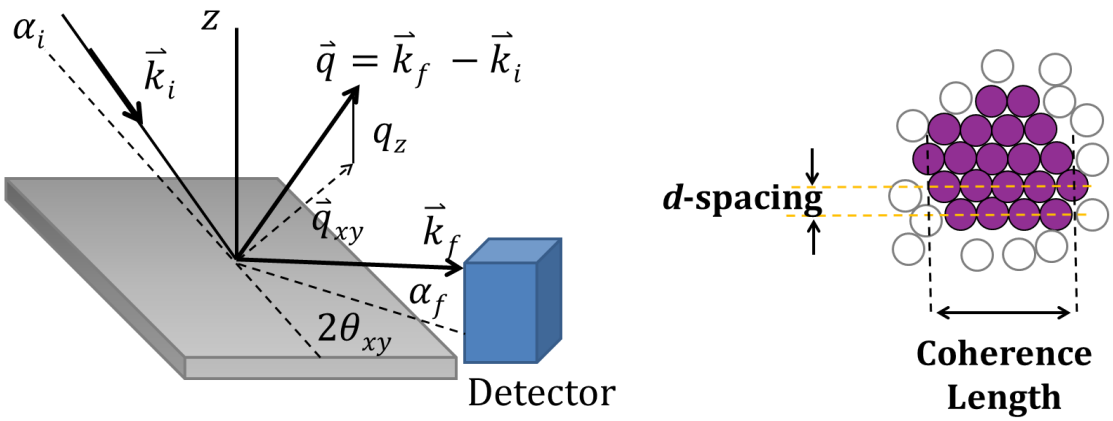


Figure 1.6 Schematic of grazing incidence X-ray diffraction and top down simplified view of a lipid monolayer.

In Figure 1.6, $k_i$ and $k_f$ are the incident and final X-ray wave vectors, respectively, with $\alpha_i$ and $\alpha_f$ as the incident and final angles. q is the momentum transfer vector, which in the diagram is broken into its z and xy components. The $2\theta_{xy}$ angle refers to the angular distance which is traversed by the detector as it translates in the xy plane.

### 1.4.2.2 X-ray reflectivity

X-ray reflectivity gives information about the compaction and aggregation of protein. XR data give information about the out-of-plane (perpendicular to the lipid film) electron density profile of the film averaged over the LE and LC phases (Figure 1.7). In general, at every interface a portion of X-rays is reflected. Interference of these partially reflected beams creates a reflectometry pattern.

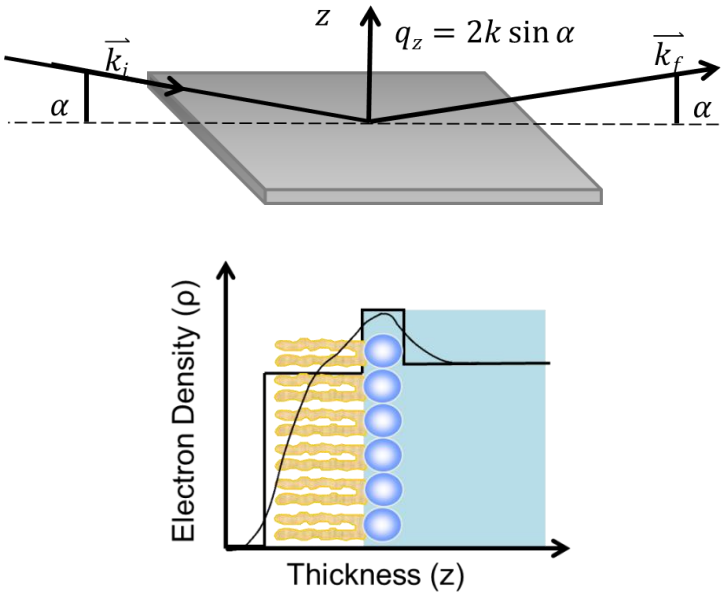


Figure 1.7 Schematic of X-ray reflectivity.

Figure 1.7 illustrates a schematic of X-ray reflectivity and a sample graph showing how chemically distinct molecular layers (*e.g.*, proteins, lipid headgroups and tails) have different electron densities and can be modeled as boxes. $k_i$ and $k_f$ are the incident and final X-ray wave vectors, respectively, with α as the incident and final angle. $q_z$ is the z component of the momentum transfer vector, equal to 2ksin α.

### 1.5 Effects of osmolytes

In order to better understand the interaction of proteins with lipid membranes, the simple model of a lipid monolayer or bilayer on a water subphase must be extended to a more physiological model. Factors which are ignored in the simpler models include molecular crowding and preferential exclusion. In a human cell, the cytoplasm has a high concentration of macromolecules (50-400 mg/mL) (Chebotareva et al., 2004). This molecular crowding may significantly change the stability, conformation and functional property of protein molecules (Batra et al., 2009; Harries & Rosgen, 2008; Johansen et al., 2011). A major contributor to this crowding is the presence of osmolytes. Osmolytes are small co-solutes that influence and counterbalance the osmotic pressure of the cell and the cellular environment (Yancey, 1982). The most common naturally occurring osmolytes include polyols (glucose and sucrose), urea and methylamines (Lee, 1981). Osmolytes are also preferentially excluded over water from the protein surface, exerting non-specific interfacial effects on proteins. The result is an increase in the surface tension of the protein/solvent interface, driving the stabilization of protein structure as the protein conformation equilibrium is shifted to a more folded state (Harries & Rosgen, 2008; Arakawa & Timasheff, 1985).

Examining the effects of sucrose, a model osmolyte, on the surface activity of Aβ and its interaction with a lipid membrane moves the model to a more physiological representation. Sucrose shifts the protein conformation equilibrium toward a minimal exposed surface area. In the presence of a membrane interface, the protein will insert into

a leaflet of a lipid (membrane interface) to further minimize solvent exposed surface area (Anaya, 2013).

## 1.6 Structural and molecular insights gained from study of additional polyampholytes with lipid membranes

### 1.6.1 *Polyampholytes and amphiphiles*

Polymers are large molecules formed from many repeating subunits. These can be produced by living organisms (biopolymers) or synthetically created. Both natural and artificial polymers are created by the polymerization of many small molecules, or monomers, into a long, covalently bonded chain (Painter & Coleman, 1997; McCrum et al., 1997). Polymeric biomolecules include three main classes: polynucleotides (DNA and RNA), polysaccharides (*e.g.*, starches or glycogen), and polypeptides (polymers of amino acids) (Mohanty et al., 2005; Meyers et al., 2008; Chandra, 1998). An amphoteric molecule is defined as one which can react either as an acid or as a base. Polyampholytes, polymers which contain both acidic and basic groups, are one type of this molecule. These molecules are prone to heterogeneous interactions because of their charged nature (Kudaibergenov, 2002, 2008). Ampholytes can also be classified as amphiphilic when they possess both hydrophilic and hydrophobic characteristics.

A range of chemical compounds, such as soaps, detergents and lipoproteins, are amphiphiles. One example group is hydrocarbon based surfactants, which may have an ionic or non-ionic polar region. Many components of physiological cell membranes are amphiphilic, including phospholipids, cholesterol and glycolipids. The amphiphilic

properties of phospholipids are the driving force behind their self-assembly into structures such as micelles and bilayers (Furse, 2011; Royal Society of Chemistry, 2014). Peptides also possess amphiphilic properties, driving their self-assembly into folded structures with hydrophobic residues at the center of their structure protected from interaction with aqueous surroundings (Yu et al, 1996).

The tau protein is both a polyampholyte and amphiphile. To learn more about how tau interacts with amphiphilic lipid membranes, and the subsequent effects on both the lipid and the tau molecule, we performed studies of the analogous interactions of lipid membranes with other polyampholyte molecules, including biocidal polymers and the galectin GM-1.

### 1.6.2 *OPEs, CPEs, and membrane destabilization*

Cationic phenylene ethynylene oligomers and polymers (OPEs and CPEs) can exhibit biocidal activity against bacteria *via* membrane destabilization (Y. Wang et al., 2010). Membrane destabilization is dependent on the lipid composition of bacterial cell membranes as opposed to mammalian cell membranes (Ji et al., 2011). This is similar to the charge-dependent interaction of tau protein with lipid monolayers or bilayers. Examination of the changes to the photophysical characteristics of lipid membranes after interaction with OPEs provides insight into possible mechanisms of cellular toxicity resulting from tau protein and lipid membrane interaction.

### 1.6.3 *Galectin*

Studying the interaction between galectin and a ganglioside GM1-containing lipid membrane provides insight into how insertion of galectin into a model lipid monolayer affects membrane properties such as fluidity, as well as the structure of the protein itself. H-Gal1, the protein discussed here, is a member of the galectin family. Galectins are proteins which are defined by their binding specificity for β-galactoside sugars (Barondes, 1994). They have a broad range of functions from mediation of cell-cell interactions to transmembrane signaling (Taylor, 2011). H-Gal1, whose structure has been shown to change upon entering a hydrophobic environment (Gupta et al., 2006), exerts growth control *via* GM1 binding on human neuroblastoma (SK-N-MC) cells *in vitro* and on activated T effector cells (Kopitz et al., 2010; Ledeen et al., 2012; J. Wang et al., 2009; Wu et al., 2011). Investigation of H-Gal1and its insertion into lipid membranes *via* X-ray scattering techniques provides further insight into the structural changes that take place in both the protein and the membrane when protein insertion occurs.

## 1.7 Structural explication of tau protein and lipid membrane interaction

With these models in mind, we began our study of the tau protein and its interaction with lipid membranes in order to learn more about the structural changes which occur in both the protein itself and the lipid membranes. Studies of model lipid membranes interacting with the full length tau protein, as described in Chapter 2, helped elucidate the structural changes which take place in the tau protein and in the membrane upon such interaction. Further experiments described in Chapter 3 using tau constructs and a hyperphosphorylation mimic investigated the effects of domain composition and

hyperphosphorylation on the structural effect of this interaction between tau and lipid membranes. To further the complexity of the model, additional studies described in Chapter 4 explored the role of osmolytes in protein folding at lipid interfaces. Investigation into photophysical characteristics of ampholytic membrane destabilization, described in Chapter 5, supplied insight into the ways that ampholytes such as tau may induce cellular toxicity. Structural changes that occur in a protein and lipid after protein insertion into a lipid interface were also examined using X-ray reflectivity techniques as described in Chapter 6. Together, these studies provide insight into the structural changes that take place in both the tau protein itself and in the lipid membranes it interacts with. This work helps elucidate the causes of tau protein misfolding leading to aggregation and lipid membrane disruption.

## 1.8 References


Alonso Adel, C., Mederlyova, A., Novak, M., Grundke-Iqbal, I., & Iqbal, K. (2004). Promotion of hyperphosphorylation by frontotemporal dementia tau mutations. *J Biol Chem, 279*(33), 34873-34881.

Als-Nielsen, J., & Aage, J. (1984). X-ray studies of phase transitions on surfaces. *Physica B: Condensed Matter, 126*(1-3), 145-148.

Als-Nielsen, J., Jacquemain, D., Kjaer, K., Leveiller, F., Lahav, M., & Leiserowitz, L. (1994). Principles and applications of grazing incidence X-ray and neutron scattering from ordered molecular monolayers at the air-water interface. *Physics Reports, 246*(5), 251-313.

Als-Nielsen, J., & Kjaer, K. (1989 April 4 - April 14, 1989). *X-ray reflectivity and diffraction studies of liquid surfaces and surfactant monolayers.* Paper presented at the The proceedings of the NATO Study Institute, Phase transitions in soft condensed matter, Geilo, Norway.

Anaya, J. (2013). *Effects of osmolytes: Amyloid-beta protein surface activity and membrane interaction.* University of New Mexico, Albuquerque.

Arakawa, T. & Timasheff, S.N. (1985). The stabilization of proteins by osmolytes. *Biophys J 47*(3), 411-414.

Arispe, N., Pollard, H. B., & Rojas, E. (1993). Giant multilevel cation channels formed by Alzheimer-disease amyloid beta-protein [a-Beta-P-(1-40)] in bilayer-membranes. *Proceedings of the National Academy of Sciences of the United States of America, 90*(22), 10573-10577.

Arispe, N., Pollard, H. B., & Rojas, E. (1994). The ability of amyloid beta-protein [A beta P (1-40)] to form Ca2+ channels provides a mechanism for neuronal death in Alzheimer's disease. *Ann N Y Acad Sci, 747*, 256-266.

Ballatore, C., Lee, V. M., & Trojanowski, J. Q. (2007). Tau-mediated neurodegeneration in Alzheimer's disease and related disorders. *Nat Rev Neurosci, 8*(9), 663-672.

Barondes Sh, C. D. N. G. M. A. L. H. (1994). Galectins. Structure and function of a large family of animal lectins. *J of biological chemistry, 269*(33), 20807-20810.

Batra, J., Xu, K., Qin, S., & Zhou, H. X. (2009). Effect of macromolecular crowding on protein binding stability: Modest stabilization and significant biological consequences. *Biophys J, 97*(3), 906-911.

Berg, H.C. (1993). *Random Walks in Biology.* Princeton University Press. Princeton, N.J.

Berger, Z., Roder, H., Hanna, A., Carlson, A., Rangachari, V., Yue, M., et al. (2007). Accumulation of pathological tau species and memory loss in a conditional model of tauopathy. *Journal of Neuroscience, 27*(14), 3650-3662.

Brandt, R., Léger, J., & Lee, G. (1995). Interaction of tau with the neural plasma membrane mediated by tau's amino-terminal projection domain. *Journal of Cell Biology, 131*(5), 1327-1340.

Butterfield, S. M., & Lashuel, H. A. (2010). Amyloidogenic protein–membrane interactions: Mechanistic insight from model systems. *Angewandte Chemie International Edition, 49*(33), 5628-5654.

Campos-Peña, V., Tapia-Ramírez, J., Sánchez-Torres, C., & Meraz-Rios, M. A. (2009). Pathological-like assembly of tau induced by a paired helical filament core expressed at the plasma membrane. [10.3233/JAD-2009-1198]. *Journal of Alzheimer's Disease, 18*(4), 919-933.

Chandra, R. & Rustgi,R. (1998). Biodegradable polymers. *Progress in Polymer Sci (23)*1273.

Chebotareva, N. A., Kurganov, B. I., & Livanova, N. B. (2004). Biochemical effects of molecular crowding. *Biochemistry (Mosc), 69*(11), 1239-1251.

Chi, E. Y., Ege, C., Winans, A., Majewski, J., Wu, G., Kjaer, K., et al. (2008). Lipid membrane templates the ordering and induces the fibrillogenesis of Alzheimer's disease amyloid-beta peptide. *Proteins, 72*(1), 1-24.

Clavaguera, F., Lavenir, I., Falcon, B., Frank, S., Goedert, M., & Tolnay, M. (2013). "Prion-like" templated misfolding in tauopathies. *Brain Pathol, 23*(3), 342-349.

Daughdrill, G. W., Pielak, G. J., Uversky, V. N., Cortese, M. S., & Dunker, A. K. (2008). Natively Disordered Proteins *Protein Folding Handbook* (pp. 275-357): Wiley-VCH Verlag GmbH.

DeGroot, N.S., Aviles, F.X., Vendrell, J., & Ventura, S. (2006). Mutagenesis of the central hydrophobic cluster in abeta42 Alzheimer's peptide: Side-chain properties correlate with aggregation propensities. *FEBS J 273*(3) 658-668.

Demuro, A., Mina, E., Kayed, R., Milton, S. C., Parker, I., & Glabe, C. G. (2005). Calcium dysregulation and membrane disruption as a ubiquitous neurotoxic mechanism of soluble amyloid oligomers. *J Biol Chem, 280*(17), 17294-17300.

Dubey, M., Jablin, M., Wang, P., Mocko, M., & Majewski, J. (2011). SPEAR — ToF neutron reflectometer at the Los Alamos Neutron Science Center. *The European Physical Journal Plus, 126*(11), 1.

Dunker, A. K., Lawson, J. D., Brown, C. J., Williams, R. M., Romero, P., Oh, J. S., et al. (2001). Intrinsically disordered protein. *Journal of Molecular Graphics and Modelling, 19*(1), 26-59.

Dyson, H. J., & Wright, P. E. (2005). Intrinsically unstructured proteins and their functions. [10.1038/nrm1589]. *Nat Rev Mol Cell Biol, 6*(3), 197-208.

Eisenberger, P., & Feldman, L. C. (1981). New approaches to surface structure determinations. *Science, 214*(4518), 300-305.

Elbaum-Garfinkle, S., Ramlall, T., & Rhoades, E. (2010). The role of the lipid bilayer in tau aggregation. *Biophysical Journal, 98*(11), 2722-2730.

Feidenhans'l, R. (1989). Surface structure determination by X-ray diffraction. *Surface Science Reports, 10*(3), 105-188.

Feigenson, G. W. (2006). Phase behavior of lipid mixtures. [10.1038/nchembio1106-560]. *Nat Chem Biol, 2*(11), 560-563.

Fischer, E. (1894). Einfluss der Configuration auf die Wirkung der Enzyme. *Berichte der deutschen chemischen Gesellschaft, 27*(3), 2985-2993.

Furse, S. (2011, 5 Nov. 2011). The Structure of a Membrane. Retrieved 4 Sep. 2014, from http://www.samuelfurse.com/2011/11/the-structure-of-a-membrane/

Ghanta, J., Shen, C. L., Kiessling, L. L., & Murphy, R. M. (1996). A strategy for designing inhibitors of beta-amyloid toxicity. *J Biol Chem, 271*(47), 29525-29528.

Goedert, M. (2005). Tau gene mutations and their effects. *Mov Disord, 20 Suppl 12*, S45-52.

Goedert, M., Clavaguera, F., & Tolnay, M. (2010). The propagation of prion-like protein inclusions in neurodegenerative diseases. *Trends Neurosci, 33*(7), 317-325.

Goedert, M., & Jakes, R. (2005). Mutations causing neurodegenerative tauopathies. *Biochim Biophys Acta, 1739*(2-3), 240-250.

Goedert, M., Jakes, R., Spillantini, M. G., Hasegawa, M., Smith, M. J., & Crowther, R. A. (1996). Assembly of microtubule-associated protein tau into Alzheimer-like filaments induced by sulphated glycosaminoglycans. [10.1038/383550a0]. *Nature, 383*(6600), 550-553.

Goodsaid-Zalduondo, F., Rintoul, D.A., Carlson, J.C., & Hansel, W. (1982). Lutoeolysis-induced changes in phase composition and fluidity of bovine lutial cell membranes.*Proc Natl Acad Sci USA, 79*(14), 4332-4336.

Gray E.G., M., P.-B., & Roher, A. (1987). Alzheimer's disease: Paired helical filaments and cytomembranes. *Neuropathol Appl Neurobiol, 13*(2), 91-110.

Gupta, R. K., Pande, A. H., Gulla, K. C., Gabius, H. J., & Hajela, K. (2006). Carbohydrate-induced modulation of cell membrane. VIII. Agglutination with mammalian lectin galectin-1 increases osmofragility and membrane fluidity of trypsinized erythrocytes. *FEBS Lett, 580*(6), 1691-1695.

Harries, D., & Rosgen, J. (2008). A practical guide on how osmolytes modulate macromolecular properties. *Methods Cell Biol, 84*, 679-735.

Hiltunen, M., van Groen, T., & Jolkkonen, J. (2009). Functional roles of amyloid-β protein precursor and amyloid-β peptides: Evidence from experimental tudies. *Journal of Alzheimer's Disease, 18*(2), 401-412.

Hong, M., Zhukareva, V., Vogelsberg-Ragaglia, V., Wszolek, Z., Reed, L., Miller, B. I., et al. (1998). Mutation-specific functional impairments in distinct tau isoforms of hereditary FTDP-17. *Science, 282*(5395), 1914-1917.

Iakoucheva, L. M., Brown, C. J., Lawson, J. D., Obradovic, Z., & Dunker, A. K. (2002). Intrinsic disorder in cell-signaling and cancer-associated proteins. *J Mol Biol, 323*(3), 573-584.

Ji, E., Parthafaraphy,A., Corbitt, T.S., Schanze, K.F., Whitten, D.G. (2011). Antibacterial activity of conjugated polyelectrolites with variable chain lengths.*Langmuir (27)*17, 10763-10769.

Johansen, D., Jeffries, C. M., Hammouda, B., Trewhella, J., & Goldenberg, D. P. (2011). Effects of macromolecular crowding on an intrinsically disordered protein characterized by small-angle neutron scattering with contrast matching. *Biophys J, 100*(4), 1120-1128.

Kaganer, V. M., Möhwald, H., & Dutta, P. (1999). Structure and phase transitions in Langmuir monolayers. *Reviews of Modern Physics, 71*(3), 779-819.

Kawarabayashi, T., Shoji, M., Younkin, L. H., Wen-Lang, L., Dickson, D. W., Murakami, T., et al. (2004). Dimeric amyloid β protein rapidly accumulates in lipid rafts followed by apolipoprotein E and phosphorylated tau accumulation in the Tg2576 mouse model of Alzheimer's disease. *The Journal of Neuroscience, 24*(15), 3801-3809.

Khemtemourian, L., Killian, J. A., Hoppener, J. W., & Engel, M. F. (2008). Recent insights in islet amyloid polypeptide-induced membrane disruption and its role in beta-cell death in type 2 diabetes mellitus. *Exp Diabetes Res, 2008*, 421287.

Kim, J. R., Gibson, T. J., & Murphy, R. M. (2003). Targeted control of kinetics of beta-amyloid self-association by surface tension-modifying peptides. *J Biol Chem, 278*(42), 40730-40735.

Kim, J. R., Muresan, A., Lee, K. Y., & Murphy, R. M. (2004). Urea modulation of beta-amyloid fibril growth: Experimental studies and kinetic models. *Protein Sci, 13*(11), 2888-2898.

Kim, J. R., & Murphy, R. M. (2004). Mechanism of accelerated assembly of beta-amyloid filaments into fibrils by KLVFFK(6). *Biophys J, 86*(5), 3194-3203.

Kopitz, J., Bergmann, M., & Gabius, H. J. (2010). How adhesion/growth-regulatory galectins-1 and -3 attain cell specificity: Case study defining their target on neuroblastoma cells (SK-N-MC) and marked affinity regulation by affecting microdomain organization of the membrane. *IUBMB Life, 62*(8), 624-628.

Korade, Z., & Kenworthy, A.K. (2008). Lipid rafts, cholestrol, and the brain. *Neuropharmacology, 55*(8), 1255-1273.

Kremer, J. J., & Murphy, R. M. (2003). Kinetics of adsorption of beta-amyloid peptide Abeta(1-40) to lipid bilayers. *J Biochem Biophys Methods, 57*(2), 159-169.

Kudaibergenov, S.E., (2002). *Polyampholytes.*Springer North America.

Kudaibergenov, S.E., (2008). Polyampholytes in *Encyclopedia Polymer Science and Technology.* John Wiley & Sons. Hoboken, N.J.

Ledeen, R. W., Wu, G., Andre, S., Bleich, D., Huet, G., Kaltner, H., et al. (2012). Beyond glycoproteins as galectin counterreceptors: Tumor-effector T cell growth control via ganglioside GM1 [corrected]. *Ann N Y Acad Sci, 1253*, 206-221.

Lee, J. C. T., S. N. (1981). The stabilization of proteins by sucrose. *J Biol Chem, 256*, 7193-7201.

Lee, V., Goedert, M., & Trojanowski, J.Q. (2001). Neurodegenerative tauopathies. *Ann Rev Neurosci (24)*1, 1121-1159.

Majewski, J., Kuhl, T. L., Wong, J. Y., & Smith, G. S. (2000). X-ray and neutron surface scattering for studying lipid/polymer assemblies at the air-liquid and solid-liquid interfaces. *J Biotechnol, 74*(3), 207-231.

Mandelkow, E., von Bergen, M., Biernat, J., & Mandelkow, E. M. (2007). Structural principles of tau and the paired helical filaments of Alzheimer's disease. *Brain Pathol, 17*(1), 83-90.

Marx, J. (2007). Alzheimer's disease: A new take on tau. *Science, 316*(5830), 1416-1417.

McCrum, N.G. & Buckley, C.T. (1997). *Principles of Polymer Engineering.* Oxford University Press. Oxford, NY.

Meredith, S. C. (2005). Protein denaturation and aggregation: Cellular responses to denatured and aggregated proteins. *Ann N Y Acad Sci, 1066*, 181-221.

Meyers, M.A., et al., (2008). Biological materials: Stucture and mechanical properties. *Progress in Mat Sci (53),* 1.

Mohanty, A.K. et al., (2005). *Natural fibers, Biopolymers and Biocomposites.* C.R.C. Press North America.

Nacharaju, P., Lewis, J., Easson, C., Yen, S., Hackett, J., Hutton, M., et al. (1999). Accelerated filament formation from tau protein with specific FTDP-17 missense mutations. *FEBS Lett, 447*(2-3), 195-199.

Painter, P. & Coleman, M. (1997). *Fundamentals of Polymer Science, an introductory text.*Technomics Publishing. Lancaster, PA.

Pedersen, J.S. & Hamley, I.W. (1994). Analysis of neutron reflectivity data by constrained least squares methods. *Physica B (198)*123, 16-23.

Pike, L.J. (2009). The challenge of lipid rafts. *J Lipid Res, 50Suppl,*S323-328.

Royal Society of Chemistry. (2014). Surfactants: the Ubiquitous Amphiphile. Retrieved 2014 from http://www.rsc.org/chemistryworld/issues/2003/july/amphiphiles.asp/

Russell, T. P. (1990). X-ray and neutron reflectivity for the investigation of polymers. *Materials Science Reports, 5*(4), 171-271.

Seelig, A. (1987). Local anesthetics and pressure: A comparison of dibucaine binding to lipid monlayers and bilayers. *BioChim BioPhys Acta (889)*2, 196-204.

Selkoe, D. J. (2000). Toward a comprehensive theory for Alzheimer's disease. Hypothesis: Alzheimer's disease is caused by the cerebral accumulation and cytotoxicity of amyloid β-protein. *Annals of the New York Academy of Sciences, 924*(1), 17-25.

Silvius, B.R. (1982). *Thermotropic Phase Transitions of Pure Lipids in Model Membranes and their Modifications by Membrane Proteins.*John Wiley & Sons. Hoboken, N.J.

Simakova, O., & Arispe, N. J. (2007). The cell-selective neurotoxicity of the Alzheimer's Abeta peptide is determined by surface phosphatidylserine and cytosolic ATP levels. Membrane binding is required for Abeta toxicity. *J Neurosci, 27*(50), 13719-13729.

Simons, K., & Ehehalt, R. (2002). Cholesterol, lipid rafts, and disease.*J Clin Invest, 110*(5), 597-603.

Singer, S. J. (1972). A fluid lipid-globular protein mosaic model of membrane structure. *Ann N Y Acad Sci, 195*, 16-23.

Singer, S. J., & Nicolson, G. L. (1972). The fluid mosaic model of the structure of cell membranes. *Science, 175*(4023), 720-731.

Skou, J. C. (1965). Enzymatic basis for active transport of Na+ and K+ across cell membrane, *Phyiol Rev 45*, 596-617.

Soto, C. (2003). Unfolding the role of protein misfolding in neurodegenerative diseases. [10.1038/nrn1007]. *Nat Rev Neurosci, 4*(1), 49-60.

Taylor, M. E. D. K. (2011). *Introduction to Glycobiology*. Oxford; New York: Oxford University Press.

Team, S. E. (2008, 11 Nov. 2008). Cells. Retrieved 4 Sep. 2014, from http://www.shmoop.com/biology-cells/

Treatments and Research. (2014). from http://www.alz.org/i-have-alz/treatments-and-research.asp

Uversky, V. N., & Dunker, A. K. (2010). Understanding protein non-folding. *Biochim Biophys Acta, 1804*(6), 1231-1264.

Uversky, V. N., Oldfield, C. J., & Dunker, A. K. (2008). Intrinsically disordered proteins in human diseases: Introducing the D2 concept. *Annu Rev Biophys, 37*, 215-246.

Walker, L. C., Diamond, M. I., Duff, K. E., & Hyman, B. T. (2013). Mechanisms of protein seeding in neurodegenerative diseases. *JAMA Neurol, 70*(3), 304-310.

Wang, J., Lu, Z. H., Gabius, H. J., Rohowsky-Kochan, C., Ledeen, R. W., & Wu, G. (2009). Cross-linking of GM1 ganglioside by galectin-1 mediates regulatory T cell activity involving TRPC5 channel activation: Possible role in suppressing experimental autoimmune encephalomyelitis. *J Immunol, 182*(7), 4036-4045.

Wang, Y., Tang, Y., Zhou, Z., Ji, E., Lopez, G. P., Chi, E. Y., et al. (2010). Membrane perturbation activity of cationic phenylene ethynylene oligomers and polymers: Selectivity against model bacterial and mammalian membranes. *Langmuir, 26*(15), 12509-12514.

Williamson, R., Usardi, A., Hanger, D. P., & Anderton, B. H. (2008). Membrane-bound β-amyloid oligomers are recruited into lipid rafts by a fyn-dependent mechanism. *The FASEB Journal, 22*(5), 1552-1559.

Wu, G., Lu, Z. H., Gabius, H. J., Ledeen, R. W., & Bleich, D. (2011). Ganglioside GM1 deficiency in effector T cells from NOD mice induces resistance to regulatory T-cell suppression. *Diabetes, 60*(9), 2341-2349.

Yancey, P. H., Clark, M.E., et al. (1982). Living with water stress: Evolution of osmolyte systems. *Science, 217*(4566), 1214-1222.

Yu, Y.C., Berndt, P., Tirrell, M., & Fields, G.B. (1996). Self-assembling amphiphiles for construction of protein molecular architecture. *JACS, 118*(50), 12515-12520.

# CHAPTER 2 INTERACTION OF TAU PROTEIN WITH MODEL LIPID MEMBRANES INDUCES TAU STRUCTURAL COMPACTION AND MEMBRANE DISRUPTION

(This chapter has been published in *Biochemistry* and appears as Emmalee M. Jones, Manish Dubey, Phillip J. Camp, Briana C. Givler, Jacek Biernat, Eckhard Mandelkow, Jaroslaw Majewski, Eva Y. Chi. 2012. Interaction of tau protein with model lipid membranes induces tau structural compaction and membrane disruption, *Biochemistry*, **51**: 2539-2250)

## Abstract

Neurofibrillary tangles composed of the tau protein are major hallmarks of Alzheimer's disease. The mechanism of tau's aggregation is unknown, but likely involves polyanionic cofactors. Tau is mainly a cytosolic microtubule-associated protein, but has also been proposed to interact with the plasma membrane and membranous organelles. This prompted our detailed investigation of tau's interactions with model lipid membranes. We show that the intrinsically disordered full-length tau is highly surface active, preferentially associates with anionic DMPG lipid membranes, undergoes structural compaction, and induces membrane morphological changes observed with fluorescence microscopy. To resolve molecular-scale structural details of tau at the air/water and membrane interfaces, X-ray scattering techniques are used. X-ray reflectivity modeling indicates tau's presence under a DMPG monolayer and partial insertion into the lipid headgroup region, while grazing incidence X-ray diffraction shows that tau insertion disrupts lipid packing. Moreover, both interfaces induce tau to partially adopt a more compact conformation similar to that of a folded protein. Neutron reflectivity assays show that tau completely disrupts DMPG bilayers while leaving the neutral DPPC bilayer intact. Our results indicate that tau's strong interaction with anionic lipid membranes induces tau

structural compaction and membrane disruption, suggesting possible membrane-based mechanisms of tau aggregation and toxicity.

## 2.1 Introduction

Alzheimer's disease (AD) is a neurodegenerative disease characterized by neurofibrillary tangles (NFTs) and amyloid plaques found in the brains of affected patients (Buée et al., 2000; Soto, 2003). The extracellular amyloid plaques consist of deposits of the amyloid-β peptide (Aβ) (Selkoe, 2000) and the intracellular NFTs are composed of aggregates of the hyperphosphorylated tau protein (Kosik et al., 1986). In addition to AD, NFTs have also been linked to the pathogenesis of more than 20 other neurodegenerative disorders collectively termed tauopathies (Lee et al., 2001). Tau's role in the development of neurodegenerative diseases is still unclear, but a link between pathological tau aggregation and cognitive impairments has been shown (Berger et al., 2007). Moreover, the identification of multiple tau gene point mutations that result in hereditary tauopathies is evidence that tau malfunction alone is sufficient to cause neurodegeneration (Poorkaj et al., 1998; Spillantini & Goedert, 1998). However, two key features of tau pathology are still unclear. First, the molecular basis of the early aggregation events, such as the structural fluctuations that trigger the aberrant accumulation of tau into NFTs rich in β-sheets *in vivo*, remain unknown. Second, the mechanism(s) by which tau aggregation causes neuronal dysfunction is unclear.

Tau proteins are expressed primarily in the central nervous system, and their critical function of promoting microtubule (MT) assembly and stability is mediated by six isoforms and phosphorylation, which decreases tau's affinity to MT resulting in the disassociation

of tau from MTs (Buée et al., 2000; Cleveland et al., 1977; Weingarten et al., 1975) (Figure 2.1A). Tau is rich in charged and hydrophilic residues, and thus is highly soluble. In solution, tau is intrinsically disordered. *In vitro*, tau aggregation can be induced by polyanionic cofactors, which compensate for tau's positive charges (Barghorn & Mandelkow, 2002; Chirita et al., 2003; Goedert et al., 1996; King et al., 2000; Wilson & Binder, 1997). Physiological factors and conditions that trigger tau aggregation *in vivo* are still poorly understood.

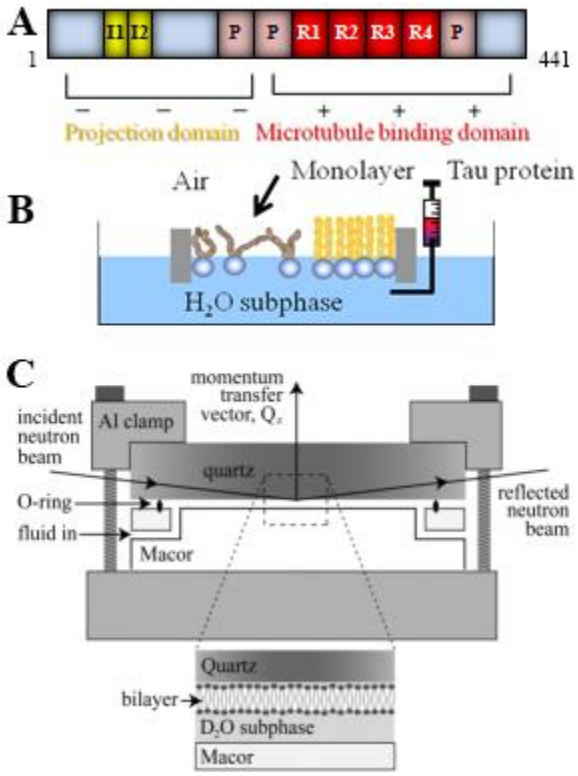


Figure 2.1 Schematics of hTau40, Langmuir trough containing a lipid monolayer, and solid-liquid interface cell.

Figure 2.1 illustrates through schematics (A) hTau40, indicating projection and microtubule binding domains and their overall charge states, (B) the Langmuir trough containing a lipid monolayer, and (C) the solid-liquid interface cell used in bilayer experiments.

Several lines of evidence suggest that plasma membranes may modulate tau dynamics. Tau has been shown to interact at least indirectly with the plasma membrane through its amino-terminal projection domain (Brandt et al., 1995) and is present in detergent resistant membrane microdomains (Kawarabayashi et al., 2004; Williamson et al., 2008). Membrane glycolipids have been found to be associated with paired helical filaments (PHFs) isolated from AD brains (Gray et al., 1987). Recently, membrane associated chimeric tau has been shown to seed the formation of PHFs from full length tau proteins (Campos-Peña et al., 2009), and anionic lipid vesicles have been shown to promote the aggregation of the microtubule binding domain of tau (K18) at sub-μM concentrations (Elbaum-Garfinkle et al., 2010). Thus, plasma membrane mediated tau misfolding and aggregation may serve as an *in vivo* mechanism by which the protein nucleates and grows into PHFs. As such, even if the membrane bound tau is only a small fraction of the protein population, it may be capable of seeding the growth of mature fibrils.

Tau-mediated neurodegeneration can arise from the loss of physiological function and/or the gain-of-toxicity (Gendron & Petrucelli, 2009; Lovestone & McLoughlin, 2002). Tau aggregation abolishes its MT-stabilizing function and can impair axonal transport (Deshpande et al., 2008). However, the absence of significant neuronal abnormalities in tau knock-out mice suggests that tau's MT-stabilizing function may not be critical and that gain-of-toxicity is more likely. There is a debate on whether mature tau fibrils are toxic or

mere inert waste, but a high β-propensity of "pro-aggregant" tau clearly leads both to tau aggregation and toxicity, whereas "anti-aggregant" tau with no β-propensity is not toxic (Sydow et al., 2011). The mechanism by which tau aggregates cause neuronal cell death is unknown. The roles of several other oligomeric protein aggregates have recently received considerable attention in numerous neurodegenerative diseases, including Aβ, α-synuclein, huntingtin, and prion oligomers (Conway et al., 2000; Lashuel et al., 2002; Novitskaya et al., 2006; Sharon et al., 2003; Walsh et al., 2002). A leading hypothesis for the mechanism of protein aggregate-induced toxicity is cell membrane disruption, resulting in the alteration of ion homeostasis and dysregulation of neuronal signal transduction (Chi et al., 2008; Chi et al., 2007; Kayed et al., 2004; Quist et al., 2005). Increases in ion permeability have been found in cells exposed to various aggregates (Demuro et al., 2005; Deshpande et al., 2006; Simakova & Arispe, 2007; Sun et al., 2003). Studies using model lipid membranes showed that Aβ induces either the formation of discrete ion channels (Arispe et al., 1993, 1994) or increases of bilayer conductance (Kayed et al., 2004; Sokolov et al., 2006; Valincius et al., 2008). Additionally, these types of membrane disruptions have been shown to be the molecular basis of toxicity and selectivity of antimicrobial compounds, including antimicrobial peptides (Gidalevitz et al., 2003) and biocidal conjugated polyelectrolytes (Wang et al., 2010).

We propose that interactions between tau and interfaces such as the cell membrane can induce disordered-to-ordered transitions in the protein, lowering the activation free energy of aggregation. We hypothesize that IDPs like tau are highly susceptible to abnormal binding to interfaces due to their unique combination of high specificity and low affinity for coupled binding-and-folding events. Such interaction can induce transitions

from a disordered but non-aggregate forming conformation to a conformation that is aggregation-competent, which can then template the assembly of tau into highly ordered fibrils. Furthermore, we propose that tau induced membrane disruption may serve as a pathway by which the protein exerts toxicity.

The focus of the current investigation is on characterizing tau-lipid membrane interactions and their effects on protein conformation and membrane stability. The full-length isoform of recombinant human tau protein (hTau40) (Figure 2.1A) is used in this study. Two model membrane systems, (i) lipid monolayer at the air-water interface, which models one leaflet of the plasma membrane, and (ii) supported lipid bilayers, are used to probe tau-membrane interactions. A combination of biophysical techniques, including pressure-area isotherms, fluorescence microscopy (FM), and X-ray and neutron scattering techniques, are used to characterize tau-membrane interactions and their effects on membrane properties. We found that although highly charged and soluble, tau is highly surface active, strongly interacts with anionic membranes, and readily disrupts membrane morphology, lipid packing, and integrity.

## 2.2 Materials and methods

### *2.2.1 Materials*

Full-length human tau (hTau40 isoform, 441 residues) was provided by Drs. J. Biernat and E. Mandelkow (Max Planck Institute for Structural Biology, Hamburg, Germany) and used without further purification. Three lipids were used to evaluate the

effect of lipid head group charge on tau-membrane interactions – zwitterionic 1,2-Dimyristoyl-sn-Glycero-3-Phosphocholine (DMPC), anionic 1,2-Dimyristoyl-sn-Glycero-3-[Phospho-rac-(1-glycerol)] (DMPG), and cationic 1,2- Dimyristoyl-3-Trimethylammonium-Propane (DMTAP). Zwitterionic Dipalmitoylphosphatidylcholine (DPPC) was used for neutron reflectivity experiments. All lipids were purchased from Avanti Polar Lipids.

DMPC, DMTAP and DPPC were dissolved in chloroform (HPLC grade, Fisher Scientific) while DMPG was dissolved in 10 vol% methanol in chloroform. For FM, the headgroup-labeled fluorescent dye Texas Red 1,2-dihexadecanoyl 3-phosphoethanolamine (TR-DHPE) (Molecular Probes) was dissolved in chloroform and included in lipid spreading solutions at 0.5 mol%. Lipid stock solutions ranged from 2 to 10 mg/ml and diluted to 0.2 or 0.5 mg/mL for spreading solutions. All lipid solutions were stored at -20°C in glass vials.

### 2.2.2 *Adsorption of hTau40 to air/water interface*

To evaluate the surface activity of hTau40, the surface pressure ($\pi$) measured by the adsorption of hTau40 from a water subphase was measured. The experiment was carried out at 25°C and on a 45 mL water subphase (Milli-Q system, Millipore, Bedford, MA) using a MiniMicro Langmuir trough (KSV Instruments Ltd., Finland). A Wilhelmy plate sensor at the center of the trough measured $\pi$ of the lipid monolayer where $\pi = \gamma_0 - \gamma$ and $\gamma_0$ is the air-water surface tension and $\gamma$ is the lipid film surface tension. The trough had a working surface area of 86.39 $cm^2$. Before injecting hTau40 into the subphase, barriers were partially closed to give a total surface area of 45 $cm^2$, roughly the same as the surface

area of the lipid monolayers compressed to 25 mN/m for the subsequent insertion experiments. For a final tau concentration of 1 μM, 1 mL of 45 μM tau was injected into the subphase using a microsyringe (Hamilton, Reno, NV).

### 2.2.3 *Constant pressure insertion assay and fluorescence microscopy*

To evaluate the interactions between hTau40 and lipid membranes, insertion of hTau40 into lipid monolayers at the air/water interface at constant π was measured. Figure 2.1B is a schematic of the insertion assay. All experiments were carried out on water subphase and at room temperature. Lipids were first spread at the air/water interface. The barriers then symmetrically compressed the monolayer at 0.3 mm/s to a target π of 25 mN/m, and π was kept constant *via* a feedback loop. This π was chosen for its relevance to physiological conditions as the lipid-packing density of a bilayer is reported to roughly correspond to that of a monolayer at ~30 mN/m (Ege & Lee, 2004; Seelig, 1987). Protein was then injected into the subphase to achieve a final 1 μM concentration. Since the monolayer was kept at a constant π, the barriers expanded as a result of protein insertion. Monolayer surface area was recorded and the % area expansion was taken as a measure of favorable tau-lipid interactions. Surface area expansion is defined as $\Delta A/A = (A-A_i)/A_i$, where A is the surface area at time t and $A_i$ is the initial surface area of the monolayer when it first reached 25 mN/m.

To monitor monolayer morphology, the trough was positioned on top of the motorized stage of an inverted optical microscope (Olympus IX 71) with a 50× objective centered on a quartz window in the bottom of the trough. A 100 Watt mercury lamp was used for fluorescence excitation. Fluorescence images were collected by a QImaging

camera (EXi Blue, QImaging Photometrics) and analyzed using the software QCapture Pro. 0.5 mol% TR-DHPE was included in the spreading solution. Due to steric hindrance, the dye partitions into the liquid-expanded (LE) phase rather than the liquid-condensed (LC) phase, giving rise to contrast (Knobler, 1990).

### 2.2.4 *X-ray scattering measurements*

Grazing-incidence X-ray diffraction (GIXD) and X-ray reflectivity (XR) data were collected at the BW1 beamline (HASYLAB, DESY, Hamburg, Germany) for both hTau40 adsorbed to the air/water interface and hTau40 inserted into a DMPG monolayer at the air/water interface. GIXD data give structural information on the in-plane (*i.e.*, in the plane of the monolayer) ordered (hence diffracting) portion of the film. Presence of Bragg peaks in GIXD data indicates 2D ordered structures. XR data give information about the out-of-plane (perpendicular to the lipid film) electron density profile of the film averaged over the LE and LC phases. The theory of XR and GIXD has been presented in detail elsewhere (Alsnielsen & Kjaer, 1989 ; Kjaer, 1994).

### 2.2.5 *Neutron reflectivity measurements*

Neutron reflectometry (NR) experiments were performed on hTau40 associated with supported lipid bilayers using the Surface ProfilE Analysis Reflectometer (SPEAR, Los Alamos National Lab). Methods and measurement of NR using SPEAR has been previously described (Dubey et al., 2010). In general, lipid bilayers were created using a Langmuir-Blodgett/Langmuir-Schaefer deposition method. Figure 2.1C is a schematic of the assembled flow cell. Neutrons entered the lateral face of the substrate and were

scattered from the substrate-subphase interface. $D_2O$ provided scattering contrast between the substrate, hydrogen-rich bilayer, and subphase. During the experiments, the ratio of elastically scattered to incident neutrons, or reflectivity ($R$), was measured as a function of the momentum-transfer vector $Q_z$. Analysis of the NR data provided information about coherent scattering-length density (SLD) distribution normal to the sample.

## 2.3 Results

### 2.3.1 *Surface activity of hTau40*

To evaluate the surface activity of hTau40, pressure ($\pi$) reached by the adsorption of hTau40 from a water subphase was measured (Figure 2.2). As shown, hTau40 rapidly adsorbed to the air/water interface after its injection into the subphase, with no lag time, and reached an equilibrium $\pi$ of ~ 16 mN/m. This value is comparable to those reached by the amphiphilic Aβ peptide (Chi et al., 2010; Ege & Lee, 2004). Moreover, the adsorption isotherm showed a reproducible, two-stage adsorption behavior. $\pi$ initially increased sharply to about 9 mN/m, followed by a plateau and subsequent slowed increase to achieve a final $\pi$ of 16 mN/m.

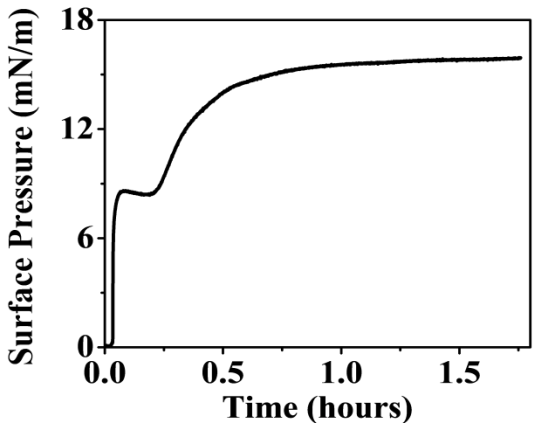


Figure 2.2 Adsorption of hTau40 to air/water interface at 25°C and 1 μM.

The XR data obtained for the adsorbed hTau40 at the air/water interface and the corresponding electron density profile (normalized to water, $\rho/\rho_{H2O}$) are shown in Figure 2.3. $\rho/\rho_{H2O}$ profile shows that hTau40 assembles in a ~10 Å thick layer at the air/protein interface with an additional 10-12 Å diffused protein layer that extends into the subphase. Fitting parameters are summarized in Table 2.1. GIXD data of the film did not reveal any diffraction peaks (data not shown) indicating a lack of long-range in-plane order for hTau40 adsorbed at the air/water interface.

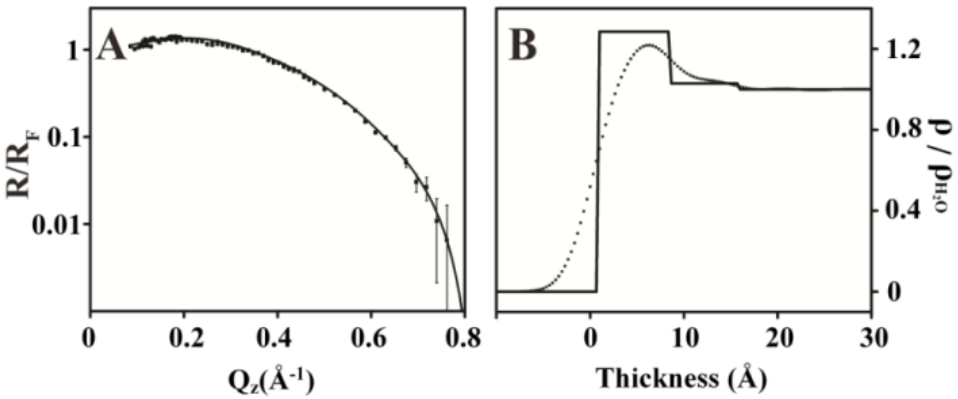


Figure 2.3 (A) Fresnel normalized X-ray reflectivity and (B) water normalized electron density of hTau40 adsorption to the air/water interface at 23 °C and 1 μM. The dashed line indicates a model independent fit and the solid line indicates a box-model fit.

Table 2.1 X-ray Reflectivity Parameters for hTau40 Adsorption to Air/water Interface

| **Sample** | **Box Composition** | **Thickness (Å)** | **ρ / $\rho_{H20}$** | **Roughness (Å)** |
|---|---|---|---|---|
| **hTau40** | air/protein interface | 7.99 ± 2.4 E-2 | 1.27 ± 3.4 E-3 | 2.66 ± 7.4 E-4 |
| | protein/subphase interface | 7.93 ± 8.6 E-2 | 1.02 ± 4.2 E-3 | 2.37 ± 6.4 E-4 |

### 2.3.2 *hTau40 insertion into lipid monolayers*

Isotherms and the accompanying % area expansion of hTau40 insertion into DMPC, DMPG, and DMTAP monolayers are shown in Figure 2.4. The protein did not insert into the neutral DMPC monolayer held at 25 mN/m and only inserted when the surface pressure was lowered to 16 mN/m (black curve in Figure 2.4A). Since this π coincided with hTau40's equilibrium π (Figure 2.2), our data show that hTau40 did not exhibit favorable interactions with the DMPC membrane. In contrast, when injected underneath the negative DMPG monolayer held at 25 mN/m, hTau40 spontaneously inserted into the monolayer and caused an area expansion of 91%. When injected underneath the positive DMTAP monolayer at 25 mN/m, hTau40 inserted into the monolayer after a short delay, but only resulted in an 8.5% area expansion (Figure 2.4).

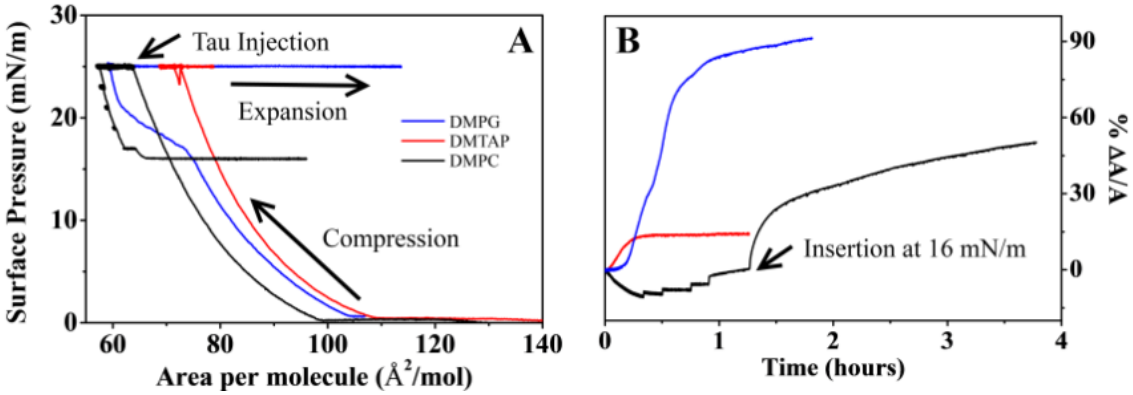


Figure 2.4 Isotherms and corresponding area expansion profiles.

Figure 2.4 illustrates isotherms (A) and corresponding area expansion profiles (B) for hTau40 insertion into DMPC, DMPG, and DMTAP monolayers at 25°C on water

subphase. The lipid monolayers were first compressed to 25 mN/m, after which tau was injected into the subphase. No insertion was observed at 25 mN/m for DMPC. Pressure was reduced until insertion was observed at 16 mN/m. Tau spontaneously inserted into DMPG and DMPTAP monolayers at 25 mN/m.

Disruption of the DMPG monolayer induced by hTau40 insertion was assessed by monitoring the morphology of the lipid film before and after hTau40 injection. Representative FM images are shown in Figure 2.5. At 25 °C, the DMPG monolayer on water undergoes a liquid-expanded (LE) to liquid-condensed (LC) phase transition at ~17 mN/m (Figure 2.4A). Because the bulky lipid headgroup dye molecules, TR-DHPE, are preferentially excluded from the LC phase, it appears as dark domains whereas the LE phase containing the dyes is bright. Figure 2.5A shows that at 25 mN/m, the DMPG monolayer contains predominantly the LC phase. Ten minutes after the injection of hTau40 (~5% area expansion), the ratio of dark to light regions is reduced and the general appearance of the LC domains changed from a well-defined circular shape to one that is less well-defined, indicative of decreased line tension around the LC domains (Figure 2.5B). These changes in the monolayer morphology became more pronounced with continued insertion of hTau40, where, in addition to decreased dark to light regions, the dark LC domains are also smaller in general, pointing to the disruption of LC domains. Note, however, the LC domain boundaries remained distinct.

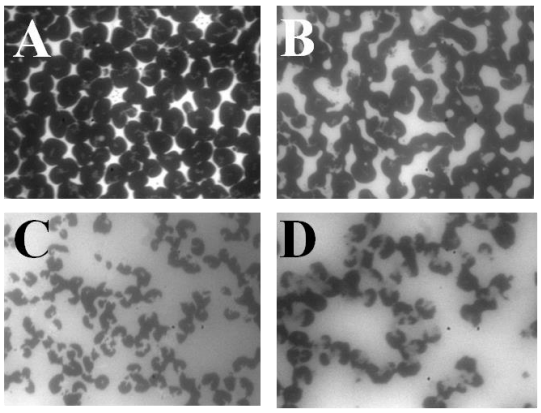


Figure 2.5 FM images of a DMPG lipid monolayer during hTau40 insertion.

The FM images in Figure 2.5 were collected (A) before tau injection, and (B) 10, (C) 30, and (D) 120 minutes after injection, corresponding to ~ 5%, 14%, and 45% area expansion, respectively.

### 2.3.3 *X-ray scattering measurements of hTau40 associated with lipid monolayers*

GIXD data of hTau40 associated with a DMPG monolayer showed that the insertion of tau disrupted lipid packing (Figure 2.6). The DMPG monolayer at 25 mN/m showed a single Bragg peak. The $Q_{xy}$ position of the peak maximum (1.483 $Å^{-1}$) corresponds to a *d*-spacing of 4.237 Å and the 2D hexagonal unit cell dimension, $a_h$, is 4.893 Å. The area per DMPG molecule is 41.47 $Å^2$ and the average size of the ordered domains is ~270 Å. No diffraction peaks were observed after tau inserted into the monolayer (Figure 2.6). Tau associated with the DMPG monolayer did not show any scattering peaks (data not shown), indicating that the protein did not fold and order into domains detectable by GIXD. Qualitatively, reflectivity profiles of tau-associated DMPG

monolayer exhibited significant differences compared to that of lipids alone (Figure 2.7). XR data of the DMPG monolayer before and at two different time points (t1 and t2) after the injection of hTau40 are shown for comparison. Qualitatively, reflectivity of the DMPG film alone showed the characteristic "two humps" of the lipid monolayer, one corresponding to the lipid headgroups and the second to the alkyl tails. After the addition of tau, significant differences in the reflectivity were observed in a time-dependent manner. Minima in the reflectivity curves became shallower and the overall intensity of the signals decreased. Fitting parameters are summarized in Table 2.2.

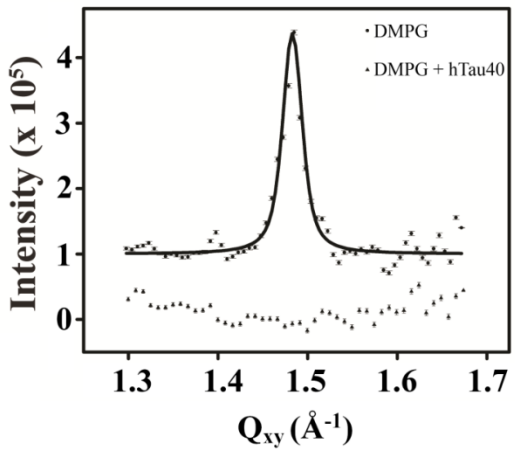


Figure 2.6 Background subtracted GIXD data of DMPG and DMPG/tau monolayers at 23 °C.

Figure 2.6 illustrates that the DMPG monolayer at 25 mN/m showed a single Bragg peak whereas no peaks were observed from the DMPG/tau film. Data are offset for clarity.

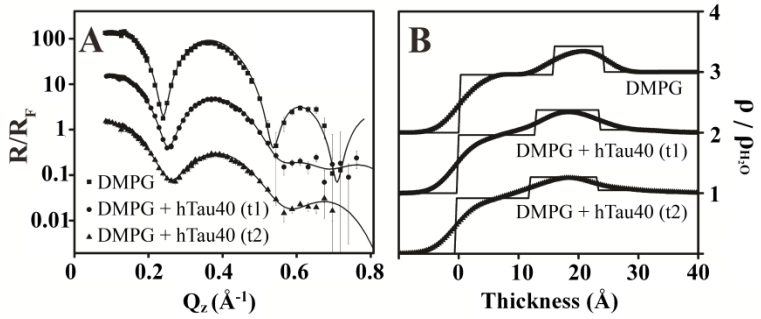


Figure 2.7 Fresnel normalized X-ray reflectivity (R/RF) of DMPG and DMPG/hTau40 monolayers at 23 °C.

As illustrated in Figure 2.7, pure DMPG and the DMPG/hTau40 (time t1) data were collected at 25 mN/m. t2 data was collected at a slightly higher pressure since tau insertion caused an area expansion beyond maximum trough area. Panel A of the figure shows the model independent fits (solid lines) of the XR data obtained from StochFit, which correspond to water normalized electron density distributions shown in panel B. Box model fit of the electron density profiles are also shown. Data are offset for clarity.

Table 2.2 X-ray Parameters for hTau40 Insertion into DMPG Monolayer[a]

| Sample | Box Composition | Thickness (Å) | ρ / $\rho_{H20}$ | Roughness (Å) |
|---|---|---|---|---|
| **DMPG** | Lipid tails | 14.9 ± 5.1 E-2 | 0.94 ± 1.2 E-2 | 3.11 ± 1.5 E-3 |
| | Lipid headgroups | 9.78 ± 9.7 E-2 | 1.37 ± 1.5 E-2 | 2.91 ± 4.6 E-3 |
| **+ hTau40 t1** | Lipid tails | 13.4 ± 5.4 E-2 | 0.93 ± 1.4 E-2 | 2.96 ± 1.2 E-2 |
| | Lipid tails + headgroups + hTau40 | 10.3 ± 1.0 E-1 | 1.32 ± 1.6 E-3 | 3.19 ± 1.8 E-2 |
| | hTau40 | 10.1 ± 1.6 E-2 | 1.01 ± 2.9 E-3 | 3.33 ± 1.6 E-2 |
| **+ hTau40 t2** | Lipid tails | 12.3 ± 2.7 E-1 | 0.91 ± 1.5 E-2 | 3.25 ± 1.1 E-2 |
| | Lipid tails + headgroups + hTau40 | 11.2 ± 3.4 E-1 | 1.25 ± 2.9 E-2 | 3.25 ± 2.3 E-2 |
| | hTau40 | 9.1 ± 1.4 E0 | 1.04 ± 3.3 E-1 | 2.33 ± 4.3 E-2 |

[a] Errors reported are standard deviations obtained from the nonlinear least-squares fitting of the reflectivity data with box models using the Levenberg-Marquadt algorithm (Danauskas et al., 2011).

Analysis of the XR data using the StochFit model (Danauskas et al., 2008) yielded $\rho/\rho_{H2O}$ distribution perpendicular to the air/water interface (Figure 2.7B). As shown, upon injection of hTau40, $\rho/\rho_{H2O}$ in the headgroup region of DMPG decreased and the length of this region increased. Additionally a region of slightly higher $\rho/\rho_{H2O}$ adjacent to the DMPG headgroup on the subphase side was required to fit the data. The size of this region corresponds to hTau40 inserted into the DMPG monolayer, thus confirming the strong association of tau with the negatively charged membrane.

### 2.3.4 *Neutron reflectivity measurements of hTau40 and supported lipid bilayers*

Figures 2.8 and 2.9 summarize the NR data obtained before and after the injection of hTau40 into DPPC and DMPG lipid bilayers, respectively. DPPC was chosen instead of the more fluid DMPC to obtain a more stable bilayer *vis-à-vis* the solid support. Similar to the XR data, the NR results are normalized by Fresnel to highlight important features. Intact bilayers are indicated by a distinctive "two-hump" pattern, with each peak representing an intact monolayer, whereas bilayers that have been disrupted lack these two peaks (Figure 2.9C). Figure 2.8 shows the NR and corresponding SLD profile for a DPPC bilayer, deposited at 25 mN/m before (Figure 2.8A and 2.8B) and after (Figure 2.8C and 2.8D) the injection of hTau40 in the subphase. A cartoon depiction for these two cases is also shown. The parameters are summarized in Table 2.3. Our data show that the addition of hTau40 did not have any effect on the DPPC membrane structure. In contrast, the addition of hTau40 completely disrupted a DMPG bilayer deposited at 40 mN/m (Figure 2.9C and 2.9D). A similar effect was observed for a DMPG bilayer deposited at 25 mN/m (data not shown). Note that, unlike DPPC, DMPG deposited at 25 and 40 mN/m showed a lower surface occupancy as seen from the SLD of the bilayer.

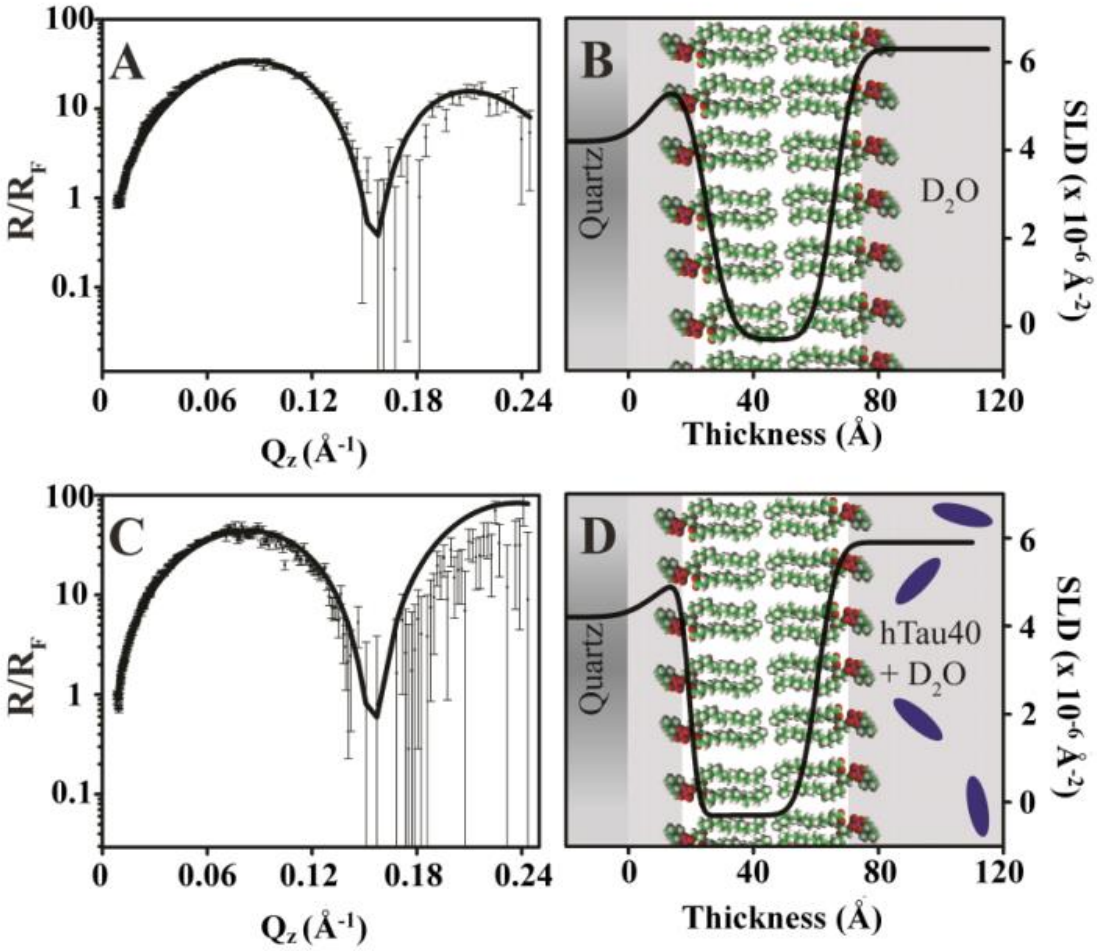


Figure 2.8 Fresnel normalized X-ray reflectivity and corresponding SLD profiles for a DPPC bilayer.

In Figure 2.8, Fresnel normalized X-ray reflectivity ($R/R_F$) (A and C) and corresponding SLD profiles (B and D) for a DPPC bilayer deposited onto a quartz substrate at 25 mN/m before (A and B) and after (C and D) tau addition. The lines are the fitted NR and SLD profiles. Schematics depicting lipids and proteins in the system are also included.

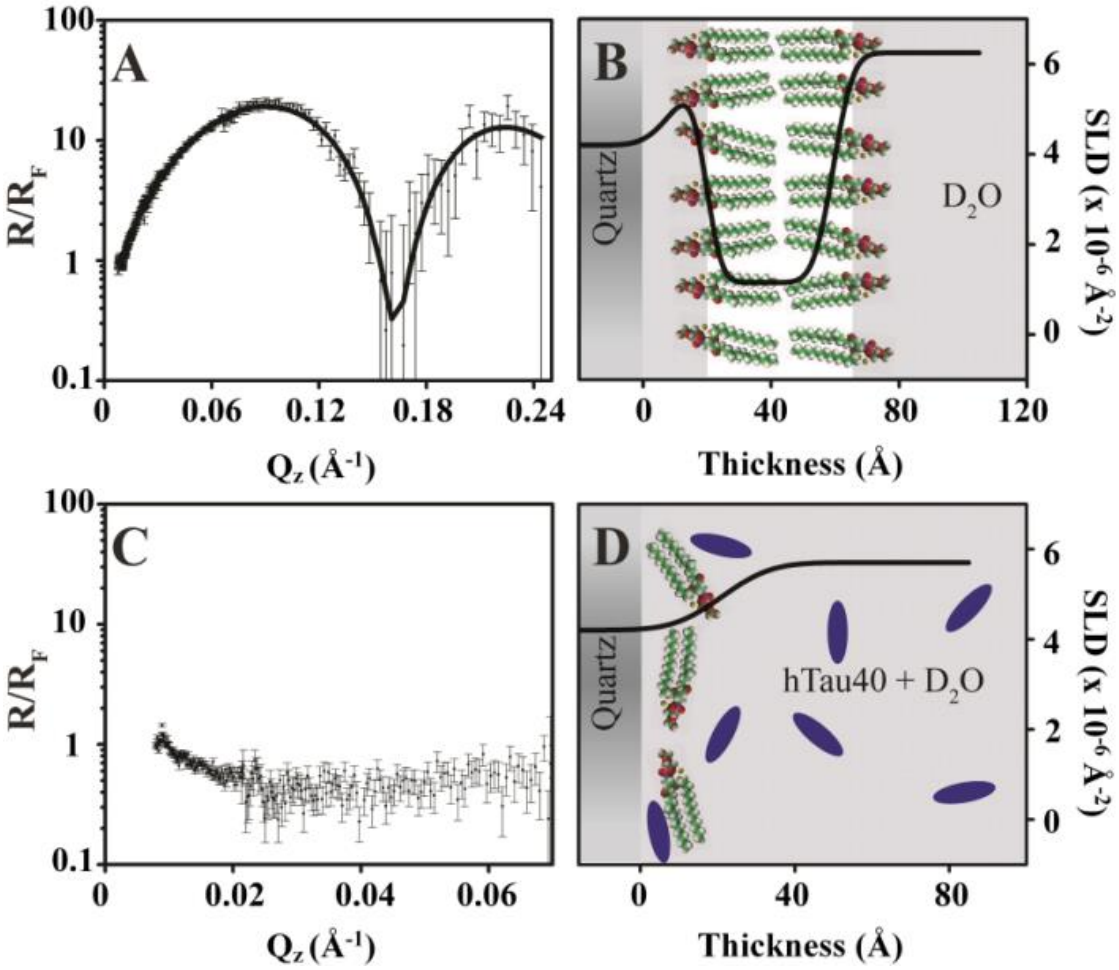


Figure 2.9 Fresnel normalized X-ray reflectivity and corresponding SLD profiles for a DMPG lipid bilayer.

In Figure 2.9, the Fresnel normalized X-ray reflectivity ($R/R_F$) (A and B) and corresponding SLD profiles (B and D) for a DMPG lipid bilayer deposited onto a quartz substrate at 40 mN/m before (A and B) and after (C and D) tau addition are illustrated. The lines are the fitted NR and SLD profiles. Schematics depicting lipids and proteins in the system are also included.

Table 2.3 Neutron Reflectivity Least-Squares Fit Parameters

| **Flow Cell Contents** | **Layer Composition** | **Thickness (Å)** | **SLD ($10^{-6}$ Å$^{-2}$)** | **Roughness (Å)** |
|---|---|---|---|---|
| **DPPC 25 mN/m** | $D_2O$ + DPPC heads | 15.9 | 6.00 | 8.00 |
| | DPPC tails | 41.0 | -0.300 | 6.15 |
| **DPPC 25 mN/m + hTau40** | $D_2O$ + DPPC heads | 10.8 | 5.20 | 7.97 |
| | DPPC tails | 41.0 | -0.300 | 2.48 |
| **DMPG 40 mN/m** | $D_2O$ + DMPG heads | 10.9 | 5.64 | 6.82 |
| | DMPG tails | 39.7 | 1.15 | 3.82 |

## 2.4 Discussion

### 2.4.1 *hTau40 is highly surface active*

Although highly charged and soluble, the full-length human recombinant hTau40 exhibited significant surface activity, adsorbing readily to the air/water interface to give a final π comparable to that reached by the adsorption of the amphipathic Aβ40 peptide to an air/water interface (Ege & Lee, 2004). The intrinsically disordered, or "soft" nature, of the tau protein thus renders it highly surface active, prone to partition or bind to different interfaces. The initial sharp increase in π (Figure 2.2) is indicative of hTau40's high affinity to the hydrophobic interface and the reproducible two-stage adsorption behavior suggests that the protein undergoes structural rearrangements once adsorbed to the interface.

### 2.4.2 *hTau40 selectively interacts with anionic membranes*

To understand the role lipid membranes play in mediating the dynamics of hTau40, we investigated the interactions between model lipid membranes and hTau40. The Langmuir monolayer is used to model one leaflet of the plasma membrane, while the supported lipid bilayers provide a better model of the plasma membrane. As demonstrated by the monolayer insertion assays, hTau40 strongly associated and inserted into the anionic DMPG monolayer, presumably in part mediated by the attractive electrostatic interactions between the positively charged MT binding domain of hTau40 (Figure 2.1A) and the lipids. The strong affinity of the MT binding domain with anionic membranes is also in agreement with previous reports on the tau repeat domain construct (K18), which forms the core of the paired-helical filaments, aggregating in the presence of anionic lipid vesicles (Elbaum-Garfinkle et al., 2010). Tau also favorably interacted with positively charged DMTAP, presumably through its negatively charged projection N-terminus, but inserted to a much lesser extent compared to DMPG. hTau40 did not exhibit any favorable interactions with the neutral DMPC lipids. The selective affinity of hTau40 towards anionic membranes is further evidenced by the complete disruption of a supported DMPG bilayer while leaving DPPC bilayer intact (Figure 2.8 and 2.9). Our findings suggest that electrostatic interactions play an important role in modulating tau-membrane interactions, with hTau40 displaying a strong affinity toward the anionic DMPG membrane. However, the extent of tau interaction with membranes could be mediated by additional factors, as evidenced by the disparate extents of insertion into anionic and cationic membranes. Further

investigations utilizing different tau mutants will help to clarify the importance of these factors.

### 2.4.3 *Air/water and lipid membrane interfaces induce tau structural compaction*

The tau film adsorbed to the air/water interface is about 20 Å thick and is not homogeneous in its electron density distribution perpendicular to the film surface (Figure 2.3). A more dense ~10 Å layer with a $\rho/\rho_{H2O}$ of 1.3 is formed at the hydrophobic air phase, followed by a more diffuse layer with a $\rho/\rho_{H2O}$ close to 1 that extends another 10 Å into the water phase. The radius of gyration ($R_g$) of the intrinsically disordered hTau40 in solution (determined by small-angle X-ray scattering) has been reported to be 65 Å (Bernadó et al., 2007), much larger than a globular, folded protein of ~400 amino acids with $R_g$ typically ranging from 20-25 Å. In addition, a $\rho/\rho_{H2O}$ of 1.3 of the more dense hTau40 layer at the air phase is comparable to the density of folded proteins that have an average specific volume of 0.73, which corresponds to a density of 1.37 g/ml (Lee & Timasheff, 1974). XR data modeling of tau inserted into a DMPG monolayer show that the membrane association and partial insertion of tau into the lipid headgroup region gave rise to a 10-20 Å layer of protein at the lipid interface with a $\rho/\rho_{H2O}$ of about 1.3 (Figure 2.7B).

Our structural measurements of air/water interface-adsorbed and membrane interface-associated tau layers of smaller dimension and higher density compared to tau in solution thus suggest that as the intrinsically disordered tau adsorbs to the air/water interface, at least a portion of the protein undergoes structural compaction to resemble the density of a folded protein. Structurally compacted conformations of the full-length tau protein that exhibit enhanced aggregation propensity have been shown in several cases, including phosphorylation at several sites diagnostic of AD (Jeganathan et al., 2008;

Jeganathan et al., 2006), binding to exogenous aggregation inducers ( Chirita et al., 2005), and fast heating/cooling (Shkumatov et al., 2011). We show here that the partition and binding of tau to two different interfaces, including a physiological membrane interface, can also induce structural compaction. Our data, along with previous reports, clearly demonstrate that structural plasticity of the tau protein and that multiple mechanisms can induce structural compaction that accompanies disordered-to-order transitions in the protein to render it aggregation-competent. However, the exact nature of the air/water and membrane interface-induced folding of tau is not clear. The interfacial tau films appear to be amorphous in long-range order, as no ordered crystalline domains were detectable by GIXD. But the lack of long-range order does not preclude the formation of local, whether intramolecular or intermolecular, secondary structures, which can render the otherwise soluble and stable tau "pro-aggregant" or aggregation-competent.

### 2.4.4 *hTau40 association with membranes disrupts lipid packing and membrane integrity*

Morphological changes to the DMPG lipid monolayer caused by the insertion of tau were observed by FM. As previously shown in Aβ-membrane studies (Bokvist et al., 2004; Ege & Lee, 2004), changes in monolayer morphology can be indicative of disruption to lipid packing. An overall increase in the ratio of light to dark regions indicates preferential insertion of the protein into the LE phase and also a change from a LC to a LE phase. For hTau40 insertion into negatively charged DMPG, this ratio grew with an increase in the % area expansion until ~45% expansion, at which point the % area expansion continued to increase without any appreciable differences in monolayer images.

One possible explanation for this finding is that beyond 45% expansion the DMPG monolayer was no longer compressed enough to provide steric inhibition of dye movement. On the molecular level, GIXD data of hTau40 associated with DMPG monolayers showed that the insertion of the protein completely disrupted lipid packing and eliminated the ordered LC phase.

NR assays used to assess lipid bilayer structure before and after insertion of hTau40 showed that tau selectively disrupted anionic DMPG lipid bilayers even at lipid packing densities higher than those of a cell membrane. Tau disrupted DMPG bilayers deposited at both 25 and 40 mN/m. In contrast, the neutrally charged DPPC bilayer was not affected by the addition of tau. These results confirm that hTau40 preferentially interacts with anionic membranes, not only with a DMPG monolayer at the air-water interface, but also with a more physiologically relevant bilayer system. Moreover, these interactions disrupt lipid membrane structure, both on a molecular scale of disrupting lipid packing and on a morphological scale of completely disrupting the integrity of lipid bilayers.

## 2.5 Conclusions

Our results provide some insights into the driving forces of the folding and aggregation of the AD-associated protein hTau40. We hypothesize that the aggregation of the highly charged, soluble, and intrinsically disordered tau is catalyzed by the formation of a structurally compact, pro-aggregant conformation, followed by energetically favorable assembly reactions to form larger aggregates. Normally, tau aggregation requires exogenous polyanionic cofactors. We examine here the interaction of tau with the more

physiological lipid membranes and the effect of these interactions on tau conformation and membrane integrity. The "soft nature" of the protein gives rise to a high surface activity as evidenced by tau's high affinity to partition to the hydrophobic air/water interface. Tau also has a strong tendency to associate with negatively charged lipid monolayer and bilayer surfaces. Both interfaces induce the intrinsically disordered hTau40 to partially adopt a more compact conformation similar to that of a folded protein. This interface-induced compaction may serve to seed the aggregation of tau. Tau's interaction with anionic lipid monolayers disrupted lipid packing and compromised integrity of the lipid bilayer, suggesting a mechanism of protein aggregate-induced toxicity in diseased cells. Further study of lipid membrane interaction with hyperphosphorylated forms of tau will provide more understanding of tau-mediated neurodegenerative processes.

**Acknowledgements**

We gratefully acknowledge support from the Alzheimer's Association, UNM Research Allocation Committee, and Oak Ridge Associated Universities. EMJ acknowledges fellowship support from the NSF-IGERT program "Integrative Nanoscience and Microsystems" and the NCI Alliance for Nanotechnology in Cancer. EM and JB acknowledge support from the Max-Planck-Society and Volkswagen Foundation. This work benefited from the use of the Lujan Neutron Scattering Center at LANSCE funded by the DOE Office of Basic Energy Sciences and Los Alamos National Laboratory under DOE Contract DE-AC52-06NA25396 and the BW1 Beamline at the Deutsches Elektronen-Synchrotron in Hamburg, Germany.

## 2.6 References


Alsnielsen, J., & Kjaer, K. (1989 April 4 - April 14, 1989). *X-ray reflectivity and diffraction studies of liquid surfaces and surfactant monolayers.* Paper presented at the proceedings of the NATO Advanced Study Institute, Phase Transitions in Soft Condensed Matter, Geilo, Norway.

Arispe, N., Pollard, H. B., & Rojas, E. (1993). Giant multilevel cation channels formed by Alzheimer-disease amyloid beta-protein [a-Beta-P-(1-40)] in bilayer-membranes. *Proceedings of the National Academy of Sciences of the United States of America, 90*(22), 10573-10577.

Arispe, N., Pollard, H. B., & Rojas, E. (1994). The ability of amyloid beta-protein [A beta P (1-40)] to form Ca2+ channels provides a mechanism for neuronal death in Alzheimer's disease. *Ann N Y Acad Sci, 747*, 256-266.

Barghorn, S., & Mandelkow, E. (2002). Toward a unified scheme for the aggregation of tau into Alzheimer paired helical filaments. *Biochemistry, 41*(50), 14885-14896.

Berger, Z., Roder, H., Hanna, A., Carlson, A., Rangachari, V., Yue, M., et al. (2007). Accumulation of pathological tau species and memory loss in a conditional model of tauopathy. *The Journal of Neuroscience, 27*(14), 3650-3662.

Bernadó, P., Mylonas, E., Petoukhov, M. V., Blackledge, M., & Svergun, D. I. (2007). Structural characterization of flexible proteins using small-angle X-ray scattering. *Journal of the American Chemical Society, 129*(17), 5656-5664.

Bokvist, M., Lindström, F., Watts, A., & Gröbner, G. (2004). Two types of Alzheimer's [beta]-amyloid (1-40) peptide membrane interactions: Aggregation preventing transmembrane anchoring versus accelerated surface fibril formation. *Journal of Molecular Biology, 335*(4), 1039-1049.

Brandt, R., Léger, J., & Lee, G. (1995). Interaction of tau with the neural plasma membrane mediated by tau's amino-terminal projection domain. *The Journal of Cell Biology, 131*(5), 1327-1340.

Buée, L., Bussière, T., Buée-Scherrer, V., Delacourte, A., & Hof, P. R. (2000). Tau protein isoforms, phosphorylation and role in neurodegenerative disorders. *Brain Research Reviews, 33*(1), 95-130.

Campos-Peña, V., Tapia-Ramírez, J., Sánchez-Torres, C., & Meraz-Rios, M. A. (2009). Pathological-like assembly of tau induced by a paired helical filament core expressed at the plasma membrane. [10.3233/JAD-2009-1198]. *Journal of Alzheimer's Disease, 18*(4), 919-933.

Chi, E. Y., Ege, C., Winans, A., Majewski, J., Wu, G., Kjaer, K., et al. (2008). Lipid membrane templates the ordering and induces the fibrillogenesis of Alzheimer's disease amyloid-beta peptide. *Proteins, 72*(1), 1-24.

Chi, E. Y., Frey, S. L., & Lee, K. Y. C. (2007). Ganglioside GM1-mediated amyloid-beta fibrillogenesis and membrane disruption. *Biochemistry, 46*(7), 1913-1924.

Chi, E. Y., Frey, S. L., Winans, A., Lam, K. L. H., Kjaer, K., Majewski, J., et al. (2010). Amyloid-[beta] fibrillogenesis seeded by interface-induced peptide misfolding and self-assembly. *Biophysical Journal, 98*(10), 2299-2308.

Chirita, C., Necula, M., & Kuret, J. (2003). Anionic micelles and vesicles induce tau fibrillization in vitro. *Journal of Biological Chemistry, 278*(28), 25644-25650.

Chirita, C. N., Congdon, E. E., & Kuret, J. (2005). Triggers of full-length tau aggregation: a role for partially folded. *Biochemistry, 44*(15), 5862-5872.

Cleveland, D. W., Hwo, S.-Y., & Kirschner, M. W. (1977). Physical and chemical properties of purified tau factor and the role of tau in microtubule assembly. *Journal of Molecular Biology, 116*(2), 227-247.

Conway, K. A., Lee, S.-J., Rochet, J.-C., Ding, T. T., Williamson, R. E., & Lansbury, P. T. (2000). Acceleration of oligomerization, not fibrillization, is a shared property of both α-synuclein mutations linked to early-onset Parkinson's disease: Implications for pathogenesis and therapy. *Proceedings of the National Academy of Sciences, 97*(2), 571-576.

Danauskas, S. M., Li, D., Meron, M., Lin, B., & Lee, K. Y. C. (2008). Stochastic fitting of specular X-ray reflectivity data using StochFit. *Journal of Applied Crystallography, 41*(6), 1187-1193.

Demuro, A., Mina, E., Kayed, R., Milton, S. C., Parker, I., & Glabe, C. G. (2005). Calcium dysregulation and membrane disruption as a ubiquitous neurotoxic mechanism of soluble amyloid oligomers. *J Biol Chem, 280*(17), 17294-17300.

Deshpande, A., Mina, E., Glabe, C., & Busciglio, J. (2006). Different conformations of amyloid beta induce neurotoxicity by distinct mechanisms in human cortical neurons. *J Neurosci, 26*(22), 6011-6018.

Deshpande, A., Win, K. M., & Busciglio, J. (2008). Tau isoform expression and regulation in human cortical neurons. *The FASEB Journal, 22*(7), 2357-2367.

Dubey, M., Jablin, M. S., Smith, H., & Majewski, J. (2010). Investigations of surrogate cellular membranes using neutron reflectometry. *Acta Crystallographica Section D, 66*(11), 1237-1243.

Ege, C., & Lee, K. Y. C. (2004). Insertion of Alzheimer's A[beta]40 peptide into lipid monolayers. *Biophysical Journal, 87*(3), 1732-1740.

Elbaum-Garfinkle, S., Ramlall, T., & Rhoades, E. (2010). The role of the lipid bilayer in tau aggregation. *Biophysical Journal, 98*(11), 2722-2730.

Gendron, T. F., & Petrucelli, L. (2009). The role of tau in neurodegeneration. *Molecular Neurodegeneration, 4*(1), 13.

Gidalevitz, D., Ishitsuka, Y., Muresan, A. S., Konovalov, O., Waring, A. J., Lehrer, R. I., et al. (2003). Interaction of antimicrobial peptide protegrin with biomembranes. *Proceedings of the National Academy of Sciences, 100*(11), 6302-6307.

Goedert, M., Jakes, R., Spillantini, M. G., Hasegawa, M., Smith, M. J., & Crowther, R. A. (1996). Assembly of microtubule-associated protein tau into Alzheimer-like filaments induced by sulphated glycosaminoglycans. [10.1038/383550a0]. *Nature, 383*(6600), 550-553.

Gray E.G., M., P.-B., & Roher, A. (1987). Alzheimer's disease: Paired helical filaments and cytomembranes. *Neuropathol Appl Neurobiol, 13*(2), 91-110.

Jeganathan, S., Hascher, A., Chinnathambi, S., Biernat, J., Mandelkow, E.-M., & Mandelkow, E. (2008). Proline-directed Pseudo-phosphorylation at AT8 and PHF1 epitopes induces a compaction of the paperclip folding of tau and generates a pathological (MC-1) conformation. *Journal of Biological Chemistry, 283*(46), 32066-32076.

Jeganathan, S., von Bergen, M., Brutlach, H., Steinhoff, H.-J., & Mandelkow, E. (2006). Global hairpin folding of tau in solution. *Biochemistry, 45*(7), 2283-2293.

Kawarabayashi, T., Shoji, M., Younkin, L. H., Wen-Lang, L., Dickson, D. W., Murakami, T., et al. (2004). Dimeric amyloid β protein rapidly accumulates in lipid rafts followed by apolipoprotein E and phosphorylated tau accumulation in the Tg2576 mouse model of Alzheimer's disease. *The Journal of Neuroscience, 24*(15), 3801-3809.

Kayed, R., Sokolov, Y., Edmonds, B., McIntire, T. M., Milton, S. C., Hall, J. E., et al. (2004). Permeabilization of lipid bilayers is a common conformation-dependent activity of soluble amyloid oligomers in protein misfolding diseases. *J Biol Chem, 279*(45), 46363-46366.

King, M. E., Gamblin, T. C., Kuret, J., & Binder, L. I. (2000). Differential assembly of human tau isoforms in the presence of arachidonic acid. [10.1046/j.1471-4159.2000.0741749.x]. *Journal of Neurochemistry, 74*(4), 1749-1757.

Kjaer, K. (1994). Some simple ideas on X-Ray reflection and grazing-incidence diffraction from thin surfactant films. *Physica B-Condensed Matter, 198*(1-3), 100-109.

Knobler, C. M. (1990). Seeing phenomena in flatland: Studies of monolayers by fluorescence microscopy. *Science, 249*(4971), 870-874.

Kosik, K. S., Joachim, C. L., & Selkoe, D. J. (1986). Microtubule-associated protein tau (tau) is a major antigenic component of paired helical filaments in Alzheimer disease. *Proceedings of the National Academy of Sciences, 83*(11), 4044-4048.

Lashuel, H. A., Petre, B. M., Wall, J., Simon, M., Nowak, R. J., Walz, T., et al. (2002). [alpha]-Synuclein, especially the Parkinson's disease-associated mutants, forms pore-like annular and tubular protofibrils. *Journal of Molecular Biology, 322*(5), 1089-1102.

Lee, J. C., & Timasheff, S. N. (1974). Partial specific volumes and interactions with solvent components of proteins in guanidine hydrochloride. *Biochemistry, 13*(2), 257-265.

Lee, V. M. Y., Goedert, M., & Trojanowski, J. Q. (2001). Neurodegenerative tauopathies. *Annual Review of Neuroscience, 24*(1), 1121-1159.

Lovestone, S., & McLoughlin, D. M. (2002). Protein aggregates and dementia: Is there a common toxicity? *Journal of Neurology, Neurosurgery & Psychiatry, 72*(2), 152-161.

Novitskaya, V., Bocharova, O. V., Bronstein, I., & Baskakov, I. V. (2006). Amyloid fibrils of mammalian prion protein are highly toxic to cultured cells and primary neurons. *Journal of Biological Chemistry, 281*(19), 13828-13836.

Poorkaj, P., Bird, T. D., Wijsman, E., Nemens, E., Garruto, R. M., Anderson, L., et al. (1998). Tau is a candidate gene for chromosome 17 frontotemporal dementia. *Ann Neurol, 43*(6), 815-825.

Quist, A., Doudevski, I., Lin, H., Azimova, R., Ng, D., Frangione, B., et al. (2005). Amyloid ion channels: a common structural link for protein-misfolding disease. *Proc Natl Acad Sci U S A, 102*(30), 10427-10432.

Seelig, A. (1987). Local anesthetics and pressure: a comparison of dibucaine binding to lipid monolayers and bilayers. *Biochimica et Biophysica Acta (BBA) - Biomembranes, 899*(2), 196-204.

Selkoe, D. J. (2000). Toward a comprehensive theory for Alzheimer's disease. Hypothesis: Alzheimer's disease is caused by the cerebral accumulation and cytotoxicity of amyloid β-protein. *Annals of the New York Academy of Sciences, 924*(1), 17-25.

Sharon, R., Bar-Joseph, I., Frosch, M. P., Walsh, D. M., Hamilton, J. A., & Selkoe, D. J. (2003). The formation of highly soluble oligomers of [alpha]-synuclein is regulated by fatty acids and enhanced in Parkinson's disease. *Neuron, 37*(4), 583-595.

Shkumatov, A. V., Chinnathambi, S., Mandelkow, E., & Svergun, D. I. (2011). Structural memory of natively unfolded tau protein detected by small-angle X-ray scattering. [10.1002/prot.23033]. *Proteins: Structure, Function, and Bioinformatics, 79*(7), 2122-2131.

Simakova, O., & Arispe, N. J. (2007). The cell-selective neurotoxicity of the Alzheimer's Abeta peptide is determined by surface phosphatidylserine and cytosolic ATP levels. Membrane binding is required for Abeta toxicity. *J Neurosci, 27*(50), 13719-13729.

Sokolov, Y., Kozak, J. A., Kayed, R., Chanturiya, A., Glabe, C., & Hall, J. E. (2006). Soluble amyloid oligomers increase bilayer conductance by altering dielectric structure. *J Gen Physiol, 128*(6), 637-647.

Soto, C. (2003). Unfolding the role of protein misfolding in neurodegenerative diseases. [10.1038/nrn1007]. *Nat Rev Neurosci, 4*(1), 49-60.

Spillantini, M. G., & Goedert, M. (1998). Tau protein pathology in neurodegenerative diseases. *Trends in Neurosciences, 21*(10), 428-433.

Sun, X. D., Mo, Z. L., Taylor, B. M., & Epps, D. E. (2003). A slowly formed transient conformer of A beta(1-40) is toxic to inward channels of dissociated hippocampal and cortical neurons of rats. *Neurobiology of Disease, 14*(3), 567-578.

Sydow, A., Van der Jeugd, A., Zheng, F., Ahmed, T., Balschun, D., Petrova, O., et al. (2011). Tau-induced defects in synaptic plasticity, learning, and memory are reversible in transgenic mice after switching off the toxic tau mutant. *Journal of Neuroscience, 31*(7), 2511-2525.

Valincius, G., Heinrich, F., Budvytyte, R., Vanderah, D. J., McGillivray, D. J., Sokolov, Y., et al. (2008). Soluble amyloid beta-oligomers affect dielectric membrane properties by bilayer insertion and domain formation: implications for cell toxicity. *Biophys J, 95*(10), 4845-4861.

Walsh, D. M., Klyubin, I., Fadeeva, J. V., Cullen, W. K., Anwyl, R., Wolfe, M. S., et al. (2002). Naturally secreted oligomers of amyloid [beta] protein potently inhibit hippocampal long-term potentiation in vivo. [10.1038/416535a]. *Nature, 416*(6880), 535-539.

Wang, Y., Tang, Y., Zhou, Z., Ji, E., Lopez, G. P., Chi, E. Y., et al. (2010). Membrane Perturbation activity of cationic phenylene ethynylene oligomers and polymers: selectivity against model bacterial and mammalian membranes. *Langmuir, 26*(15), 12509-12514.

Weingarten, M. D., Lockwood, A. H., Hwo, S. Y., & Kirschner, M. W. (1975). A protein factor essential for microtubule assembly. *Proceedings of the National Academy of Sciences, 72*(5), 1858-1862.

Williamson, R., Usardi, A., Hanger, D. P., & Anderton, B. H. (2008). Membrane-bound β-amyloid oligomers are recruited into lipid rafts by a fyn-dependent mechanism. *The FASEB Journal, 22*(5), 1552-1559.

Wilson, D. M., & Binder, L. I. (1997). Free fatty acids stimulate the polymerization of tau and amyloid beta peptides. In vitro evidence for a common effector of pathogenesis in Alzheimer's disease. *American Journal of Pathology, 150*(6), 2181-2195.

# CHAPTER 3 EFFECTS OF HYPERPHOSPHORYLATION AND DOMAIN COMPOSITION ON THE INTERACTION OF TAU PROTEIN WITH MODEL LIPID MEMBRANES

(This chapter was prepared for possible publication collaboratively by Emmalee Jones, Ann Junghans, Jacek Biernat, Eckhard Mandelkow, Jaroslaw Majewski, and Eva Y. Chi)


## Abstract

Tau protein is known to misfold and aggregate in the course of several neurodegenerative diseases, including Alzheimer's disease. Previous studies have demonstrated that the full length hTau40 interacts with negatively charged lipid membranes, initiating both structural compaction of the protein itself and disruption of lipid membrane structure. To better understand both the behavior of the tau in its diseased state and which domains of the protein are involved in its interaction with membranes, we investigated both a mutant tau protein which mimicked a diseased hyperphosphorylated state and tau constructs containing only certain domains of the protein. We found that both the mimic and the constructs interacted strongly with negative membranes.


## 3.1 Introduction

Alzheimer's disease (AD) is a progressive, and ultimately fatal, neurodegenerative disease currently affecting more than five million Americans ("Treatments and Research," 2014). One of the major pathological hallmarks of AD is the misfolding and aggregation of two proteins, amyloid beta (Aβ) and tau. The Aβ protein misfolds and aggregates into extracellular amyloid neuritic plaques, while the microtubule associated protein tau forms intracellular neurofibrillary tangles (NFTs) (Soto, 2003). In addition to AD, NFTs have also been linked to the pathogenesis of over 20 other neurodegenerative disorders,

collectively termed tauopathies (Buée et al., 2000). Tau's role in the development and progression of neurodegenerative diseases is still unclear, but a link between pathological tau aggregation and cognitive impairments has been demonstrated (Gendron & Petrucelli, 2009). Moreover, the identification of multiple tau gene point mutations that result in hereditary tauopathies is evidence that tau malfunction alone is sufficient to cause neurodegeneration (Poorkaj et al., 1998; Spillantini & Goedert, 1998). Investigation of the conditions and triggers for tau's aggregation and toxicity in neurodegenerative diseases is vital.

Tau is primarily expressed in the central nervous system. Its vital function, promoting microtubule (MT) assembly and stability, is mediated by six isoforms. These tau proteins are further regulated by phosphorylation, which decreases tau's binding affinity to MT resulting in the disassociation of tau from MTs (Buée et al., 2000; Cleveland et al., 1977; Weingarten et al., 1975). All of the isoforms have multiple charged and hydrophilic residues, and thus they are highly soluble. Because of its high solubility, tau is also resistant to aggregation. However, tau protein does form aggregates of insoluble paired helical filaments (PHFs) when it is hyperphosphorylated (Ihara et al., 1986; Kosik et al.,1986). Although, as mentioned, tau is highly soluble, *in vitro* aggregation can be induced by polyanionic cofactors such as heparin, which compensate for tau's positive charges (Goedert et al., 1996). Aggregation is largely determined by ionic interactions, with anionic micelles and vesicles demonstrated to promote the aggregation of tau (Chirita et al., 2003; Elbaum-Garfinkle et al., 2010), suggesting that tau aggregation proceeds through a nucleation controlled polymerization pathway. The interactions between tau and the anionic inducers increase the protein's local concentration and

compensate for its positive charges (Barghorn & Mandelkow, 2002; Chirita et al., 2003; Goedert et al., 1996; King et al., 2000; Wilson & Binder, 1997), both of which favor second or higher order reactions such as fibril formation. Several prior lines of research suggest that tau's interaction with the plasma membrane may modulate tau aggregation (Elbaum-Garfinkle et al., 2010; Jones et al., 2012). One hypothesis of the toxic function of amyloid proteins like tau is the misfolded proteins' ability to disrupt the lipid membrane (Demuro et al., 2005; Kayed et al., 2004). This compromises the membrane's biological function as an impermeable barrier.

To understand the molecular basis of early aggregation events and the mechanism by which tau aggregation causes neuronal dysfunction, we have previously examined the interaction of the wild type full-length human tau isoform hTau40 (Figure 3.1) and lipid membranes. Our results provided some structural insights into the dual roles that the lipid membrane plays in catalyzing tau misfolding and aggregation and in serving as a target for tau aggregates to exert toxicity *via* membrane destabilization. The wildtype tau protein was highly surface active, and selectively associated with and intercalated into anionic lipid membranes. The hydrophobic air/water interface and an anionic lipid membrane interface induced the intrinsically disordered hTau40 protein to partially adopt a more compact conformation similar to that of a folded protein. Furthermore, association of hTau40 with anionic membranes disrupted lipid packing and compromised membrane integrity.

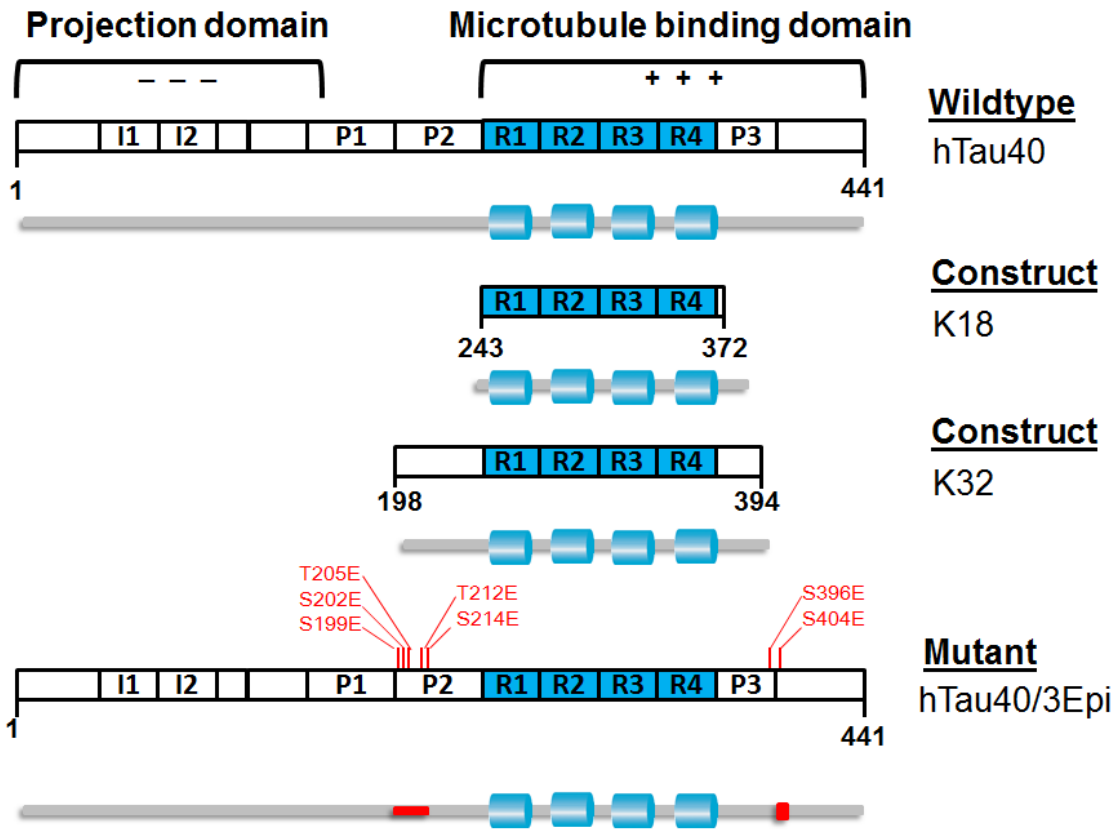


Figure 3.1 Wildtype full length hTau40, tau-derived constructs K18 and K32, and the mutant hTau40/3Epi.

The isoform hTau40, illustrated in Figure 3.1, is the largest one in the human central nervous system (441 residues). In each of the isoforms, the C-terminal half contains three or four pseudorepeats (~31 residues each, R1–R4, blue shade), which are involved in MT binding and form the core of PHFs. The construct K18 represents only the repeat domains of hTau40, comprising four repeats. The construct K32 represents the repeat domains of hTau40 and both of the flanking domains to either side. The "hyperphosphorylated" mutant hTau40/3Epi has nine extra anionic residues, indicated by the red arrows in Figure 3.1.

We now examine the effects of domain composition and hyperphosphorylation on tau-lipid membrane interactions and subsequent membrane-induced tau conformational change and tau-induced membrane disruption. The tau construct K18 consists only of the "repeat domain" in the C-terminal half of tau which contains all four microtubule binding repeats, while the K32 construct contains the repeat domains as well as the two flanking domains to either side (Figure 3.1). Binding to MTs requires both the repeat domains and the flanking domains. When bound to microtubules for its biological function, the C-terminal half of tau adopts α-helical structures, and when assembled into PHFs, the C-terminal half adopts the characteristic β-sheet structure (Chirita et al., 2003; Mandelkow et al., 2007; Mylonas et al., 2008; von Bergen et al., 2005). Anionic lipid vesicles have also been shown to promote the aggregation of the MT binding domain of tau (K18) at sub-micromolar concentrations (Elbaum-Garfinkle et al., 2010). Examination of the K18 and K32 constructs will help to further elucidate which domains of the protein are involved in its misfolding, aggregation and ultimate toxicity.

Tau in PHF is also known to be highly phosphorylated (Wille et al., 1992). In PHF-tau, 19 phosphorylation sites have been identified, and all but Ser-262 are localized to the amino- and carboxyl-terminal flanking regions of the microtubule-binding domain (Morishima-Kawashima et al, 1995). The mutant hTau40/3Epi mimics hyperphosphorylation with 9 extra anionic residues (Figure 3.1) focused in the flanking regions of the microtubule-binding domain. We examine this mutant of the tau protein, hTau40/3Epi, to learn more about the interaction of tau in its diseased state with lipid membranes.

## 3.2 Results

### 3.2.1 *Surface activity of K18, K32 and hTau40/3Epi*

To better understand the effects of domain composition and phosphorylation on tau interaction with hydrophobic interfaces, we compared the surface activity of the wildtype hTau40 protein with that of the K18 and K32 constructs as well as the hTau40/3Epi hyperphosphorylation mimic. Measurement of surface activity assessed the protein's inherent propensity to exhibit exogenous interactions. We measured the surface pressure ($\pi$) reached by the adsorption of the tau proteins to the air/water interface from a water subphase. As shown by the adsorption isotherms in Figure 3.2, all of the proteins adsorbed readily to the air/water interface. The mutant hTau40/3Epi visibly exhibited two-stage adsorption behavior similar to hTau40, possibly reflecting structural rearrangements of the protein layer following rapid adsorption of the protein to the air/water interface. The K32 construct had a lag time of about 15 minutes before adsorbing to the interface, while the K18 construct immediately adsorbed.

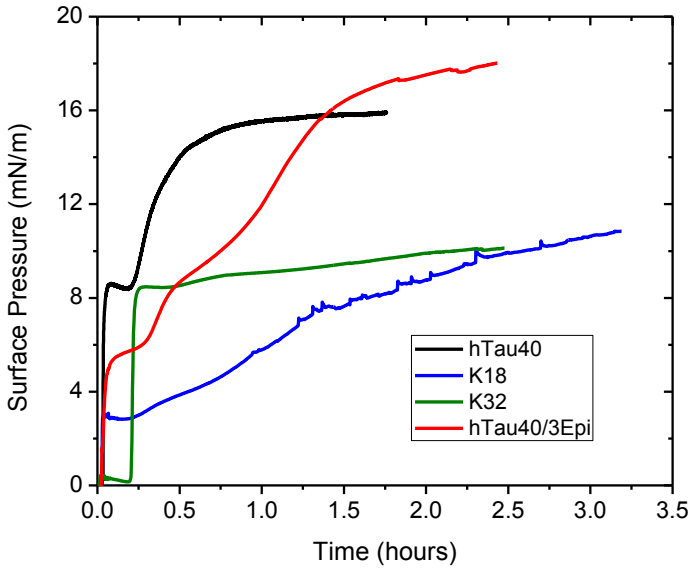


Figure 3.2 Adsorption isotherms for hTau40 (black), K18 construct (blue), K32 construct (green) and mutant hTau40/3Epi (red). Time zero corresponds to the time of protein injection into the subphase.

The XR data obtained for the tau proteins at the air/water interface and the corresponding model independent electron density profiles (ρ, normalized to water, $\rho/\rho_{H2O}$) are shown in Figure 3.3 and fitting parameters are found in Table 3.1. In general, a denser portion is formed at the hydrophobic air phase, followed by a more diffuse layer with lower ρ close to that of water ($\rho/\rho_{H2O} \approx 1$). This disparity in electron densities indicates inhomogeneity of the surface adsorbed tau film in the direction perpendicular to the air/water interface. GIXD data of the films did not show any diffraction peaks (data not

shown), indicating a lack of long-range ordering, in the plane of the film, for any of the tau proteins adsorbed at the air/water interface.

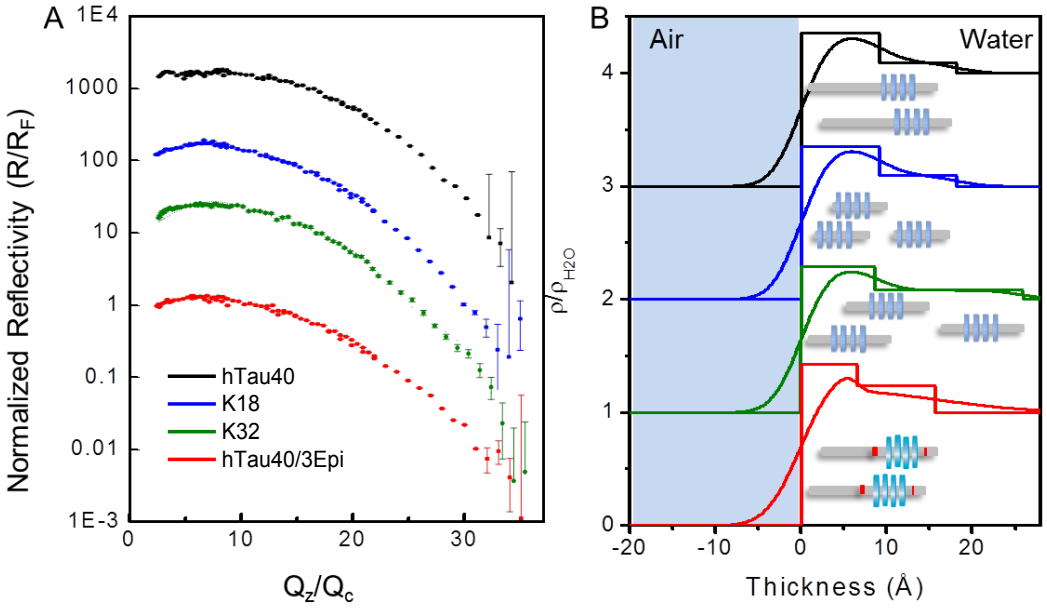


Figure 3.3 X-ray reflectivity (A) and p/pH20 (B) of four tau proteins – hTau40 (black), K18 construct (blue), K32 construct (green), and mutant hTau40/3Epi (red) – adsorbed to air/water interface. Data are offset for clarity.

Table 3.1 X-ray Reflectivity Parameters for Adsorption of Tau to Air/water Interface

| Sample | Box Composition | Thickness (Å) | ρ / $\rho_{H20}$ | Roughness (Å) |
|---|---|---|---|---|
| **hTau40** | air/protein interface | 7.99 ± 2.4 E-2 | 1.27 ± 3.4 E-3 | 2.66 ± 7.4 E-4 |
| | protein/subphase interface | 7.93 ± 8.6 E-2 | 1.02 ± 4.2 E-3 | 2.37 ± 6.4 E-4 |
| **K18** | air/protein interface | 9.38 ± 8.3 E-2 | 1.33 ± 1.7 E-2 | 2.57 ± 7.1 E-3 |
| | protein/subphase interface | 8.58 ± 9.9 E-1 | 1.12 ± 2.0 E-2 | 3.38 ± 1.6 E-2 |
| **K32** | air/protein interface | 8.65 ± 7.3 E-2 | 1.29 ± 1.0 E-2 | 2.51 ± 3.0 E-3 |
| | protein/subphase interface | 17.21 ± 4.7 E-1 | 1.07 ± 1.1 E-2 | 2.12 ± 1.1 E-2 |
| **hTau40/3Epi** | air/protein interface | 6.61 ± 1.4 E-1 | 1.22 ± 1.4 E-2 | 2.57 ± 1.7 E-2 |
| | protein/subphase interface | 9.63 ± 1.6 E-1 | 1.09 ± 2.9 E-3 | 2.57 ± 1.7 E-2 |

### 3.2.2 *Tau construct and hyperphosphorylation mimic insertion into anionic lipid monolayers*

We next examined the effects of domain composition and phosphorylation on tau's interaction with lipid membranes. The % trough area expansions of the tau proteins into a DMPG monolayer held at constant pressure are shown in Figure 3.4A. Time zero of the area expansion corresponds to the time of protein injection into the water subphase *via* an injection port on the side of the trough below the level of the subphase. As previously described, a feedback loop is utilized to maintain constant surface pressure. When the film is perturbed, the barriers move to compensate for the fluctuations in monolayer pressure.

Just as with hTau40, both K18 and hTau40/3Epi inserted readily into the anionic DMPG monolayer held at 25 mN/m. The construct K18 caused an area expansion of over 140% and hTau40/3Epi an expansion of 52%, compared to hTau40's 91% expansion. The K32 construct did insert, but caused an expansion of only 22%.

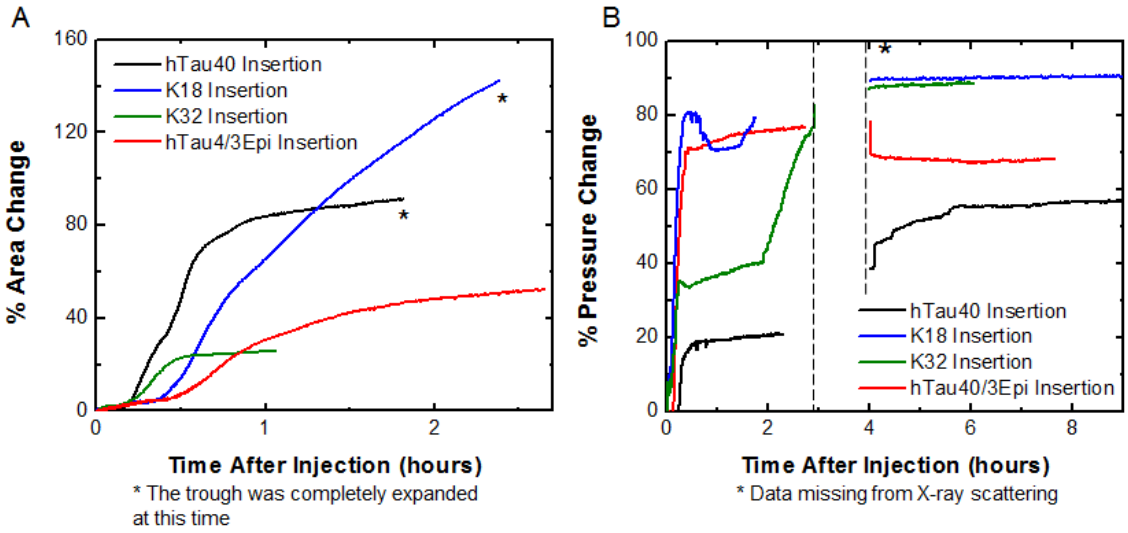


Figure 3.4 % area or pressure change versus time during insertion of hTau40, K18, K32 and hTau40/3Epi mutant proteins into DMPG lipid monolayers.

Figure 3.4 illustrates the % area or pressure change versus time during insertion of hTau40, K18 construct, K32 construct, and hTau40/3Epi mutant proteins into DMPG lipid monolayers held at either constant pressure (A) or constant area (B). Constant pressure assays for hTau40, K18 and hTau40/3Epi were performed at UNM and accompanied by FM imaging to monitor morphology. The constant pressure assay with K32 was performed

at HASYLAB and accompanied by X-ray scattering measurements. All four of the constant area assays also took place at HASYLAB and were accompanied by X-ray scattering.

The pressure increase of the tau construct or mimic into a DMPG monolayer held at constant area is shown in Figure 3.4B. Time zero of the pressure increase corresponds to the time of protein injection into the ~ 25 mL water subphase. In these experiments, a needle was inserted directly into the lipid monolayer from above to inject into the water subphase. The feedback loop in this circumstance was used to maintain constant trough area, and the barriers did not move. All four tau proteins exhibited an immediate increase in surface pressure after injection. The wildtype had a final percent pressure increase of 56%, the mimic hTau40/3Epi an increase of 68%, K18 an increase of 90% and K32 an increase of 88%.

To assess changes in lipid packing and disruption of the constant pressure DMPG monolayers induced by tau protein insertion, we monitored the morphology of the lipid films before and after protein injection. Representative FM images for hTau40, K18, and hTau40/3Epi are shown in Figure 3.5. % area expansion is indicated for each image. At 25 °C, the DMPG monolayer on water undergoes a liquid-expanded (LE) to liquid-condensed (LC) phase transition at ∼17 mN/m (Jones et al., 2012). Because the bulky lipid dye molecules, TR-DHPE, are preferentially excluded from the ordered LC phase, it appears as dark domains in FM whereas the fluid LE phase containing the dyes is bright.

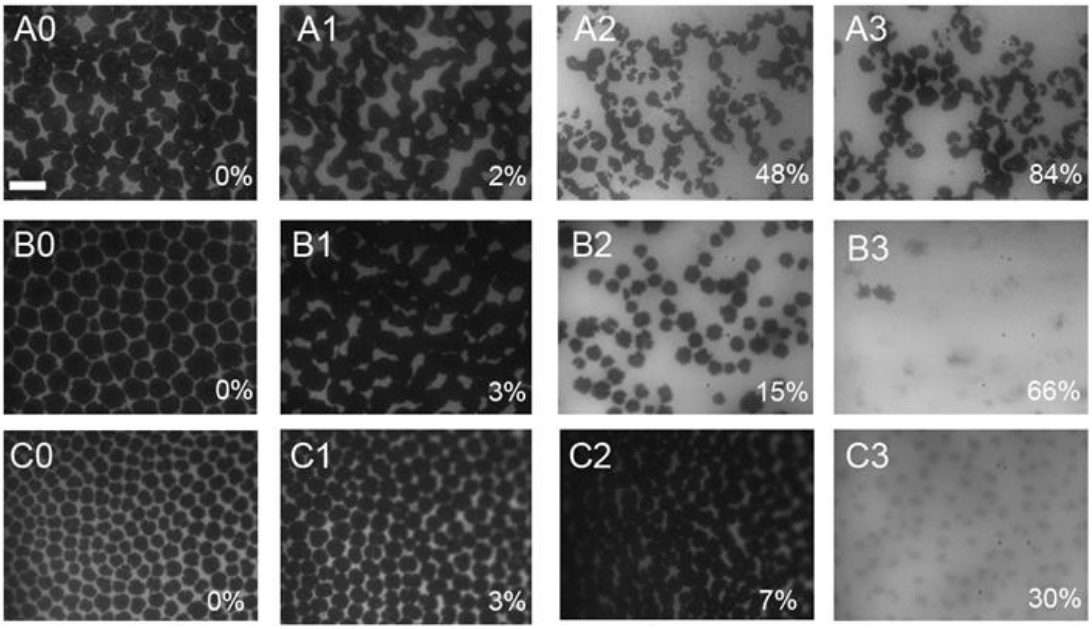


Figure 3.5 FM images of the DMPG monolayer for the hTau40 (A), K18 (B) and hTau40/3Epi (C).

FM images in Figure 3.5 of the DMPG monolayer for the hTau40 (A), K18 (B) and hTau40/3Epi (C) constant pressure insertion experiments were collected at UNM. K32 were not obtained due to limited protein sample. The images were collected right before injection of the protein (0), 10 minutes after injection (1), 30 minutes after injection (2), and 60 minutes after injection (3). The scale bar is equal to 25 μm and the percentages overlaid on each image correspond to the % area expansion at the time each image was collected.

Figures 3.5A0, 3.5B0 and 3.5C0 show that at 25 mN/m the DMPG monolayer contains predominantly the LC phase. Ten minutes after injection (Figure 3.5A1, 3.5B1, 3.5C1), the appearance in general of the LC domains changed from a well-defined circular

shape to one that is less well-defined, indicative of decreased line tension around the LC domains due to the association of the tau proteins to the lipid monolayer (Figure 3.5A2, 3.5B2, 3.5C2). Thirty minutes after injection, the ratio of dark to light regions is reduced. The dark LC domains also became smaller, pointing to the disruption of these ordered domains. One hour after injection (Figure. 3.5A3, 3.5B3, 3.5C3), these changes are even further pronounced.

### 3.2.3 *X-ray scattering measurements of tau constructs and mutant associated with lipid monolayers*

XR profiles of DMPG monolayers held at constant area with tau proteins injected underneath showed significant differences compared to that of lipids alone (Figure 3.6A, 3.7A, 3.8A, 3.9A). XR data before and at two different timepoints (t1=4 hours and t2= 7 hours) after the tau protein injections are shown for comparison. Qualitatively, reflectivity of the DMPG film alone showed the characteristic “two humps” of the lipid monolayer: one corresponding to the lipid headgroups and the second to the alkyl tails. After the injection of the tau proteins, significant differences in the reflectivity were observed in a time-dependent manner. Overall, minima in the reflectivity curves became shallower and the overall intensity of the signals decreased.

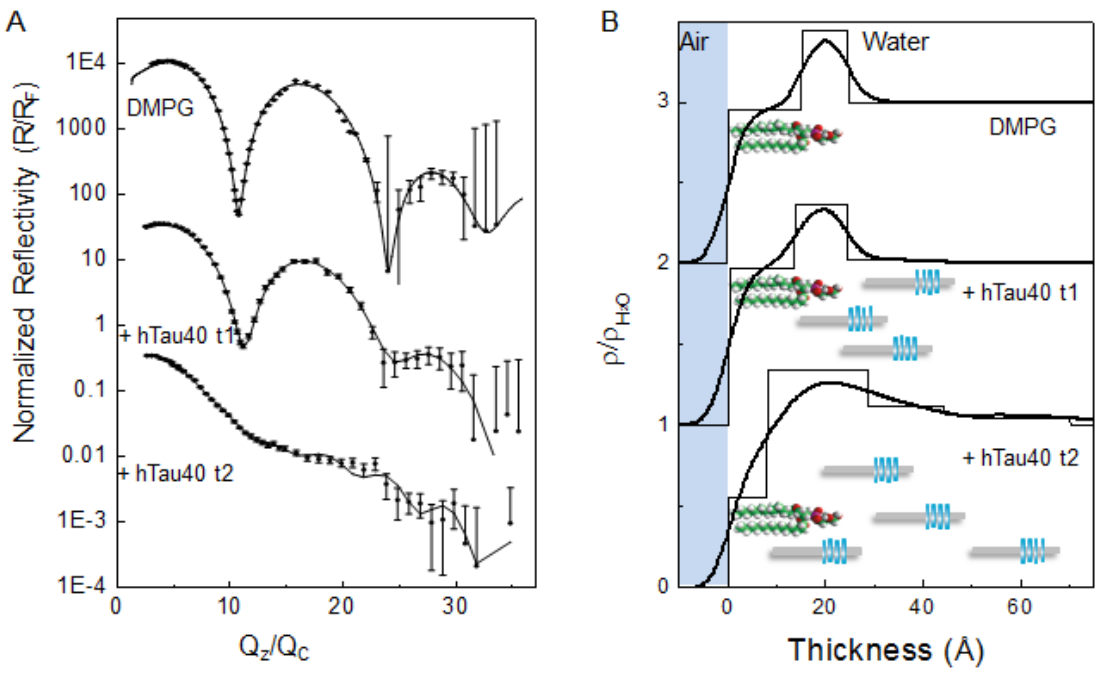


Figure 3.6 (A) Fresnel normalized X-ray reflectivity (R/RF) and (B) water normalized electron density (ρ/ρH2O) curves of DMPG monolayer with hTau40.

As seen in Figure 3.6, (A) Fresnel normalized X-ray reflectivity ($R/R_F$) and (B) water normalized electron density ($\rho/\rho_{H2O}$) curves of DMPG monolayer before and at two time points (t1=4 hours and t2=7 hours) after injection of hTau40 protein into subphase are illustrated. Figure 3.6 (A) Model dependent fits (lines) to $R/R_F$ data (filled symbols) are from Stochfit. (B) $\rho/\rho_{H2O}$ profiles from model dependent (curved lines) and box model fits (straight line profiles). Data for both reflectivity and electron density has been offset for clarity. The reflectivity value for bare DMPG is offset by 1000 and t1 is offset by 10. The electron density for DMPG is offset by 2 and for t1 by 1. Schematics depicting location of tau protein and lipids are also shown. Thickness value 0 corresponds to the air/lipid tail interface.

Table 3.2 X-ray Reflectivity Box Fit Parameters for hTau40 Insertion

| **Sample** | **Box Composition** | **Thickness (Å)** | **ρ / $\rho_{H20}$** | **Roughness (Å)** |
|---|---|---|---|---|
| **DMPG** | Lipid Tails | 15.30 ± 8.4 E-2 | 0.95 ± 3.7 E-2 | 3.22 ± 3.0 E-2 |
| | Lipid Heads | 9.31 ± 1.5 E-1 | 1.45 ± 5.0 E-3 | 3.22 ± 3.0 E-2 |
| **DMPG + hTau40 t1= 4 hours** | Lipid Tails | 13.45 ± 2.8 E-2 | 0.97 ± 4.7 E-3 | 4.19 ± 5.61 E-3 |
| | Lipid Tails + Heads + hTau40 | 10.67 ± 8.0 E-1 | 1.36 ± 6.5 E-4 | 2.13 ± 5.61 E-3 |
| | Lipid Heads + hTau40 | 11.53 ± 1.6 E-2 | 1.03 ± 1.7 E-3 | 3.14 ± 5.61 E-3 |
| | hTau40 | 10.67 ± 1.4 E-2 | 1.01 ± 1.8 E-3 | 2.10 ± 5.6 E-3 |
| **DMPG + hTau40 t2 = 7 hours** | Lipid Tails | 7.82 ± 2.2 E-1 | 0.55 ± 3.4 E-2 | 3.09 ± 3.2 E-2 |
| | Lipid Tails + Heads + hTau40 | 20.84 ± 2.6 E-1 | 1.34± 6.5 E-2 | 5.15 ± 5.6 E-3 |
| | hTau40 | 15.63 ± 3.4 E-1 | 1.11 ± 1.9 E-1 | 6.77 ± 9.7 E-3 |
| | hTau40 | 25.53 ± 1.2 E-2 | 1.05 ± 3.8 E-1 | 3.03 ± 1.0 E-1 |

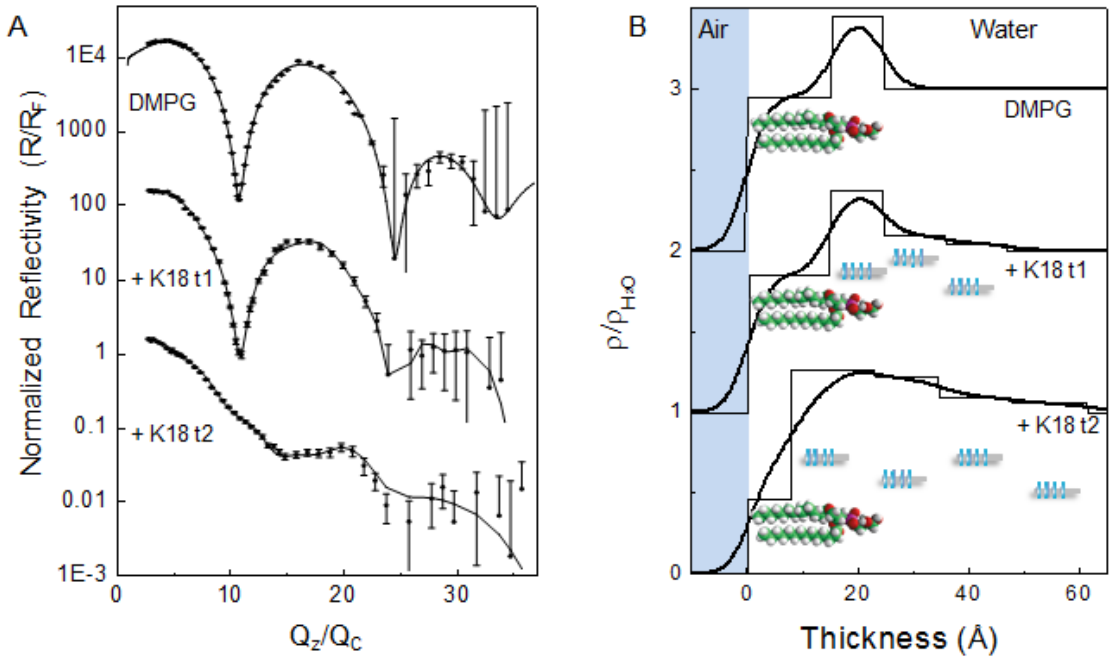


Figure 3.7 Fresnel normalized X-ray reflectivity and water normalized electron density curves of DMPG monolayer with K18.

Figure 3.7 illustrates (A) Fresnel normalized X-ray reflectivity ($R/R_F$) and (B) water normalized electron density ($\rho/\rho_{H2O}$) curves of DMPG monolayer before and at two time points (t1=4 hours and t2=7 hours) after injection of K18 protein into subphase. (A) Model dependent fits (lines) to $R/R_F$ data (filled symbols) from Stochfit. (B) $\rho/\rho_{H2O}$ profiles from model dependent (curved lines) and box model fits (straight line profiles). Data for both reflectivity and electron density has been offset for clarity. The reflectivity value for bare DMPG is offset by 10000 and t1 is offset by 100. The electron density for DMPG is offset by 2 and for t1 it is offset by 1. Schematics depicting location of tau protein and lipids are also shown. Thickness value 0 corresponds to the air/lipid tail interface.

Table 3.3 X-ray Reflectivity Box Fit Parameters for K18 Insertion

| **Sample** | **Box Composition** | **Thickness (Å)** | **ρ / $\rho_{H20}$** | **Roughness (Å)** |
|---|---|---|---|---|
| **DMPG** | Lipid Tails | 15.30 ± 8.4 E-2 | 0.95 ± 3.1 E-2 | 3.22 ± 3.0 E-2 |
| | Lipid Heads | 9.31 ± 1.5 E-1 | 1.45 ± 5.0 E-3 | 3.22 ± 3.0 E-2 |
| **DMPG + K18 t1= 4 hours** | Lipid Tails | 14.52 ± 4.7 E-2 | 0.85 ± 1.2 E-2 | 3.75 ± 1.4 E-2 |
| | Lipid Tails + Heads + K18 | 9.83 ± 1.443 E-1 | 1.36 ± 1.3 E-3 | 3.75 ± 1.4 E-2 |
| | Lipid Heads + K18 | 11.11 ± 3.3 E-3 | 1.09± 3.6 E-3 | 3.75 ± 1.4 E-2 |
| | K18 | 10.89 ± 3.6 E-3 | 1.04 ± 3.7 E-3 | 3.75 ± 1.4 E-2 |
| **DMPG + K18 t2= 7 hours** | Lipid Tails | 7.77 ± 4.6 E-2 | 0.46 ± 2.5 E-2 | 2.86 ± 2.1 E-2 |
| | Lipid Tails + Heads +K18 | 15.06 ± 1.8 E-1 | 1.26 ± 3.7 E-3 | 6.11 ± 5.4 E-2 |
| | Lipid Heads + K18 | 11.66 ± 1.1 E-1 | 1.21 ± 1.6 E-3 | 2.25 ± 2.4 E-2 |
| | K18 | 12.88 ± 1.5 E-1 | 1.09 ± 3.6 E-3 | 4.89 ± 6.1 E-2 |
| | K18 | 13.61 ± 1.9 E-1 | 1.05 ± 2.2 E-3 | 3.55 ± 3.1 E-2 |

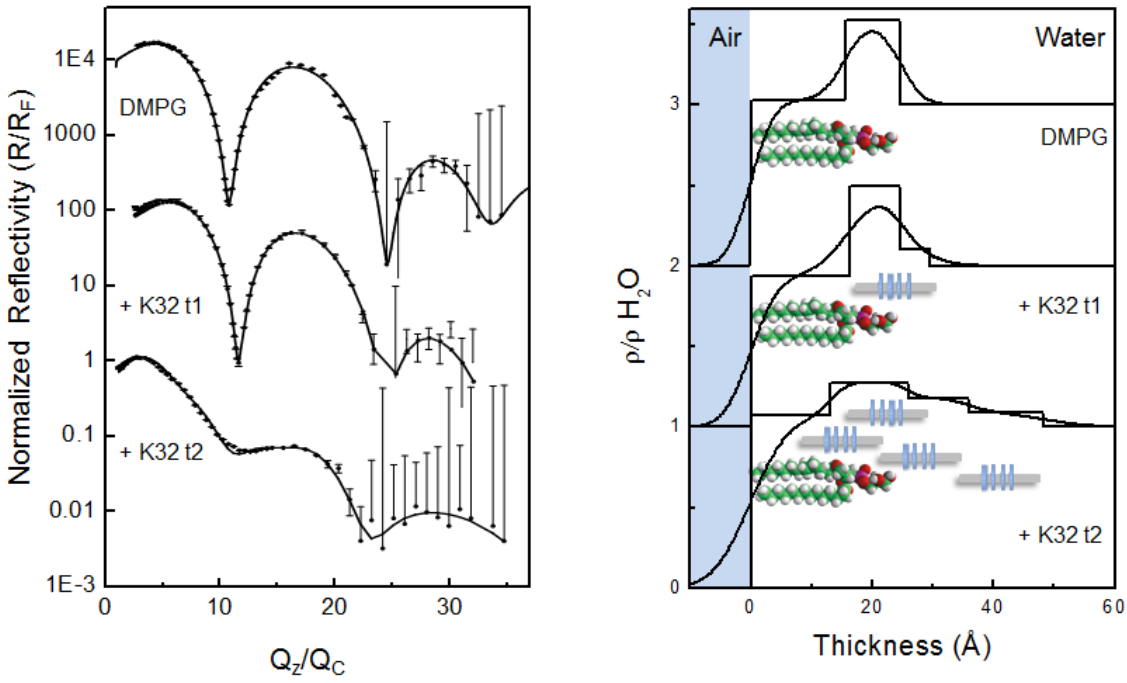


Figure 3.8 Fresnel normalized X-ray reflectivity and water normalized electron density curves of DMPG monolayer with K32.

Figure 3.8 illustrates (A) Fresnel normalized X-ray reflectivity ($R/R_F$) and (B) water normalized electron density ($\rho/\rho_{H2O}$) curves of DMPG monolayer before and at two time points (t1=4 hours and t2=7 hours) after injection of K32 protein into subphase. (A) Model dependent fits (lines) to $R/R_F$ data (filled symbols) from Stochfit. (B) $\rho/\rho_{H2O}$ profiles from model dependent (curved lines) and box model fits (straight line profiles). Data for both reflectivity and electron density has been offset for clarity. The reflectivity value for bare DMPG is offset by 10000 and t1 is offset by 100. The electron density for DMPG is offset by 2 and for t1 it is offset by 1. Schematics depicting location of tau protein and lipids are also shown. Thickness value 0 corresponds to the air/lipid tail interface.

Table 3.4 X-ray Reflectivity Box Fit Parameters for K32 Insertion

| **Sample** | **Box Composition** | **Thickness (Å)** | **ρ / $\rho_{H20}$** | **Roughness (Å)** |
|---|---|---|---|---|
| **DMPG** | Lipid Tails | 15.30 ±8.4 E-2 | 0.95 ± 3.7 E-2 | 3.22 ± 3.0 E-2 |
| | Lipid Heads | 9.31 ± 1.5 E-1 | 1.45 ± 5.0 E-3 | 3.22 ± 3.0 E-2 |
| **DMPG + K32 t1= 4 hours** | Lipid Tails | 16.36 ± 8.9 E-2 | 0.94 ± 2.4 E-2 | 3.96 ± 3.2 E-3 |
| | Lipid Heads + K32 | 8.28 ± 8.2 E-2 | 1.5 ± 2.8 E-2 | 3.56 ± 6.7 E-3 |
| | K32 | 4.77 ± 2.4 E-1 | 1.11 ± 1.1 E-1 | 4.01 ± 3.7 E-2 |
| **DMPG + K32 t2 = 7 hours** | Lipid Tails + K32 | 13.11 ± 1.1 E-1 | 1.07 ± 3.3 E-2 | 4.94 ± 3.1 E-2 |
| | Lipid Tails + Heads + K32 | 12.76 ± 4.8 E-1 | 1.28 ± 4.6 E-3 | 2.31± 3.1 E-2 |
| | K32 | 10.12 ± 1.8 E-1 | 1.18 ± 2.9 E-3 | 2.13± 3.1 E-2 |
| | K32 | 12.27 ± 3.6 E-1 | 1.09 ± 1.2 E-2 | 3.09± 3.1 E-2 |

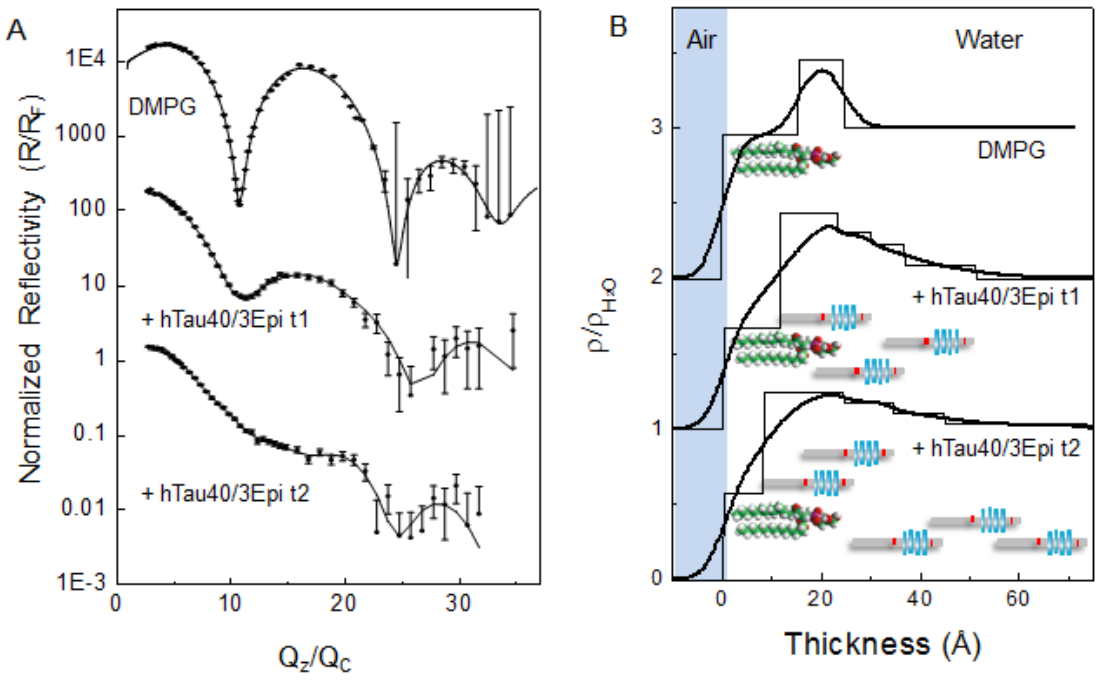


Figure 3.9 Fresnel normalized X-ray reflectivity and water normalized electron density curves of DMPG monolayer with hTau40/3Epi.

Figure 3.9 illustrates (A) Fresnel normalized X-ray reflectivity ($R/R_F$) and (B) water normalized electron density ($\rho/\rho_{H2O}$) curves of DMPG monolayer before and at two time points (t1=4 hours and t2=7 hours) after injection of hTau40/3Epi protein into subphase. (A) Model dependent fits (lines) to $R/R_F$ data (filled symbols) from Stochfit. (B) $\rho/\rho_{H2O}$ profiles from model dependent (curved lines) and box model fits (straight line profiles). Data for both reflectivity and electron density has been offset for clarity. The reflectivity value for bare DMPG is offset by 10000 and t1 is offset by 100. The electron density for DMPG is offset by 2 and for t1 it is offset by 1. Schematics depicting location of tau protein and lipids are also shown. Thickness value 0 corresponds to the air/lipid tail interface.

Table 3.5 X-ray Reflectivity Box Fit Parameters for hTau40/3Epi Insertion

| **Sample** | **Box Composition** | **Thickness (Å)** | **$\rho / \rho_{H20}$** | **Roughness (Å)** |
|---|---|---|---|---|
| **DMPG** | Lipid Tails | 15.30 ± 8.4 E-2 | 0.95 ± 3.7 E-2 | 3.22 ± 3.04 E-2 |
| | Lipid Heads | 9.31 ± 1.5 E-1 | 1.45 ± 5.0 E-3 | 3.22 ± 3.04 E-2 |
| **DMPG + hTau40/3Epi t1= 4 hours** | Lipid Tails | 11.35 ± 1.071 E-1 | 0.66 ± 3.271 E-2 | 3.15 ± 3.8 E-2 |
| | Lipid Tails + Heads + hTau40/3Epi | 11.57 ± 6.9 E-1 | 1.43 ± 4.3 E-3 | 7.55 ± 3.2 E-2 |
| | Lipid Heads + hTau40/3Epi | 6.90 ± 1.2 E-2 | 1.30 ± 4.8 E-3 | 1.47 ± 2.8 E-2 |
| | hTau40/3Epi | 6.68 ± 2.4 E-2 | 1.23 ± 2.4 E-2 | 3.69 ± 3.8 E-2 |
| | hTau40/3Epi | 14.25 ± 2.6 E-2 | 1.08 ± 2.6 E-2 | 7.44 ± 3.2 E-2 |
| **DMPG + hTau40/3Epi t2 = 7 hours** | Lipid Tails | 8.02 ± 1.1 E-1 | 0.57 ± 1.9 E-2 | 3.35 ± 1.3 E-2 |
| | Lipid Tails + Heads + hTau40/3Epi | 16.31 ± 1.7 E-1 | 1.23 ± 3.1 E-2 | 6.53 ± 7.8 E-4 |
| | Lipid Heads + hTau40/3Epi | 9.89 ± 6.9 E-1 | 1.18 ± 5.9 E-2 | 1.78 ± 1.9 E-2 |
| | hTau40/3Epi | 10.42 ± 2.4 E-1 | 1.10 ± 1.3 E-1 | 2.52 ± 2.7 E-2 |
| | hTau40/3Epi | 28.61 ± 1.0 E-1 | 1.03 ± 1.1 E-1 | 7.28 ± 5.1 E-2 |

Analysis of the XR data using the StochFit program (Danauskas et al., 2008) yielded $\rho/\rho_{H2O}$ distributions perpendicular to the protein/lipid film (Figure 3.6B, 3.7B, 3.8B, 3.9B). Box model fitting parameters are summarized in Tables 3.2-3.5. A two box model fit of the DMPG lipids alone shows a region of high density corresponding to lipid headgroups and a region of lower density corresponding to lipid acyl tails (see top schematics in Figure 3.6B, 3.7B, 3.8B, 3.9B). With the insertion of protein, three or more boxes were required to provide good fits to the two XR data sets, t1 and t2. The box at the air interface corresponds to DMPG tail groups alone and this box decreased in thickness with protein insertion. The box corresponding to the headgroup region of DMPG increased in thickness and slightly decreased in $\rho/\rho_{H2O}$ with tau protein insertion.

These physical changes to the DMPG film taken together indicate the presence of protein both in the headgroup and tail regions of the lipid monolayer as well as a diffuse layer of protein underneath the headgroups (see middle and bottom schematics in Figure 3.6B, 3.7B, 3.8B). The middle layers thus encompass a portion of lipid tails, lipid headgroups, and protein, all of which contribute to the overall $\rho/\rho_{H2O}$ fitted for this layer. Lipid tails, which have significantly lower electron density, most likely caused the decreases in the electron density of this middle layer as more of the tail region became incorporated into this layer.

Thus, XR measurements revealed that all four tau proteins inserted into the DMPG monolayer were located (1) underneath the lipid headgroups, (2) in the charged headgroup region, and (3) partially in the hydrophobic tail region. With time, all tau proteins penetrated further into the hydrophobic tail region. The three modes of interaction gave

rise to a protein layer at the membrane surface with the portion of the protein that had intercalated into the lipid membrane exhibiting a density of ~1.3.

GIXD data of K18 and hTau40/3Epi associated with a DMPG monolayer held at constant area showed that the insertion of the tau proteins disrupted the ordered packing of lipid tails (Figure 3.10), in agreement with observed disruption to monolayer morphology observed by FM (Figure 3.5). The DMPG monolayer at 25 mN/m showed a single Bragg peak, consistent with the LC domains observed from FM. After injection of K18 and incubation for ~13 hours, no diffraction peaks were observed in the monolayer (Figure 3.10A), indicating that the ordered lipid phase had been disrupted by the insertion of tau protein. After injection of hTau40/3Epi and incubation for ~13 hours, the Bragg peak associated with the DMPG monolayer had significantly decreased in intensity, indicating partial disruption of the ordered lipid phase. Moreover, K18 or hTau40/3Epi adsorbed to the bare air/water interface did not give rise to any scattering peaks (data not shown), indicating that they did not fold and assemble into in-plane crystalline structures detectable by GIXD.

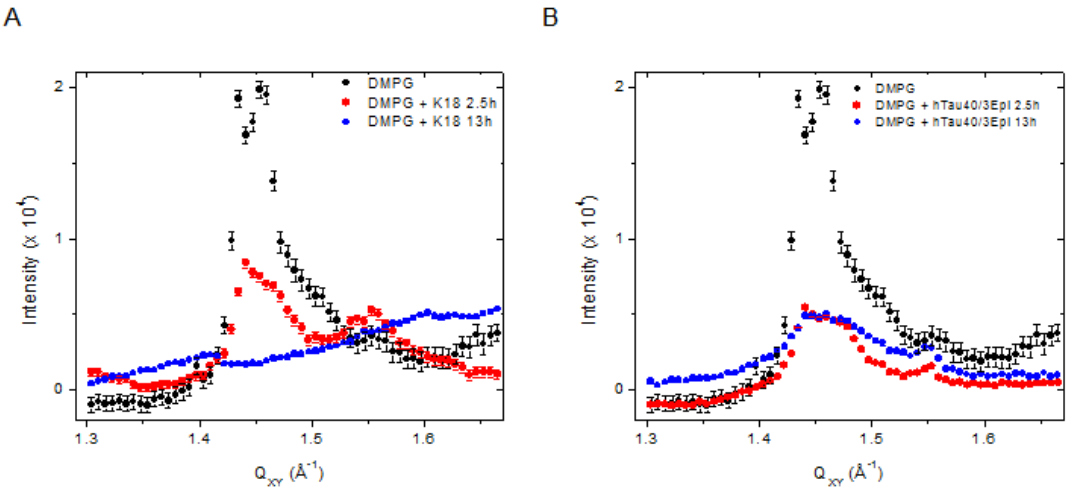


Figure 3.10 GID of DMPG overlaid with DMPG + K18 (A) or DMPG + mutant hTau40/3Epi (B) after 2.5 hours and 13 hours.

During the insertion experiments GIXD measurements were also taken before injection of protein, after two and half hours of incubation with the protein (t1) and at twelve hours after incubation (t2). The diffraction patterns obtained for the DMPG monolayer at 25 mN/m and 25 °C before and after protein injection are shown in Figure 3.11, 3.12, 3.13, and 3.14.

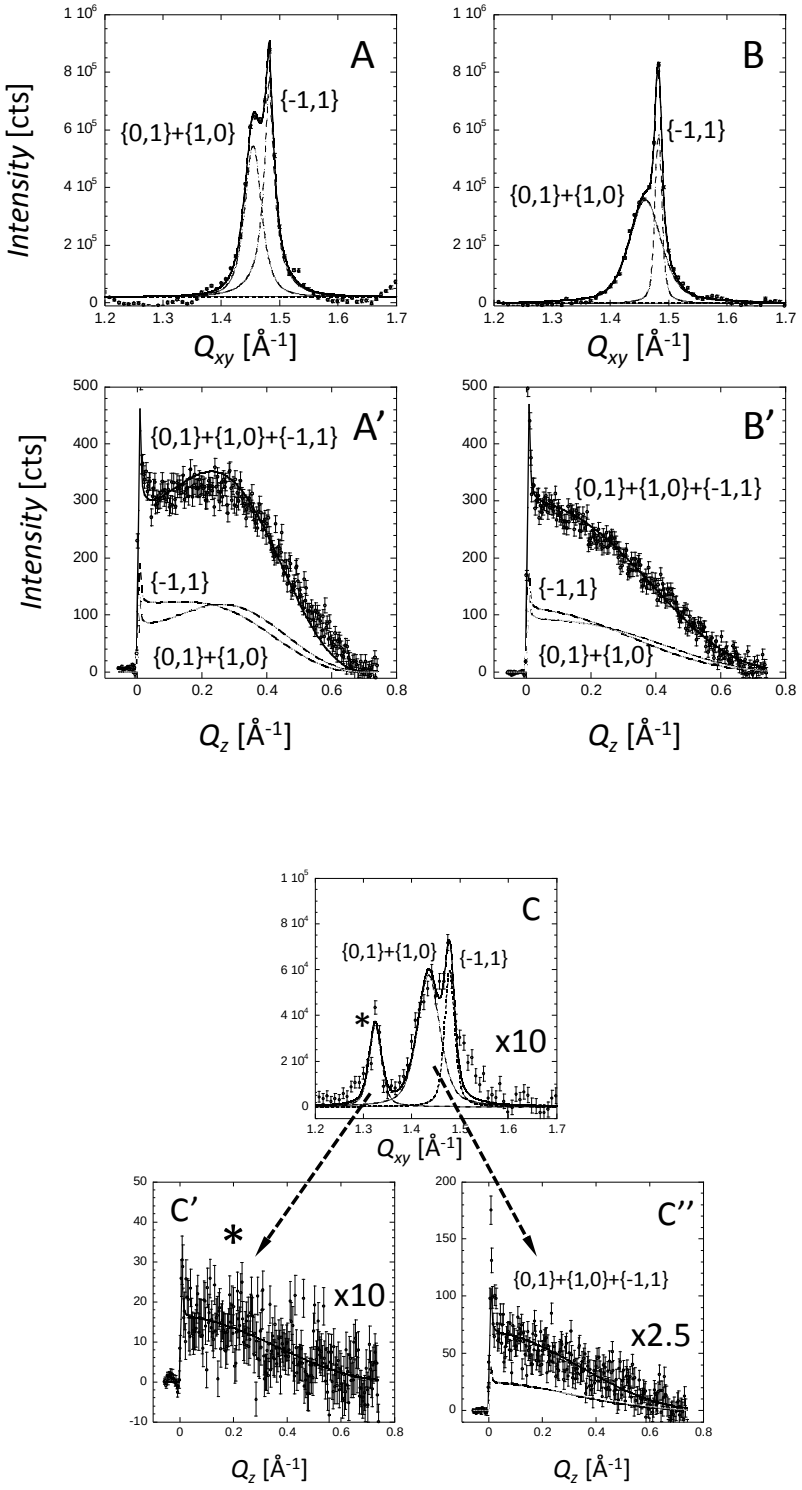


Figure 3.11 Bragg peaks (top) and rods (bottom) of pure DMPG monolayer and hTau40.

Figure 3.11 illustrates *Bragg peaks* (top row) and *rods* (bottom row) of pure DMPG monolayer (A, A') at the air water interface at the surface pressure of 25 mN/m and the temperature of 25°C and with hTau40 after *t*1=2.5 hours (B, B') and *t*2=12 hours (C, C', C'') of incubation, respectively. Due to the measurements at the constant area of the trough the protein injection caused the surface pressure increase for the consecutive time periods: at *t*1, 34 and at *t*2, 39 mN/m, respectively. The *Bragg peaks* were fitted using the sum of two Voigt profiles (solid line) and de-convoluted into separate peaks (dashed lines) corresponding to each of *{1,0}+{0,1}* and *{1,-1}* Bragg peaks. *Bragg peaks* were obtained by integrating over the (-0.05 Å-1 $\leq Q_z \leq$ 0.75 Å$^{-1}$). A', B' and C'' show the sum of the two *{1,0}+{0,1}* and *{1,-1} Bragg rods* corresponding to DMPG, *t1* and *t2* after injection of hTau40. The *Bragg rods* were obtained by integrating over the (1.35 Å$^{-1} \leq Q_{xy} \leq$ 1.55 Å$^{-1}$) region and fitted (solid line) by approximating the coherently scattering part of the alkyl tail by a cylinder of constant electron density. Each of the separate Bragg rods are shown as dashed lines in the bottom row. The *{0,1}* and *{1,0} Bragg rods* are superimposable. The *Bragg peak* and *rod* associated with the hTau40 protein are indicated by *. The *Bragg rod* (C') was obtained by integrating over the (1.25 Å$^{-1} \leq Q_{xy} \leq$ 1.35 Å$^{-1}$) region.

Table 3.6 Structural Parameters from GIXD of hTau40 Insertion into DMPG Monolayer

| 25°C | | DMPG (25 mN/m) | DMPG: hTau40 t1=2.5hrs (34 mN/m) | DMPG: hTau40 t=12hrs (39 mN/m) |
|---|---|---|---|---|
| **Distorted Hexagonal Unit Cell** | **a (Å)** | 4.93 ± 0.01 | 4.92 ± 0.01 | 4.96 ± 0.01 |
| | **b (Å)** | 4.93 ± 0.01 | 4.92 ± 0.01 | 4.96 ± 0.01 |
| | **γ (degrees)** | 118.8 ± 0.4 | 119.0 ± 0.4 | 118.0 ± 0.4 |
| **Area per molecule ($Å^2$)** | | 42.6 ± 0.1 | 42.4 ± 0.2 | 43.4 ± 0.1 |
| **Integrated Intensity (%)** | | 100 | 90 | 13 |
| **Coherence Length, $L_c$ (Å)** | | 14.0 ± 0.5 | 11.5 ± 0.5 | 11.7 ± 0.5 |
| **tilt angle, t (°)** | | 18.1 ± 1.0 | 15.5 ± 1.0 | 16.7 ± 1.0 |
| **Tilt dir. from NN, non-symmetry (°)** | | 0 | 0 | 0 |
| **σ (Å)** | | 0.5 ± 0.2 | 0.6 ± 0.2 | 0.6 ± 0.2 |

Extracted from the GIXD measurements structural parameters of the DMPG before and after injection of the hTau40 protein measured at constant trough area at t1=2.5 and t2=12 hours, respectively. The GIXD measurements are shown in Figure 3.11. Due to the constant area of the trough the protein injection caused the surface pressure increase for the consecutive time periods. $L_c$ is the length of the coherently scattering part of the alkyl tail measured along its backbone. Tilt angle is measured from the surface normal. The tilt angle is measured between direction of nearest neighbor and the projection of the alkyl tail on the subphase surface. Nearest neighbor (NN) is along a + b, where a and b are the 2D unit cell vectors. Debye-Waller factor is the root mean-square molecular displacement.

Table 3.7 In-Plane Bragg Peaks Coherence Length for hTau40 Insertion into DMPG

| **25ºC** | **In-Plane Bragg Peaks Coherence Length, $L_{xy}$ (Å) ± 10 Å** | |
|---|---|---|
| | **$L_{10+01}$** | **$L_{1-1}$** |
| **DMPG** | 170 | 310 |
| **DMPG+hTau40, t1=2.5hrs** | 90 | 500 |
| **DMPG+hTau40, t2=12hrs** | 100 | 240 |

Length, $L_{xy}$, is the in-plane coherence length; an average size of the 2D "crystalline" islands.

Table 3.8 Structural Parameters Extracted from hTau40 Protein Peak at $Q_{xy}$=1.325Å$^{-1}$

| **25ºC** | ***d*-spacing (Å)** | **Inte-grated Intensity (%)** | **Coherence Length, $L_c$ (Å)** | **tilt angle, t (°)** | **σ (Å)** | **In-Plane Bragg Peaks Co-herence Length, $L_{xy}$ (Å) ± 10 Å** |
|---|---|---|---|---|---|---|
| **hTau40 t1=2.5hrs (34 mN/m)** | - | - | - | - | - | - |
| **hTau40 t=12hrs (39 mN/m)** | 4.74 ± .02 | 100 | 7.2 ± 1 | 0 | 0.83± 0.2 | 200 |

$L_c$ is the length of the coherently scattering part of the protein.

Length, $L_{xy}$, is the in-plane coherence length; an average length over which the scattering units are in registry.

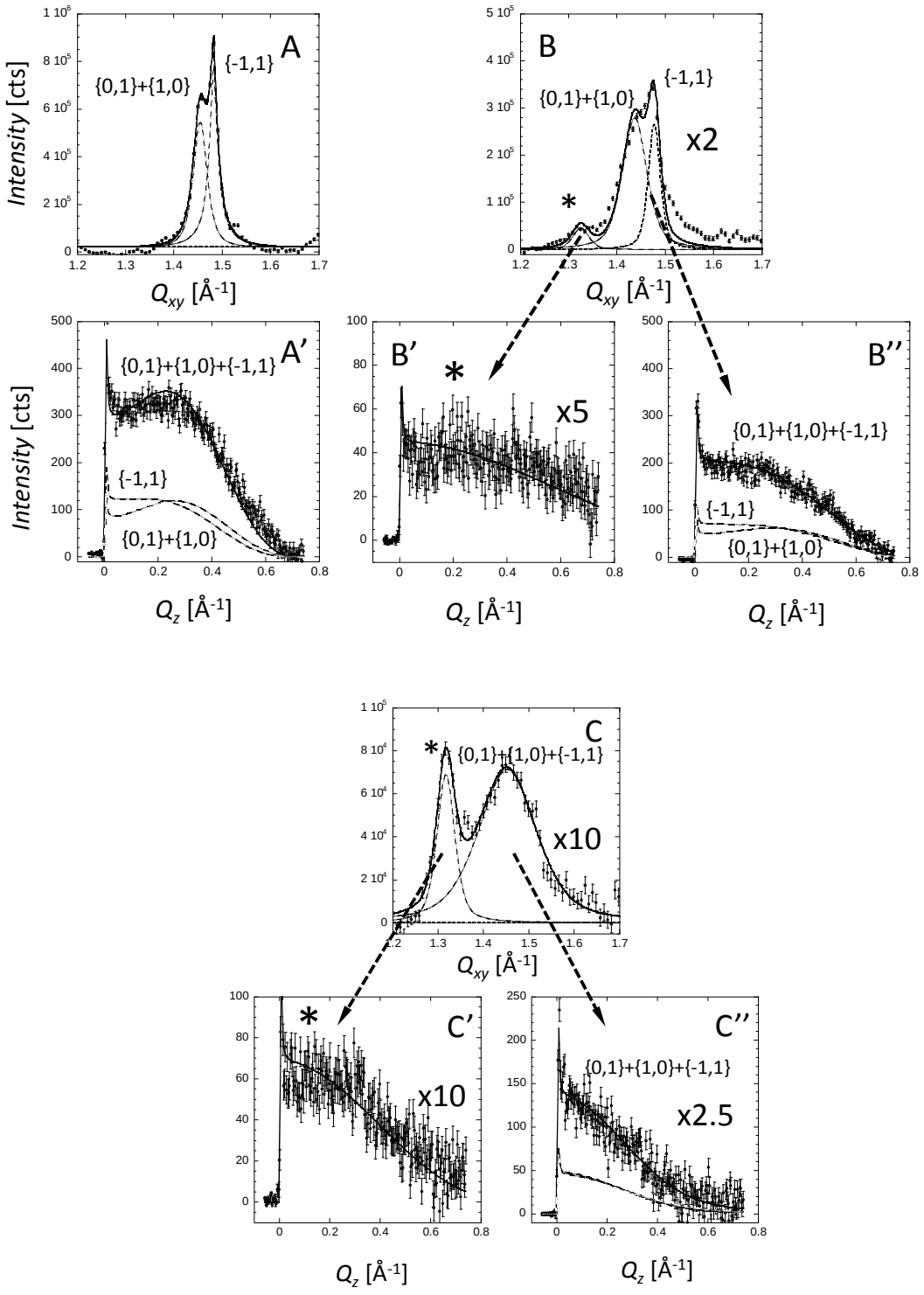


Figure 3.12 Braggs peaks (top) and rods (bottom) of pure DMPG monolayer with K18.

Figure 3.12 illustrates *Bragg peaks* (top row) and *rods* (bottom row) of pure DMPG monolayer (A, A') at the air water interface at the surface pressure of 25 mN/m and the temperature of 25°C and with K18 after *t*1=2.5 hours (B, B', B'') and *t*2=12 hours (C, C', C'') of incubation, respectively. Due to the measurements at the constant area of the trough the protein injection caused the surface pressure increase for the consecutive time periods: at *t*1, 45 and at *t*2, 45 mN/m, respectively. The *Bragg peaks* were fitted using the sum of two Voigt profiles (solid line) and de-convoluted into separate peaks (dashed lines) corresponding to each of *{1,0}+{0,1}* and *{1,-1}* Bragg peaks. *Bragg peaks* were obtained by integrating over the (0.05 Å-1 $\leq Q_z \leq$ 0.75 Å$^{-1}$). (A', B'', and C'') show the sum of the two *{1,0}+{0,1}* and *{1,-1} Bragg rods* corresponding to DMPG, *t1* and *t2* after injection of K18. The *Bragg rods* were obtained by integrating over the (1.35 Å$^{-1}$ $\leq Q_{xy} \leq$ 1.55 Å$^{-1}$) region and fitted (solid line) by approximating the coherently scattering part of the alkyl tail by a cylinder of constant electron density. Each of the separate *{0,1}, {1,0}* and *{-1,1} Bragg rods* are shown as dashed lines in bottom row. The *{0,1}* and *{1,0} Bragg rods* are superimposable. The *Bragg peaks* and *rods* associated with the K18 protein is indicated by *. The protein peak *Bragg rods* (B', C') were obtained by integrating over the (1.25 Å$^{-1}$ $\leq Q_{xy} \leq$ 1.35 Å$^{-1}$) region.

Table 3.9 Structural Parameters from GIXD of K18 Insertion into DMPG Monolayer

| 25°C | | DMPG (25 mN/m) | DMPG: K18 t1=2.5hrs (45 mN/m) | DMPG: K18 t=12hrs (45 mN/m) |
|---|---|---|---|---|
| **Distorted Hexagonal Unit Cell** | **a (Å)** | 4.93 ± 0.01 | 4.96 ± 0.01 | 5.00 ± 0.01 |
| | **b (Å)** | 4.93 ± 0.01 | 4.96 ± 0.01 | 5.00 ± 0.01 |
| | **γ (degrees)** | 118.8 ± 0.4 | 118.1 ± 0.4 | 120 |
| **Area per molecule ($Å^2$)** | | 42.6 ± 0.1 | 43.4 ± 0.2 | 43.2 ± 0.2 |
| **Integrated Intensity (%)** | | 100 | 70 | 30 |
| **Coherence Length, $L_c$ (Å)** | | 14.0 ± 0.5 | 11.6 ± 0.5 | 10.5 ± 0.5 |
| **tilt angle, t (°)** | | 18.1 ± 1.0 | 19.5 ± 1.0 | 13.6 ± 1.0 |
| **tilt dir. from NN, non-symmetry (°)** | | 0 | 0 | 0 |
| **σ (Å)** | | .5 ± 0.2 | .5 ± 0.2 | 0.6 ± 0.2 |

Extracted from the GIXD measurements structural parameters of the DMPG before and after injection of the K18 protein measured at constant trough area at $t1$=2.5 and $t2$=12 hours, respectively. The GIXD measurements are shown in Figure 3.12. Due to the constant area of the trough the protein injection caused the surface pressure increase for the consecutive time periods. $L_c$ is the length of the coherently scattering part of the alkyl tail measured along its backbone. Tilt angle is measured from the surface normal. The tilt angle is measured between direction of nearest neighbor and the projection of the alkyl tail on the subphase surface. Nearest neighbor (NN) is along $a + b$**,** where $a$ and $b$ are the 2D unit cell vectors**.** $\sigma$ is the Debye-Waller factor or root mean-square molecular displacement.

Table 3.10 In-Plane Bragg Peaks Coherence Length for K18 Insertion into DMPG

| **25°C** | **In-Plane Bragg Peaks Coherence Length, $L_{xy}$ (Å) ± 10 Å** | |
|---|---|---|
| | **$L_{10+01}$** | **$L_{1-1}$** |
| **DMPG** | 170 | 310 |
| **DMPG+K18, t1=2.5hrs** | 100 | 200 |
| **DMPG+K18, t2=12hrs** | 40 | 40 |

Length, $L_{xy}$, is the in-plane coherence length; an average size of the 2-D "crystalline" islands.

Table 3.11 Structural Parameters Extracted from K18 Protein Peak at Qxy=1.325Å$^{-1}$

| 25°C | *d*-spacing (Å) | Inte-grated Intensity (%) | Co-herence Length, $L_c$ (Å) | tilt angle t (°) | σ (Å) | In-Plane Bragg Peaks Co-herence Length, $L_{xy}$ (Å) |
|---|---|---|---|---|---|---|
| **K18 t1=2.5hrs (45 mN/m)** | 4.74 ± 0.03 | 56 | 4.5* | 0 | 0.6± 0.2 | 150 ± 20 Å |
| **K18 t=12hrs (45 mN/m)** | 4.77 ± 0.02 | 100 | 6.5± 1 | 0 | 0.7± 0.2 | 120 ± 10 Å |

Structural parameters extracted from the K18 protein peak at $Q_{xy}$=1.325Å$^{-1}$.

$L_c$ is the length of the coherently scattering part of the protein. Length, $L_{xy}$, is the in-plane coherence length; an average length over which the protein scattering units are in registry.

* Due to weak scattering and high background the extraction of the *Bragg rod* and resulting structural data was with high degree of uncertainty.

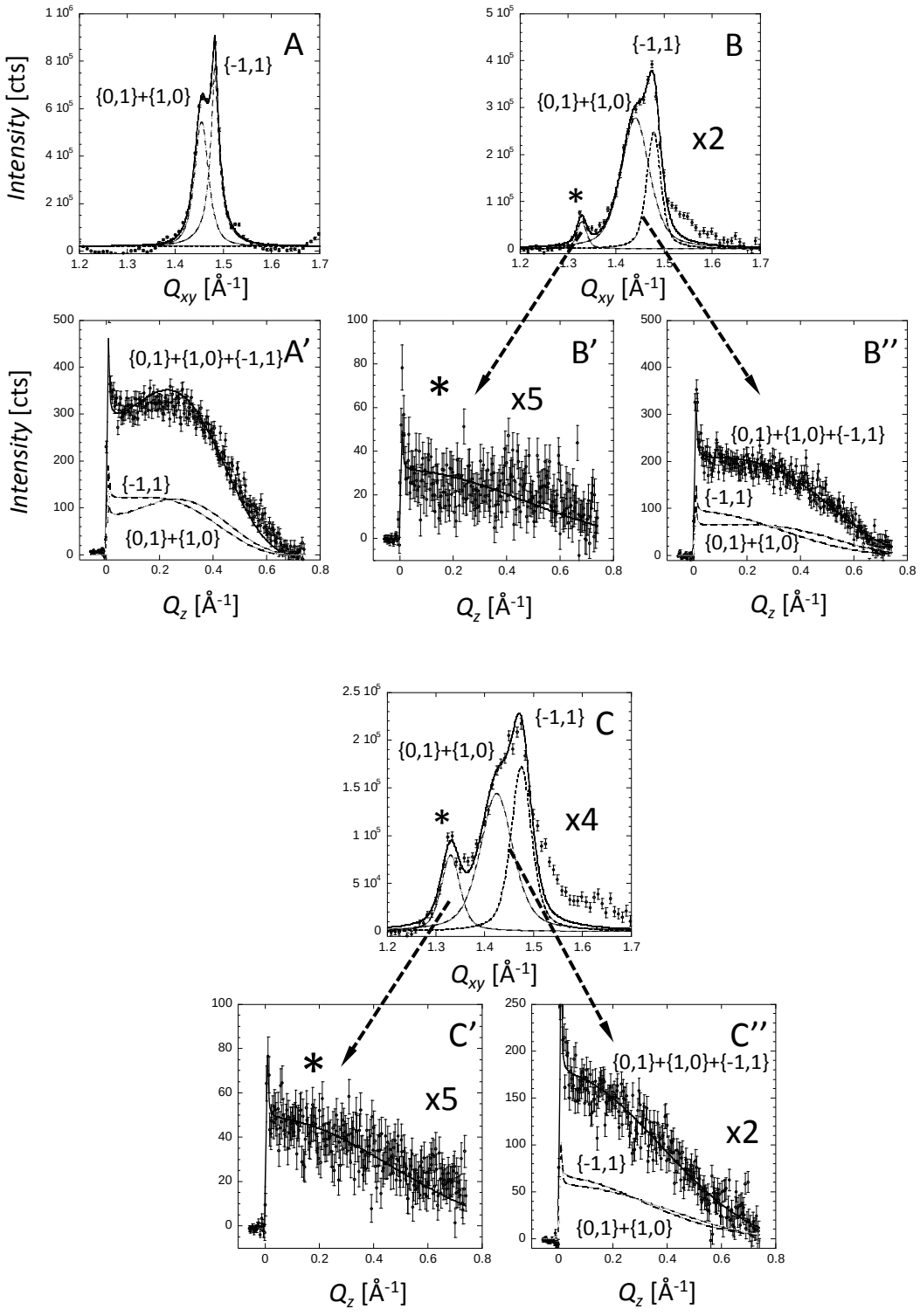


Figure 3.13 Bragg peaks (top) and rods (bottom) of pure DMPG monolayer with hTau40/3Epi.

Figure 3.13 illustrates *Bragg peaks* (top row) and *rods* (bottom row) of pure DMPG monolayer (A, A') at the air water interface at the surface pressure of 25 mN/m and the temperature of 25°C and with hTau40/3Epi after *t*1=2.5 hours (B, B', B'') and *t*2=12 hours (C, C', C'') of incubation, respectively. Due to the measurements at the constant area of the trough the protein injection caused the surface pressure increase for the consecutive time periods: at *t*1, 47 and at *t*2, 44 mN/m, respectively. The *Bragg peaks* were fitted using the sum of two Voigt profiles (solid line) and de-convoluted into separate peaks (dashed lines) corresponding to each of *{1,0}+{0,1}* and *{1,-1}* Bragg peaks. *Bragg peaks* were obtained by integrating over the (0.05 Å-1 $\leq Q_z \leq$ 0.75 Å$^{-1}$). (A', B'', and C'') show the sum of the two *{1,0}+{0,1}* and *{1,-1} Bragg rods* corresponding to DMPG, *t1* and *t2* after injection of hTau40/3Epi. The *Bragg rods* were obtained by integrating over the (1.35 Å$^{-1}$ $\leq Q_{xy} \leq$ 1.55 Å$^{-1}$) region and fitted (solid line) by approximating the coherently scattering part of the alkyl tail by a cylinder of constant electron density. Each of the separate *{0,1}, {1,0}* and *{-1,1} Bragg rods* are shown as dashed lines in bottom row. The *{0,1}* and *{1,0} Bragg rods* are superimposable. The *Bragg peaks* and *rods* associated with the hTau40/3Epi protein is indicated by *. The protein peak *Bragg rods* (B', C') were obtained by integrating over the (1.25 Å$^{-1}$ $\leq Q_{xy} \leq$ 1.35 Å$^{-1}$) region.

Table 3.12 Structural Parameters from GIXD of hTau40/3Epi Insertion into DMPG Monolayer

| **25°C** | | **DMPG (25 mN/m)** | **DMPG: hTau40/3Epi t1=2.5hrs (47 mN/m)** | **DMPG: hTau40/3Epi t=12hrs (44 mN/m)** |
|---|---|---|---|---|
| **Distorted Hexagonal Unit Cell** | **a (Å)** | 4.93 ± 0.01 | 4.95 ± 0.01 | 4.98 ± 0.01 |
| | **b (Å)** | 4.93 ± 0.01 | 4.95 ± 0.01 | 4.98 ± 0.01 |
| | **γ (degrees)** | 118.8 ± 0.4 | 118.2 ± 0.4 | 117.6 ± 0.4 |
| **Area per molecule ($Å^2$)** | | 42.6 ± 0.1 | 43.2 ± 0.1 | 43.9 ± 0.1 |
| **Integrated Intensity (%)** | | 100 | 80 | 58 |
| **Coherence Length, $L_c$ (Å)** | | 14.0 ± 0.5 | 10.9 ± 0.5 | 10.9 ± 0.5 |
| **tilt angle, t (°)** | | 18.1 ± 1.0 | 18.1 ± 1.0 | 19.2 ± 1.0 |
| **tilt dir. from NN, non-symmetry (°) Tilt dir. from NN, non-symmetry (°)** | | 0 | 0 | 0 |
| **σ (Å)** | | 0.5 ± 0.2 | 0.6 ± 0.2 | 0.6 ± 0.2 |

Extracted from the GIXD measurements structural parameters of the DMPG before and after injection of the hTau40/3Epi protein measured at constant trough area at $t1$=2.5 and $t2$=12 hours, respectively. The GIXD measurements are shown in Figure 3.13. Due to the constant area of the trough the protein injection caused the surface pressure increase for the consecutive time periods. $L_c$ is the length of the coherently scattering part of the alkyl tail measured along its backbone. Tilt angle is measured from the surface normal. The tilt angle is measured between direction of nearest neighbor and the projection of the alkyl tail on the subphase surface. Nearest neighbor (NN) is along $a + b$, where $a$ and $b$ are the 2D unit cell vectors**.** σ is the Debye-Waller factor or root mean-square molecular displacement.

Table 3.13 In-plane Bragg Peaks Coherence Length for hTau40/3Epi Insertion into DMPG

| 25ºC | **In-Plane Bragg Peaks Coherence Length, $L_{xy}$ (Å) ± 10 Å** | |
|---|---|---|
| | **$L_{10+01}$** | **$L_{1-1}$** |
| **DMPG** | 170 | 310 |
| **DMPG+hTau40/3Epi, t1=2.5hrs** | 80 | 170 |
| **DMPG+hTau40/3Epi, t2=12hrs** | 70 | 110 |

Length, $L_{xy}$, is the in-plane coherence length; an average size of the 2-D "crystalline" islands.

Table 3.14 Structural Parameters Extracted from hTau40/3Epi Protein Peak at $Q_{xy}$=1.325Å$^{-1}$

| 25ºC | *d*-spacing (Å) | Inte-grated Intensity (%) | Co-herence Length, $L_c$ (Å) | tilt angle, t (°) | σ (Å) | In-Plane Bragg Peaks Co-herence Length, $L_{xy}$ (Å) ± 10 Å |
|---|---|---|---|---|---|---|
| **hTau40/3Epi t1=2.5hrs (47 mN/m)** | 4.72 ± .02 | 37 | 5.5 ± 1 | 0 | 0.63± 0.2 | 110 |
| **hTau40/3Epi t=12hrs (44 mN/m)** | 4.72 ± .02 | 100 | 5.5 ± 1 | 0 | 0.67± 0.2 | 130 |

Structural parameters extracted from the hTau40/3Epi protein peak at $Q_{xy}$=1.33Å$^{-1}$.

$L_c$ is the length of the coherently scattering part of the protein. Length, $L_{xy}$, is the in-plane coherence length; an average length over which the scattering units are in registry.

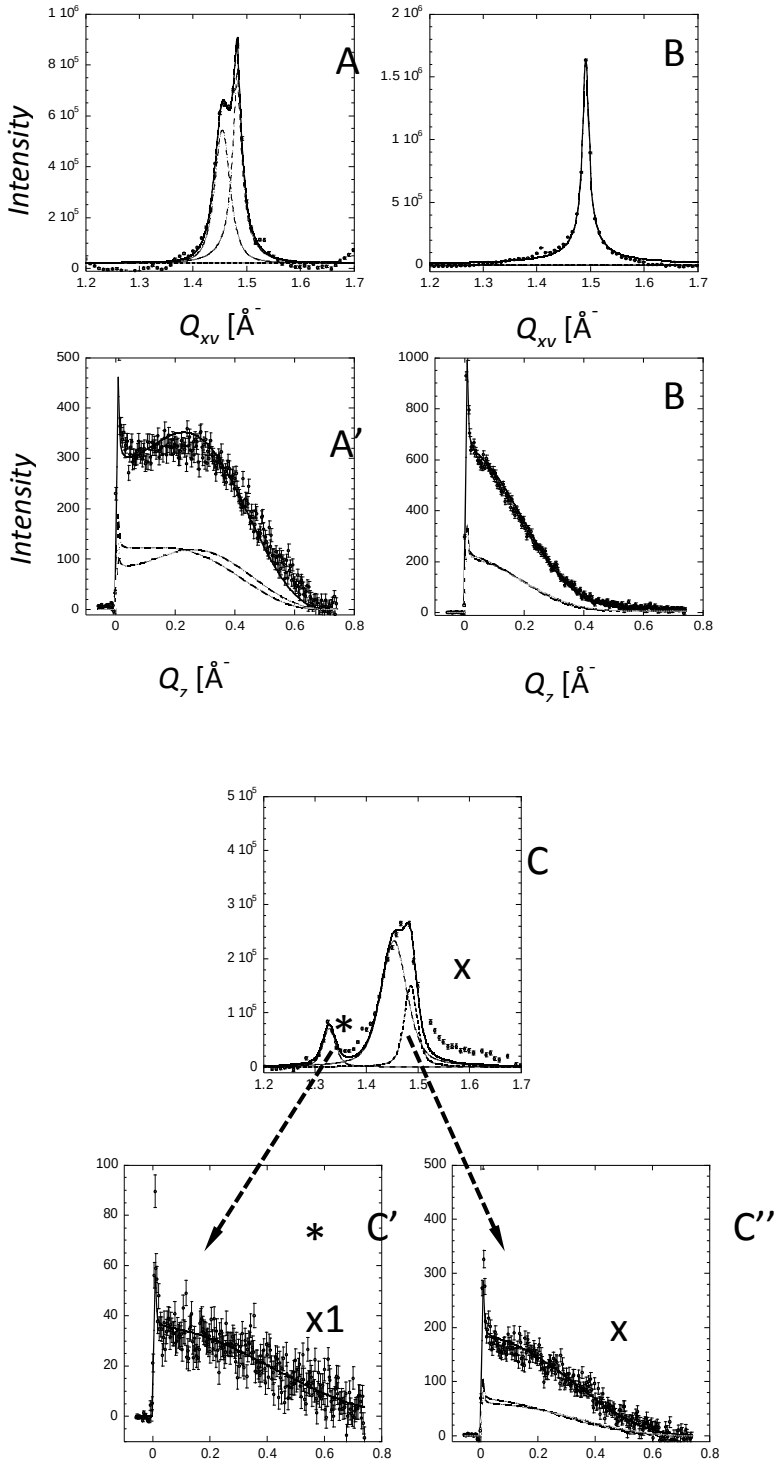


Figure 3.14 Bragg peaks (top) and rods (bottom) of pure DMPG monolayer with K32.

Figure 3.14 illustrates *Bragg peaks* (top row) and *rods* (bottom row) of pure DMPG monolayer (A, A') at the air/water interface at the surface pressure of 25 mN/m and the temperature of 25°C and with K32 protein after *t1*=2.5 hours (B, B') and *t*2=12 hours (C, C', C'') of incubation, respectively. Due to the measurements at the constant area of the trough the protein injection caused the surface pressure increase for the consecutive time periods: at *t1*, 40 and at *t2*, 48 mN/m, respectively. The *Bragg peaks* were fitted using the sum of two Voigt profiles (solid line) and de-convoluted into separate peaks (dashed lines) corresponding to each of *{1,0}+{0,1}* and *{1,-1}* Bragg peaks. *Bragg peaks* were obtained by integrating over the (0.05 Å-1 $\leq Q_z \leq$ 0.75 $Å^{-1}$). (A', B', and C'') show the sum of the two *{1,0}+{0,1}* and *{1,-1} Bragg rods* corresponding to DMPG, *t1* and *t2* after injection of K32. The *Bragg rods* were obtained by integrating over the (1.35 $Å^{-1} \leq Q_{xy} \leq$ 1.55 $Å^{-1}$) region and fitted (solid line) by approximating the coherently scattering part of the alkyl tail by a cylinder of constant electron density. Each of the separate *{0,1}, {1,0}* and *{-1,1} Bragg rods* are shown as dashed lines in bottom row. The *{0,1}* and *{1,0} Bragg rods* are superimposable. The *Bragg peaks* and *rods* associated with the K32 protein is indicated by *. The protein peak *Bragg rods* (C') were obtained by integrating over the (1.25 $Å^{-1} \leq Q_{xy} \leq$ 1.35 $Å^{-1}$) region.

For all four of the insertion experiments we obtained a strong initial signal for the Bragg peaks representing the DMPG monolayer (Figure 3.11A, 3.12A, 3.13A, and 3.14A). The DMPG monolayer at 25 mN/m showed two Bragg peaks, consistent with the LC domains observed from FM. For each of the systems measured, two Bragg peaks were

observed at $Q_{xy}$ ~ 1.45 Å$^{-1}$ and $Q_{xy}$ ~ 1.48 Å$^{-1}$. The presence of two Bragg peaks indicates a distorted hexagonal 2D unit cell. For each of the systems the ratio of the integrated intensities of the two Bragg peaks (-0.05 Å-1 ≤ $Q_z$ ≤ 0.75 Å$^{-1}$) were approximately 2:1, in agreement with the multiplicity rule. The two peaks can be indexed as *{1, 0}+{0, 1}* and *{1,-1}*. The observed two *d*-spacings (= $2\pi/Q_{xy}$): $d_{10+01}$, and $d_{1-1}$ give rise to a primitive 2D unit cell with dimensions and of the unit vectors |**a**| = |**b**| and the angle between them γ, as well as the area per two alkyl chains listed in the Tables. The diffraction patterns were fitted using the sum of two Voigt profiles (solid lines) and de-convoluted into separate peaks (dashed lines) corresponding to *{1,0}+{0,1}* and *{1,-1}* Bragg peaks. The structural parameters extracted from the analysis of the GIXD diffraction data are listed in the Tables. Assuming the monolayer consists of perfect 2D crystallites of finite average dimension $L_{xy}$ (the lateral *coherence length*) in the crystallographic direction {*h, k*} with no preferred azimuthal orientation, the Scherrer formula can be used to calculate the coherence length in the three crystallographic directions.

In principle, the diffraction from the DMPG monolayer after injection of the proteins is similar and shows the same final result of reduction of the amount of ordered monolayer phase at the interface. This is indicated by the decreased integrated intensities of the Bragg peaks, the increased area per lipid molecule, and reduction in the average coherence lengths $L_{xy}$ (the peaks becoming broader). The coherently scattering parts of the alkyl tails ($L_c$) are also becoming shorter and the Debye-Waller factors (σ) are increasing. The initial distorted hexagonal packing (|**a**| = |**b**|, γ<120°) is becoming hexatic-like, with little or no distinction between lipid tail packing along *{0,1}+{1,0}* and *{-1,1}* crystallographic directions.

In the cases of the hTau40, K18 and hTau40/3Epi insertions (Figure 3.11B, 3.12B, and 3.13B) we also saw a small peak emerging at 1.325 $Å^{-1}$. After twelve hours of incubation we observed both a greater decrease in the DMPG signal and an increased intensity at the location of the small peak of ~ 1.325 $Å^{-1}$for all proteins (Figure 3.11C, 3.12C, 3.13C, and 3.14C). Bragg rods which were derived from this data (Figure 3.11A', 3.12A', 3.13A', and 3.14A'; 3.11B", 3.12B", 3.13B", and 3.14B'; and 3.11C", 3.12C", 3.13C", and 3.14C") corresponded to the DMPG monolayer *{1,0}+{0,1}* and *{1,-1}* Bragg peaks and the Bragg rods in Figure 3.11B', 3.12B', and 3.13B'; and 3.11C', 3.12C' 3.13C', and 3.14C' corresponded to the small peak at around 1.4 $Å^{-1}$. The combined Bragg rod profiles of the *{0,1}+{1,0}* and *{1,-1}* reflections, were obtained by integrating the scattering data through the 1.35 $Å^{-1} \leq Q_{xy} \leq 1.55$ $Å^{-1}$ region of the two peaks. Analysis of the Bragg rod profiles were done by approximating the lipid alkyl tails as tilted cylinders with constant electron density and length $L_c$. See the tables for the numerical results of this analysis.

The *d*-spacings associated with these peaks are ~ 4.75 (± 0.03) Å and the length coherently scattering units obtained from the *Bragg rod* fits are from 4.5 to 7.2 Å. Due to small intensity of these 'protein peaks' and the proximity of the strong scattering peaks from the DMPG monolayer, extraction of the their *Bragg* rods was difficult. The in-plane coherence lengths calculated from the FWHMs of these peaks vary from 110 to 200 Å and correspond to 23 - 42 *d*-spacings. The integrated intensities of the peaks increased significantly with the incubation time indicating increased amount of material accumulating at the surface.

No diffraction signals were observed in the low $Q_{xy}$ region (0.05 - 1.2 $Å^{-1}$) corresponding with *d*-spacings of from 120 Å  5.5 Å (data not shown). Therefore we can conclude that no regular molecular arrays with such characteristic distances are formed or detectable by GIXD.

### 3.2.4 *Neutron reflectivity measurements of K18, htau40/3Epi and K32 associated with supported lipid bilayers*

To study the effect of the K18 tau protein construct on a charge neutral DPPC lipid bilayer, NR measurements have been performed using a custom made solid-liquid interface cell as previously described (Dubey, 2010.) Reflectivity and corresponding SLD profile are shown in Figure 3.15A. The simplest physically meaningful model was used to fit the data. The system was described using two slabs. The first slab accounts for a thin $D_2O$ layer between the quartz substrate and the lipid bilayer and the second for the alkyl tails of the bilayer. Fit parameters resulting in best $\chi^2$ values are included in Table 3.15. The lipid bilayer was fabricated by LB/LS transfer at 25 mN/m, which leads to a moderate densely packed bilayer with the lipids in LC phase. The water buffer layer between quartz and the bilayer has an initial thickness of 26 Å. The initial thickness of the alkyl tails of DPPC is approximately 41.1 Å. The obtained $SLD_{DPPC}$ of -0.12 $\times 10^6$ $Å^{-2}$ indicates that the surface coverage is approximately 95%. After the characterization of the DPPC bilayer, K18 protein was added into the system. The ~7 hour incubation of the bilayer with 5 µM protein had no significant effect on the thickness or the SLD of the DPPC bilayer. This indicates that K18 has small or no effect on the neutrally charged model membrane. Only a slight

change was recorded in the thickness of water layer between quartz and the bilayer. The thickness of this layer changed from 26 to 23 Å.

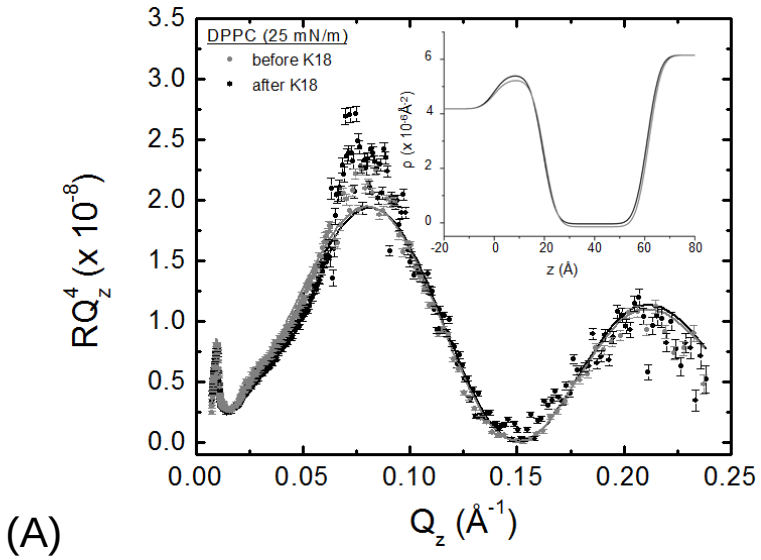


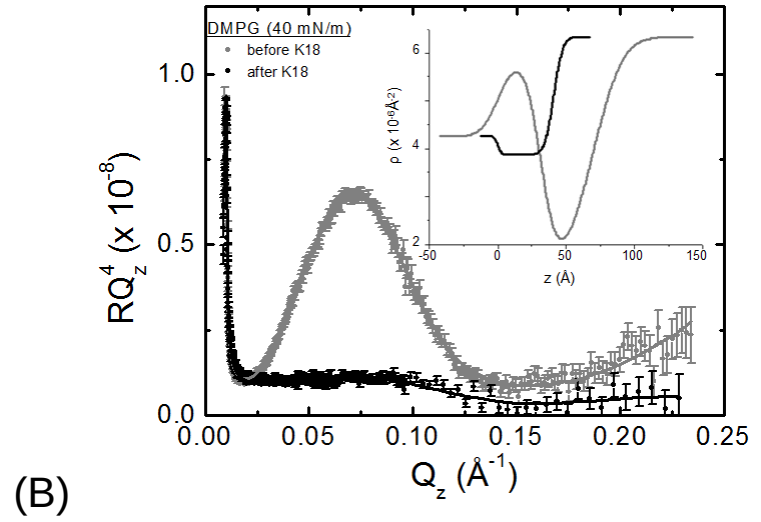


Figure 3.15 Reflectivity ($RQ_z^4$ vs. $Q_z$) and corresponding SLD profiles (inset) of a DPPC (A) and DMPG (B) bilayer measured in $D_2O$ with (black) and without (gray) K18.

The error bars in Figure 3.5 denote the standard deviation for each measurement**.** The bilayers were deposited utilizing the Langmuir-Blodgett/Langmuir-Schaefer technique at the surface pressures of 25 mN/m (A) and 40 mN/m (B).

Table 3.15 Fit Parameters for DPPC Bilayer Measured in $D_2O$ with and without K18.

| | **DPPC before K18** | **DPPC after K18** |
|---|---|---|
| **Background** | 2.3e-9 ± 1e-5 | 3.0e-8 ± 6.1e-6 |
| **$Roughness_{Substrate}$** | 1.8 ± 0.1 | 5.8 ± 0.2 |
| **$Thickness_{Water}$ [Å]** | 25.5 ± 0.3 | 22.5 ± 3 |
| **$SLD_{Water} \times 10^6$ [$Å^{-2}$]** | 5.8 ± 0.4 | 5.9 ± 0.4 |
| **$Roughness_{Water}$ [Å]** | 3.7 ± 0.3 | 6.8± 0.2 |
| **$Thickness_{DPPC}$ [Å]** | 41.1 ± 0.1 | 42.3 ± 0.4 |
| **$SLD_{DPPC} \times 10^6$ [$Å^{-2}$]** | -0.12 ± 0.2 | 0.22 ± 0.3 |
| **$Roughness_{DPPC}$ [Å]** | 4.5 ± 0.1 | 2.7 ± .2 |

Table 3.16 Fit Parameters for DMPG Bilayer Measured in $D_2O$ with and without K18.

| | **DMPG before k18** | **DMPG after k18** |
|---|---|---|
| **Background** | 9.0e-7±2.5e-8 | 6.4e-8±2e-8 |
| **$Roughness_{Substrate}$** | 16.5±0.1 | 5.3±0.3±3e-8 |
| **$Thickness_{Water}$ [Å]** | 31.6±0.2 | -- |
| **$SLD_{Water}$ $\times 10^6$ [$Å^{-2}$]** | 5.8±0.1 | -- |
| **$Roughness_{Water}$ [Å]** | 9.7±0.25 | -- |
| **$Thickness_{DMPG}$ [Å]** | 38.2±0.1 | 40.9±1.5 |
| **$SLD_{DMPG}$ $\times 10^6$ [$Å^{-2}$]** | 1.5±0.1 | 3.9±0.1 |
| **$Roughness_{DMPG}$ [Å]** | 8.9±0.1 | 2.0±0.1 |

The interaction of the tau construct K18 and a negatively charged DMPG bilayer was investigated by NR in a similar solid-liquid interface cell. Reflectivity and corresponding SLD profile are shown in Figure 3.15B. Fit parameters resulting in best fits are shown in Table 3.16. Differences between neutrally charged DPPC membranes and negatively charged DMPG are immediately visible. Although LB/LS transfer was conducted at a much higher surface pressure of 40 mN/m, the surface occupancy of the resulting bilayer is much smaller than in the case of DPPC. The obtained $SLD_{DMPG}$ of 1.5 $\times 10^6$ $Å^{-2}$ indicates that the surface coverage is approximately 75%. The much higher roughness parameters obtained from the fit indicate much less organized structures. The thickness of the aqueous layer (32 Å) between the quartz wafer and the DMPG bilayer is larger as compared to similar layer studied in the DPPC case. This can be attributed to the

repulsive interaction between negatively charged DMPG headgroups and quartz surface, respectively.

The fitted thickness of the DMPG bilayer before K18 was added is 38 Å. After the addition of K18 pronounced changes in the NR can be observed. The intensity of the first interference fringe drops substantially indicating that most of the material is removed from the interface. The NR can be fitted using one layer only. The thickness of this layer is approximately 41 Å with the SLD of $3.9 \times 10^6$ Å$^{-2}$. The structure and composition of this layer is unknown but its direct contact with the quartz surface might indicate membrane patches which are attached to the interface after the DMPG bilayer is disrupted by K18 protein. Proximity of this layer to the negatively charged quartz surface can indicate some saturation of the negatively charged DMPG headgoups by the positively charged K18 tau construct.

Further tests with the K18 construct injected into bilayers of varying ratios of anionic DMPG to zwitterionic DPPC revealed that a membrane composed of even as high a ratio as 60% DMPG to 40% DPPC was not completely disrupted (Figure 3.16A-C). These results, summarized in Tables 3.17-3.19, demonstrate that K18 did not completely disrupt the mixed bilayers. The only disruption evidenced at the highest proportion of PG to PC lipids (60:40) was an increase in thickness of the water layer between the membrane and quartz, indicating a less stable membrane.

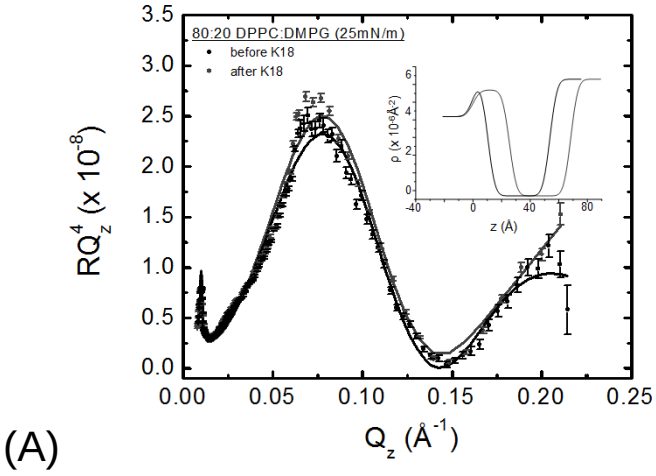


(A)

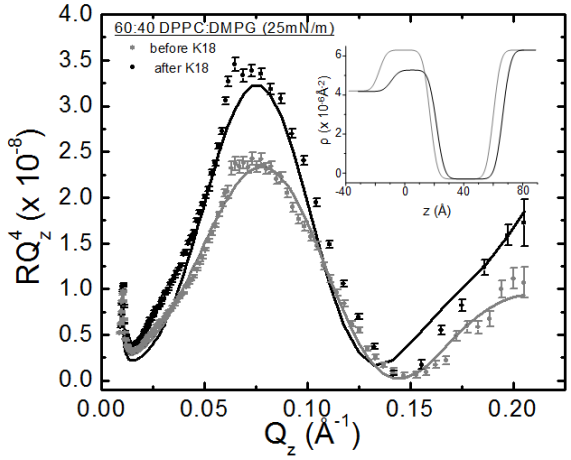


(B)

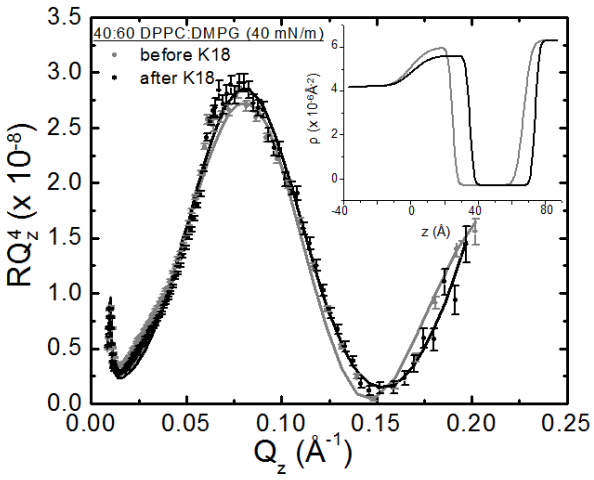


(C)

Figure 3.16 Reflectivity and corresponding SLD profiles (inset).

In Figure 3.16**,** reflectivity ($RQ_z^4$ vs. $Q_z$) and corresponding SLD profiles (inset) of 80:20 ratio (A), 60:40 ratio (B), and 40:60 ratio (C) of DPPC:DMPG bilayers show measurements in $D_2O$ with (black) and without (gray) K18. The error bars in Figure 3.16 denote the standard deviation for each measurement.

Table 3.17 Fit Parameters for 80:20 DPPC:DMPG Bilayer Measured in $D_2O$ with and without K18

| | **80:20 before K18** | **80:20 after K18** |
|---|---|---|
| **Background** | 1e-7 | 1e-7 |
| **$Roughness_{Substrate}$** | 4 (fixed) | 4 (fixed) |
| **$Thickness_{Water}$ [Å]** | 25.53 | 10.42 |
| **$SLD_{Water} \times 10^6$ [$Å^{-2}$]** | 5.68 | 6.25 |
| **$Roughness_{Water}$ [Å]** | 4 (fixed) | 4 (fixed) |
| **$Thickness_{DMPG}$ [Å]** | 42.99 | 43.49 |
| **$SLD_{DMPG} \times 10^6$ [$Å^{-2}$]** | -0.3 | -0.3 |
| **$Roughness_{DMPG}$ [Å]** | 4 (fixed) | 4 (fixed) |

Table 3.18 Fit Parameters for 60:40 DPPC:DMPG Bilayer Measured in $D_2O$ with and without K18

| | **60:40 before K18** | **60:40 after K18** |
|---|---|---|
| **Background** | 4.6e-6 | 1.99e-7 |
| **$Roughness_{Substrate}$** | 4 (fixed) | 4 (fixed) |
| **$Thickness_{Water}$ [Å]** | 34.99 | 28.85 |
| **$SLD_{Water} \times 10^6$ [$Å^{-2}$]** | 6.29 | 5.27 |
| **$Roughness_{Water}$ [Å]** | 4 (fixed) | 4 (fixed) |
| **$Thickness_{DMPG}$ [Å]** | 43.78 | 42.28 |
| **$SLD_{DMPG} \times 10^6$ [$Å^{-2}$]** | -0.3 (fixed) | -0.3 |
| **$Roughness_{DMPG}$ [Å]** | 4 (fixed) | 4 (fixed) |

Table 3.19 Fit Parameters for 40:60 DPPC:DMPG Bilayer Measured in $D_2O$ with and without K18

| | **40:60DPPC:DMPG before K18** | **40:60DPPC:DMPG after K18** |
|---|---|---|
| **Background** | 5.2e-9 ± 1.5e-8 | 2.1e-6 ± 3e-6 |
| **$Roughness_{Substrate}$** | 3.6 ± 0.4 | 2 (fixed) |
| **$Thickness_{Water}$ [Å]** | 25.0 ± 0.8 | 35.2 ± 0.25 |
| **$SLD_{Water} \times 10^6$ [$Å^{-2}$]** | 5.9 ± 0.6 | 5.6 ± 0.2 |
| **$Roughness_{Water}$ [Å]** | 7.9 ± 0.8 | 8.4 ± 1.4 |
| **$Thickness_{DMPG}$ [Å]** | 42.4 ± 0.9 | 39.8 ± 0.3 |
| **$SLD_{DMPG} \times 10^6$ [$Å^{-2}$]** | -0.3 ± 0.2 | -0.3 (fixed) |
| **$Roughness_{DMPG}$ [Å]** | 2 (fixed) | 2 (fixed) |

To study the effect of hTau40/3Epi protein on a charge neutral DPPC lipid bilayer, NR measurements have been performed using a similar solid-liquid interface cell. Reflectivity and corresponding SLD profile are shown in Figure 3.17A. The system was again described using two slabs, with the simplest physically meaningful model used to fit the data. The first slab accounts for a thin water layer between the quartz substrate and the lipid bilayer and the second for the alkyl tails of the bilayer. Fit parameters resulting in best $\chi^2$ values are included in Table 3.20. The lipid bilayer was fabricated by LB/LS transfer at 25 mN/m. The scattering length density (SLD) of the lipid tails

($SLD_{DPPC} = 0.67 \times 10^6$ $Å^{-2}$) indicates 87% coverage of the surface. The water buffer layer between quartz and the bilayer has an initial thickness of 11.3 Å. The initial thickness of the alkyl tails of DPPC is approximately 42 Å. After the characterization of the DPPC bilayer, hTau40/3Epi protein was added into the system. The 7 hour incubation of the bilayer with 5 μM of the hTau40/3Epi protein had no significant effect on the thickness or the SLD of the DPPC bilayer. This indicates that hTau40/3Epi has small or no effect on the neutrally charged model membrane. Only a slight change was recorded in the thickness of water layer between quartz and the bilayer. The thickness of this layer increased from 11.3 to 13.7 Å. Although the cause of this increase is unknown, it might be due to perturbation of the DPPC bilayer during the addition of hTau40/3Epi which required a slow exchange of the subphase during the protein injection.

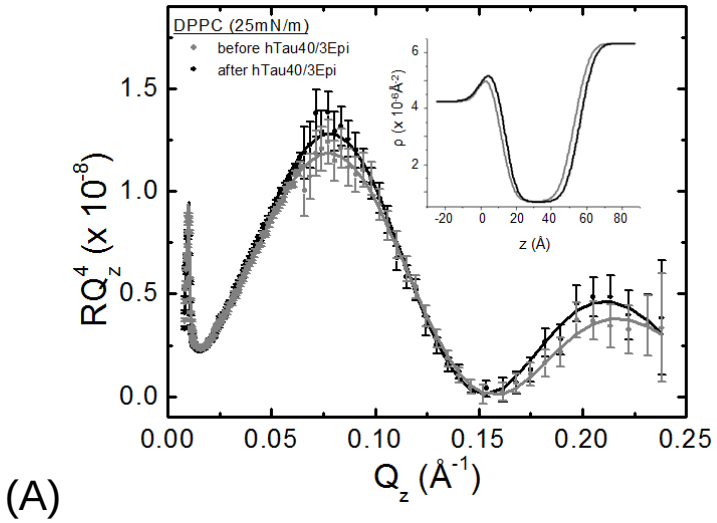


(A)

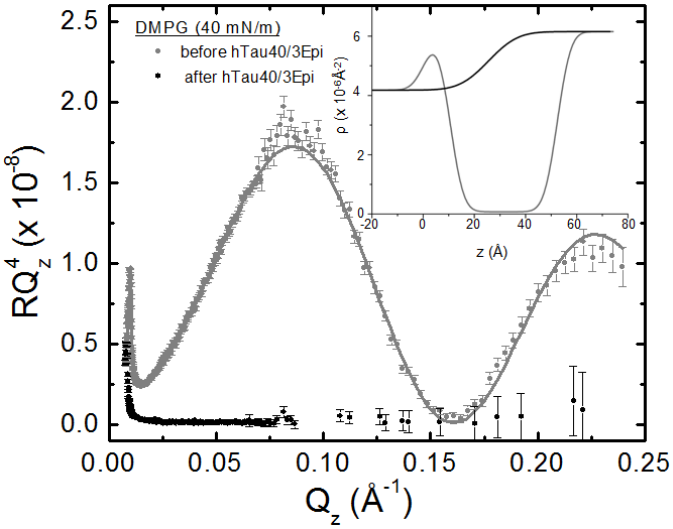


(B)

Figure 3.17 Reflectivity ($RQ_z^4$ vs. $Q_z$) and corresponding SLD profiles (inset) of a DPPC (A) and DMPG (B) bilayer measured in $D_2O$ with (black) and without (gray) hTau40/3Epi.

The Figure 3.17 error bars denote the standard deviation for each measurement. The bilayers were deposited utilizing the Langmuir-Blodgett/Langmuir-Schaefer technique at the surface pressures of 25 mN/m (A) and 40 mN/m (B).

Table 3.20 Fit Parameters for DPPC Bilayer Measured in $D_2O$ with and without hTau40/3Epi

| | **DPPC before 3Epi** | **DPPC after 3Epi** |
|---|---|---|
| **Background** | 0 (fixed) | 0 (fixed) |
| **$Roughness_{Substrate}$** | 6.6 ± 0.1 | 6.5 ± 0.1 |
| **$Thickness_{Water}$ [Å]** | 11.3 ± 0.2 | 13.7 ± 0.3 |
| **$SLD_{Water} \times 10^6$ [$Å^{-2}$]** | 5.6 ± 0.1 | 5.6 ± 0.1 |
| **$Roughness_{Water}$ [Å]** | 4.1 ± 0.6 | 4.9 ± 0.4 |
| **$Thickness_{DPPC}$ [Å]** | 41.6 ± 0.1 | 42.3 ± 0.1 |
| **$SLD_{DPPC} \times 10^6$ [$Å^{-2}$]** | 0.67 ± 0.04 | 0.66 ± 0.04 |
| **$Roughness_{DPPC}$ [Å]** | 5.6 ± 0.1 | 5.2 ± 0.1 |

The interaction of the hyperphosphorylation mimic hTau40/3Epi and a negatively charged DMPG bilayer was investigated by NR in a similar solid-liquid interface cell. Reflectivity and corresponding SLD profile are shown in Figure 3.17B. Fit parameters resulting in best fits are shown in Table 3.21. LB/LS transfer was conducted at a much higher surface pressure of 40 mN/m, and the obtained $SLD_{DMPG}$ of 0.23 $\times 10^6$ $Å^{-2}$ indicates that the surface coverage is approximately 90%. The thickness of the aqueous layer (13 Å) between the quartz wafer and the DMPG bilayer is slightly larger as compared to the similar layer studied in the DPPC case. This again can be attributed to the repulsive interaction between negatively charged DMPG headgroups and the quartz surface, respectively. The fitted thickness of the DMPG bilayer before hTau40/3Epi was added is

40 Å. After the addition of hTau40/3Epi pronounced changes in the NR can be observed. The NR can no longer be fitted, indicating that no patches of lipids in a bilayer or even micellar structure remain close to the interface once the DMPG bilayer is disrupted.

Table 3.21 Fit Parameters for DMPG Bilayer Measured in $D_2O$ with and without hTau40/3Epi

| | **DMPG before 3Epi** | **DMPG after3Epi** |
|---|---|---|
| **Background** | 0 (fixed) | 0 (fixed) |
| **$Roughness_{Substrate}$** | 4 (fixed) | 4 (fixed) |
| **$Thickness_{Water}$ [Å]** | 12.7 ± 0.5 | -- |
| **$SLD_{Water} \times 10^6$ [$Å^{-2}$]** | 5.3 ± 0.9 | -- |
| **$Roughness_{Water}$ [Å]** | 4 (fixed) | -- |
| **$Thickness_{DMPG}$ [Å]** | 40.4 ± 0.1 | -- |
| **$SLD_{DMPG} \times 10^6$ [$Å^{-2}$]** | 0.23 ± 0.06 | -- |
| **$Roughness_{DMPG}$ [Å]** | 4 (fixed) | -- |

Examinations of the tau construct K32 and its interaction with similar DPPC and DMPG bilayers were also conducted. While the results of these assays (Figure 3.18 and Tables 3.22-3.23) are not as reliable due to problems with constructing the solid-liquid interface cells, they do suggest further areas of investigation.

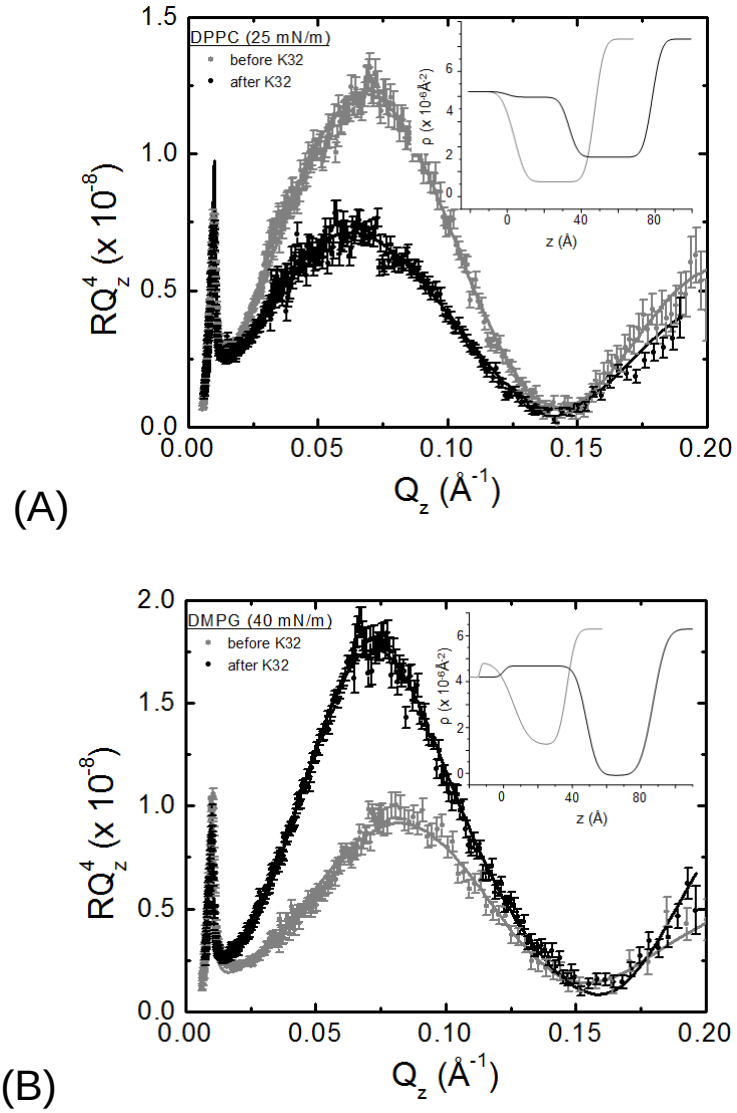


Figure 3.18 Reflectivity ($RQ_z^4$ vs. $Q_z$) and corresponding SLD profiles (inset) of a DPPC (A) and DMPG (B) bilayer measured in $D_2O$ with (black) and without (gray) K32

The Figure 3.18 error bars denote the standard deviation for each measurement. The bilayers were deposited utilizing the Langmuir-Blodgett/Langmuir-Schaefer technique at the surface pressures of 25 mN/m (A) and 40 mN/m (B).

Injection of the K32 construct into the DPPC bilayer (Figure 3.18A) caused partial disruption of the membrane, shown by the larger water thickness and the higher SLD of the DPPC layer, both of which indicate $D_2O$ has penetrated further into the membrane. The effects of injection of K32 into the DMPG bilayer (Figure 3.18B) are quite different from the effects of the other three tau proteins. Here, injection of K32 actually does not completely disrupt the bilayer. The reflectivity data retains the distinctive "two-hump" pattern indicative of a bilayer, and modeling the data affirms that while the thicknesses of the layers and the SLD of the water layer have increased, the SLD of the DMPG layer has decreased which indicates that less $D_2O$ is inside of the lipid layer.

Table 3.22 Fit Parameters for DPPC Bilayer Measured in $D_2O$ with and without K32

| | **DPPC before K32** | **DPPC after K32** |
|---|---|---|
| **Background** | 5.51e-8 | 1.81e-9 |
| **$Roughness_{Substrate}$** | 4 (fixed) | 4 (fixed) |
| **$Thickness_{Water}$ [Å]** | 5.98 | 33.49 |
| **$SLD_{Water} \times 10^6$ [$Å^{-2}$]** | 2.74 | 3.98 |
| **$Roughness_{Water}$ [Å]** | 4 (fixed) | 4 (fixed) |
| **$Thickness_{DPPC}$ [Å]** | 41.38 | 45.12 |
| **$SLD_{DPPC} \times 10^6$ [$Å^{-2}$]** | 0.59 | 1.58 |
| **$Roughness_{DPPC}$ [Å]** | 4 (fixed) | 4 (fixed) |

Table 3.23 Fit Parameters for DMPG Bilayer Measured in D2O with and without K32

| | **DMPG before K32** | **DMPG after K32** |
|---|---|---|
| **Background** | 5.51e-8 | 8.25e-7 |
| **$Roughness_{Substrate}$** | 4 (fixed) | 4 (fixed) |
| **$Thickness_{Water}$ [Å]** | 5.99 | 49.31 |
| **$SLD_{Water} \times 10^6$ [$Å^{-2}$]** | 2.74 | 4.58 |
| **$Roughness_{Water}$ [Å]** | 4 (fixed) | 4 (fixed) |
| **$Thickness_{DMPG}$ [Å]** | 41.38 | 40.03 |
| **$SLD_{DMPG} \times 10^6$ [$Å^{-2}$]** | 0.56 | -0.28 |
| **$Roughness_{DMPG}$ [Å]** | 4 (fixed) | 4 (fixed) |

## 3.3 Discussion

### 3.3.1 *Tau constructs, K18 and K32, and mimic, hTau40/3Epi, are highly surface active*

The constructs K18 and K32, along with the hyperphosphorylation mimic hTau40/3Epi, are highly charged and soluble, but like the full-length hTau40 they adsorb readily to the air/water interface. They all exhibit significant surface activity, reaching pressures comparable to that reached by the full-length hTau40 (Figure 3.2) and to the pressure of the amphipathic Aβ40 peptide to an air/water interface (Ege & Lee, 2004). As with hTau40, the other tau proteins are intrinsically disordered which renders them prone to partition or to bind to different interfaces. All four tau proteins have a sharp initial increase in pressure indicating a high affinity to the hydrophobic interface. GIXD

measurements of the adsorbed tau protein films reveal no diffraction peaks, indicating no long-range repeat structures in the plane of the films are formed at the air/water interface. As our previous work with hTau40 describes, however, this does not rule out the possible formation of local, nonproprogating, secondary structures or amorphous aggregates of the proteins at the air/water interface.

### 3.3.2 *K18, K32 and hTau40/3Epi strongly interact with negative membranes*

In order to more fully understand the role interaction with negative membranes plays in mediating the dynamics of K18, K32 and hTau40/3Epi, we investigated the interactions between two types of model lipid membranes and the tau constructs and mutant. The Langmuir monolayer modeled one leaflet of the plasma membrane, while the supported lipid bilayers provided a model of both leaflets of the membrane. Both constant pressure and constant area insertion assays demonstrated that like the wildtype hTau40, K18, K32 and hTau40/3Epi strongly associated and inserted into the anionic DMPG monolayer (Figure 3.4). The K18 MTB domain construct is very membrane-active even without the projection domain, presumably mediated in part by the attractive electrostatic interactions between the overall positively charged K18 (Figure 3.1) and the lipids. This strong affinity of the MT binding domain for anionic membranes is also in agreement with previous reports of K18 aggregating in the presence of anionic lipid vesicles (Elbaum-Garfinkle et al., 2010). The addition of the two flanking, proline-rich domains to either side of the MTB domain in the K32 construct lowered the rate at which the protein adsorbed but did not prevent it from the interaction. Even with the addition of further negative charge through the mutation of select amino acids (Figure 3.1), the hyperphosphorylation mimic

hTau40/3Epi interacted strongly with anionic membranes. Both K18 and hTau40/3Epi also demonstrated a selective affinity toward anionic membranes by disrupting only supported DMPG bilayers while leaving the zwitterionic DPPC bilayer intact (Figure 3.15 and 3.17). Our findings give further evidence toward the MTB domain's role in the affinity of the tau protein for anionic membranes. They also suggest that even in a diseased, hyperphosphorylated state, the tau protein retains this affinity.

### 3.3.3 *Air/Water and lipid membrane interfaces induce K18, K32 and hTau40/3Epi structural compaction*

The films of the four tau proteins – hTau40, K18, K32 and hTau40/3Epi – adsorbed to the air/water interface are approximately 20-25 Å thick and are not homogenous in electron density perpendicular to the film surface (Figure 3.3). At the hydrophobic air phase, a layer ~10 Å thick, with a $\rho/\rho_{H2O}$ approaching 1.3, forms. A more diffuse layer of $\rho/\rho_{H2O}$ ~1 then extends out into the water phase.

Modeling of hTau40, K18, K32 and hTau40/3Epi inserted into a DMPG monolayer (Figure 3.6-3.9) shows that all four associated with and partially inserted into the lipid membrane. The wildype hTau40, the MT binding domain K18, the MTB plus flanking regions K32 and the hyperphosphorylation mimic Tau40/3Epi all gave rise to a ~15 Å layer of protein inserted in the membrane with a density of about 1.3, followed by a more diffuse layer of ~9 Å underneath the DMPG headgroups with a density close to 1 extending into the water phase. As previously described, the radius of gyration ($R_g$) of the intrinsically disordered hTau40 in solution (determined by small-angle X-ray scattering) has been reported to be 65 Å, (Mylonas et al., 2008) much larger than a globular, folded protein

of ~400 amino acids with $R_g$ typically ranging from 20 to 25 Å. Furthermore, a $\rho/\rho_{H2O}$ of 1.3 of the more dense portion of the layers at the air/water and membrane interfaces is comparable to the density of folded proteins that have an average specific volume of 0.73, which corresponds to a density of 1.37 g/mL (Lee & Timasheff, 1974). GIXD measurements of this data showed that all the tau proteins built up at the interface over time, indicating that the tau proteins partitioned to the interface and began to form amorphous aggregates.

For the GIXD studies of hTau40, K18, K32 and hTau40/3Epi proteins incubated with DMPG monolayers at constant area for 12 hours, the presence of a new diffraction peak at $Q_{xy}$ ~ 1.325 $Å^{-1}$ was detected. That peak (with smaller intensity) was also present for shorter (~2 hour) incubation times but only for K18 and hTau40/3Epi proteins. The *d*-spacings associated with these peaks are ~ 4.75 (± 0.03) Å and the out-of-plane length of the coherently scattering units associated with these peaks and obtained from the *Bragg rod* fits are from 4.5 to 7.2 Å. The in-plane coherence lengths calculated from the FWHMs of the *Bragg peaks* vary from 110 to 200 Å and correspond to 23 - 42 *d*-spacings. For the K18 and hTau40/3Epi cases, the integrated intensities of the peaks increased significantly with the incubation time indicating increased amount of material accumulating at the surface. The *d*-spacing of 4.75 Å closely matches the distance between *β*-sheets units in A*β* fibrils (Chi et al., 2008).

Taken together, our structural measurements of air/water interface-adsorbed and membrane interface-associated tau layers of a smaller dimension and higher density compared to tau in solution suggest that along with our previous findings on the wildtype hTau40 (Jones et al., 2012), as the tau constructs and mimic partition to interfaces, at least

a portion undergoes structural compaction to resemble the density of a folded protein. This conformational change may also be accompanied by protein-protein interactions that lead to amorphous aggregation of tau protein at the interfaces. Our GIXD measurements of the tau proteins forming structures at anionic membrane interfaces which indicate the formation of β-sheet fibrils also strongly points to the formation of misfolded aggregates at the surface.

In addition to previous reports on the ability of anionic membranes to induce tau fibrillization ( Chirita et al., 2003; Elbaum-Garfinkle et al., 2010) and the ability of anionic membrane to induce structural compaction of the full length hTau40 (Jones et al., 2012), the ability of anionic membrane to also strongly induce structural compaction of K18 described here suggests that the MT binding domain of tau plays a vital role in the early structural changes that can then lead to fibrillization. Anionic membrane also induced structural compaction of the mutant hyperphosphorylation mimic. Structurally compacted conformations of the full-length tau protein that exhibit enhanced aggregation propensity have been shown in several cases, including phosphorylation at several sites diagnostic of AD (Jeganathan et al., 2006; Jeganathan et al., 2008) binding to exogenous aggregation inducers (Chirita et al., 2005) and fast heating/cooling (Shkumatov et al., 2011). We show here that the binding of the tau constructs K18 and K32 and the mimic hTau40/3Epi to a hydrophobic interface (the air/water interface), and the binding of K18, K32 and hTau40/3Epi to a physiological membrane interface, can also induce structural compaction and lead to fibril formation.

### 3.3.4 *K18, K32 and hTau40/3Epi association with lipid membranes disrupts lipid packing and membrane integrity*

We observed morphological changes to the DMPG lipid monolayer caused by the insertion of the tau construct K18 and mimic hTau40/3Epi. As we previously showed in our hTau40-membrane study (Jones et al., 2012), disruption to monolayer morphology can be indicative of disruption to lipid packing. An overall increase in the ratio of light LE phase to dark LC phase can be caused by preferential insertion of the proteins into the more fluid LE region and/or disruption of the ordered LC domains. The decrease in size of LC domains indicates that the insertion disrupts lipid packing in the LC domains, which is corroborated by GIXD data. On the molecular level, K18 or hTau40/3Epi insertion into DMPG monolayers disrupted the ordered packing of lipid tails.

We used NR experiments to assess lipid bilayer structural integrity before and after the addition of K18, K32 or hTau40/3Epi. Both K18 and hTau40/3Epi selectively disrupted anionic DMPG lipid bilayers even at lipid packing densities higher than those of a cell membrane. The neutrally charged DPPC bilayer, however, was unaffected by addition of either K18 or hTau40/3Epi.

Our results confirm that the MT binding domain of tau, K18, the MTB domain plus the flanking regions, K32, and the hyperphosphorylation mimic, hTau40/3Epi, interact with an anionic monolayer at the air/water interface, but also with more physiologically relevant lipid bilayers. They also disrupted lipid membrane structure on a molecular scale by disrupting lipid packing and on a morphological scale by completely disrupting lipid bilayer integrity. However, a lipid bilayer of even only 40% PC lipids to 60% anionic lipids, was not completely disrupted by the addition of the MTB domain, K18.

### 3.4 Conclusions

Our results provide some understanding of the effects of domain composition and phosphorylation on the interaction of tau protein with lipid membranes. Although the projection domain is absent in the K18 and K32 constructs, both were highly surface active. K18 strongly associated with anionic membranes which disrupted lipid packing and membrane integrity. The mutant hyperphosphorylation mimic hTau40/3Epi, despite containing additional negative charge from the mutations in the regions flanking the MT binding domain, was also highly surface active and strongly interacted with negative membranes, disrupting lipid packing and membrane integrity.

For K18 and hTau40/3Epi, the hydrophobic air/water interface and the anionic lipid membrane interface induced the intrinsically disordered proteins to partially adopt a more compact conformation similar to a folded protein. The behavior of the K18 MT binding domain construct suggests that this domain plays an essential role in both tau misfolding and aggregation and in exerting toxicity *via* membrane destabilization. Despite the addition of extra negative charges mimicking a diseased hyperphosphorylated state, the hTau40/3Epi mutant also exhibited a strong affinity to both adsorb to the air/water interface and associate with and intercalate into negatively charged lipid monolayers and bilayers.

These results indicate that hyperphosphorylation of the tau protein, as seen in a diseased state, did not prevent interaction of tau protein with negatively charged lipid membranes that lead to misfolding and structural compaction of the tau protein and may seed the assembly of tau into fibrils. Furthermore, just as in the case of the wild type hTau40 protein, the interaction of hTau40/3Epi with anionic lipid membranes disrupted lipid packing and destabilized the membrane. Hyperphosphorylation of the tau protein,

which occurs early during the pathogenesis of Alzheimer's disease, causes detachment of tau from microtubules.

We demonstrate that hTau40/3Epi, mimicking this free tau, is then capable of interacting with anionic lipids in the plasma membrane. This interaction could then both seed formation of PHFs and disrupt the lipid membrane, a proposed mechanism of protein aggregate-induced toxicity in diseased cells. We propose that hTau40/3Epi's ability to still interact with negatively charged membranes and overcome any repulsive force because of its additional negative charge is likely due to the fact that it still contains the positively charged repeat domains which make up the K18 construct which strongly interacts with anionic membranes.

### 3.5 Materials and Methods

Full-length human tau isoform (hTau40, 441 residues), a mutant hyperphosphorylation mimic (hTau40/3Epi, 441 residues), and the MT binding repeat domain (K18, 130 residues) and the MT binding domain plus the flanking regions (K32, 196 residues) were synthesized and purified as previously described (Figure 3.1) (Gustke et al., 1994; Trinczek et al., 1995). Two lipids were used to evaluate the effect of lipid headgroup charge on tau–membrane interactions:

anionic 1,2-dimyristoyl-*sn*-glycero-3-[phospho-*rac*-(1-glycerol)] (DMPG) and zwitterionic 1,2-dipalmitoyl-*sn*-glycero-3-phosphocholine (DPPC) (Figure 3.19C).

Lipids were purchased from Avanti Polar Lipids and used as received. DPPC was dissolved in chloroform ($CHCl_3$) (HPLC grade, Fisher Scientific) while DMPG was dissolved in 10 vol % methanol (MeOH) in chloroform. For FM, the headgroup-labeled fluorescent dye

Texas Red 1,2-dihexadecanoyl 3-phosphoethanolamine (TR-DHPE) (Molecular Probes) was first dissolved in chloroform and subsequently added to lipid spreading solutions at 0.5 mol %. Lipid stock solutions ranged from 2 to 10 mg/mL were prepared and then diluted to 0.2 or 0.5 mg/mL for spreading solutions. All lipid solutions were stored at −20 °C in glass vials.

### 3.5.1 *Adsorption of tau proteins to air/water interface*

To evaluate the surface activity of the wildtype, mutant and K18 construct, the surface pressure ($\pi$) measured by the adsorption of the proteins from a water subphase was measured. The experiment was carried out at 25 °C and on a 45 mL water subphase (Milli-Q system, Millipore, Bedford, MA) using a MiniMicro Langmuir trough (KSV Instruments Ltd., Finland). A Wilhelmy plate sensor at the center of the trough measured $\pi$ of the lipid monolayer where $\pi = \gamma_0 - \gamma$ and $\gamma_0$ is the air/water surface tension and $\gamma$ is the lipid film surface tension. The trough had a working surface area of 86.39 $cm^2$. Before injecting protein into the subphase, barriers were partially closed to give a total surface area of 45 $cm^2$, roughly the same as the surface area of the lipid monolayers compressed to 25 mN/m for the subsequent insertion experiments. For a final tau concentration of 1μM, 1 mL of 45μM tau was injected into the subphase using a gastight glass microsyringe (Hamilton, Reno, NV).

### 3.5.2 *Constant pressure insertion assay and fluorescence microscopy*

To evaluate the interactions between the tau proteins and lipid membranes, insertion of tau into lipid monolayers at the air/water interface held at a constant π was measured (Figure 3.19A). All experiments were carried out on water subphase and at room temperature. Lipids were first spread at the air/water interface. The barriers then symmetrically compressed the monolayer at 0.3 mm/s to a target π of 25 mN/m, and this π was kept constant *via* a feedback loop. A π of 25 mN/m was chosen for its relevance to physiological conditions as the lipid-packing density of a bilayer is reported to roughly correspond to that of a monolayer at 30 mN/m (Ege & Lee, 2004; Seelig, 1987).

The speed at which the barriers moved to maintain this target pressure was controlled by the feedback loop and depended upon how fast the barriers needed to expand or contract in response to a perturbation, for example, rate of tau insertion. A maximum barrier speed of 3 mm/min was set during the constant pressure duration of the experiment. Protein was then injected into the subphase underneath the monolayer into the water subphase *via* an injection port on the side of the trough below the level of the subphase to achieve a final 1 μM concentration. Since the monolayer was kept at a constant π, the barriers expanded as a result of protein insertion. Monolayer surface area was recorded, and the % area expansion was taken as a measure of favorable tau–lipid interactions. Surface area expansion is defined as $\Delta A/A = (A - A_i)/A_i$, where $A$ is the surface area at time $t$ and $A_i$ is the initial surface area of the monolayer when it reached 25 mN/m.

To monitor lipid monolayer morphological change during tau insertion, the trough was positioned on top of a motorized stage of an inverted optical microscope

(Olympus IX 71) with a 50× objective centered on a quartz window in the bottom of the trough. A 100 W mercury lamp was used for fluorescence excitation. Fluorescence images were collected by a QImaging camera (EXi Blue, QImaging Photometrics) and analyzed using the software QCapture Pro. 0.5 mol % TR-DHPE was included in the spreading solution. Because of steric hindrance, the dye partitions into the liquid-expanded (LE) phase rather than the liquid-condensed (LC) phase, giving rise to fluorescence contrast (Knobler, 1990).

### 3.5.3 *Constant area insertion assay*

To evaluate the interactions between the tau proteins and lipid membranes, insertion of tau into lipid monolayers at the air/water interface held at a constant area was measured. In these experiments, a needle was inserted directly into the lipid monolayer from above to inject into the water subphase. All experiments were carried out on water subphase and at room temperature. Lipids were first spread at the air/water interface. Protein was then injected into the subphase underneath the monolayer to achieve a final 1 μM concentration. Since the monolayer was kept at a constant area *via* a feedback loop, the pressure increased as a result of protein insertion. The amount of pressure increase was taken as a measure of favorable tau–lipid interactions.

### 3.5.4 *X-ray scattering measurements*

Grazing-incidence X-ray diffraction (GIXD) and X-ray reflectivity (XR) data were collected at the BW1 beamline (HASYLAB, DESY, Hamburg, Germany) for both hTau40 adsorbed to the air/water interface and hTau40 inserted into a DMPG monolayer at the

air/water interface. XR data give information about the out-of-plane (perpendicular to the lipid film) electron density profile of the film averaged over the LE and LC phases. GIXD measurements give structural information on the in-plane (*i.e.*, in the plane of the monolayer) ordered (hence diffracting) portion of the film. Presence of Bragg peaks in GIXD data indicates 2D ordered structures. The theory of XR and GIXD has been presented in detail elsewhere (Als-Nielsen et al., 1994; Als-Nielsen & Kjær, 1990).

The synchrotron X-ray beam was monochromated to a wavelength (λ) of around 1.304 Å by Bragg reflection from a beryllium (200) monochromator crystal in Laue geometry. By tilting the reflecting crystal planes out of the vertical plane the monochromatic beam was deflected down to impinge on the horizontal liquid surface at a shallow glancing angle. All experiments were carried out in an ultrasmall volume Langmuir trough liquid diffractometer (20 mL subphase volume) at 23 °C and an hTau40 concentration of 1 μM in pure water. The trough was temperature controlled and equipped with a Wilhelmy balance for surface pressure measurements and a motorized barrier for surface area variation was mounted on the diffractometer. During the XR experiments at low incident angles, due to the small dimensions of the trough, the footprint of the beam was larger than the size of the trough. Therefore, the normalized XR data were truncated to only include data at which the footprint of the incoming beam is smaller than the size of the trough.

For the XR experiments, reflectivity, *R*, is defined as the ratio of the intensity of X-rays specularly reflected from a surface relative to that of the incident X-ray beam measured as a function of wave-vector transfer ($Q_z = |\mathbf{k}_{out} - \mathbf{k}_{in}| = 4\pi \sin\theta/\lambda$, where θ is the grazing angle and λ is the wavelength of the X-ray beam). The *R* profile contains

information on the sample-normal profile of in-plane average of the electron density. Chemically distinct molecular layers (*e.g.*, proteins, lipid headgroups and tails) have different electron densities. Electron density profile of a film, therefore, gives us information on the location and thickness of the protein layer associated with the lipids (Als-Nielsen et al., 1994; Jensen & Kjaer, 2001). The absolute $R$ was derived by subtracting background followed by normalization to the incident beam flux. The data was reduced and plotted as $R/R_F$ versus $Q_z$ (the division by Fresnel reflectivity, $R_F$, increases the visibility of the reflectivity profile by removing a sharp $Q_z^{-4}$ decrease of the reflectivity due to Fresnel's law). The error bars on the data represent the statistical errors in the measurements (standard deviation, $\sigma R$).

Analysis of the measured reflectivity profiles was performed using a free form StochFit fitting routine (Danauskas et al., 2008; Pedersen & Hamley, 1994). StochFit utilizes a stochastic procedure for analyzing XR data of thin films at an interface. StochFit first provides a model-independent electron density profile (ρ) of the XR data, after which ρ is fit with a box model with smeared interfaces to extract physically meaningful results (Chi et al., 2010). Each box represents a layer of distinct chemical composition, thus ρ. From the box model fitting, lengths, ρ normalized to that of water $\rho_{H2O}$, ($\rho/\rho_{H2O}$), and interfacial roughness values are reported for each box.

For the GIXD experiments, the X-ray beam was adjusted to strike the surface at an incident angle of 0.11°, which corresponds to a $q_z = 0.85Q_c$, where $Q_c = 0.02176$ Å$^{-1}$ is the critical scattering vector for total external reflection from the liquid subphase. At this angle the incident wave is totally reflected, while the refracted wave becomes evanescent,

traveling along the liquid surface. Such a configuration maximizes surface sensitivity. The dimension of the X-ray beam footprint on the liquid surface was approximately $2 \times 50$ mm$^2$ and was bigger than the width of the ultrasmall volume Langmuir trough we used. This caused over illumination of the sample and small increases in the scattering background. The scattered intensity was measured by scanning over a range of horizontal scattering vectors, $Q_{xy}$, the combination of horizontal components $Q_x$ and $Q_y$ (Als-Nielsen et al., 1994; Als-Nielsen & Kjær, 1990). Bragg peaks are intensity resolved in the $Q_{xy}$-direction and integrated over channels along the *z*-direction in the position sensitive detector. The position of the maxima of the Bragg peaks, $Q_{xy}^{max}$, was used to calculate the repeat distances $d = 2\pi/Q_{xy}$ of the 2D lattice. The widths of the peaks, corrected for the instrument resolution, were used to determine the 2D crystalline in-plane coherence length, $L_{xy}$ (the average distance in the direction of the reciprocal lattice vector $Q_{xy}$ over which there is "near-perfect" crystallinity).

### 3.5.5 *Neutron reflectivity measurements*

Neutron reflectometry (NR) experiments were performed on mutant or K18 tau construct associated with supported lipid bilayers using the Surface ProfilE Analysis Reflectometer, or SPEAR, at Los Alamos National Lab (Dubey et al., 2011). Methods and measurement of NR using SPEAR have been previously described (Dubey et al., 2010). In general, lipid bilayers were created using a Langmuir–Blodgett/Langmuir–Schaefer deposition method. 1 mg/mL DMPG in 9:1 $CHCl_3$:MeOH and DPPC in $CHCl_3$ were used as spreading solutions. Lipids were spread at the air–water interface in a Langmuir trough and compressed to a target pressure of 25 or 40 mN/m. A quartz substrate was drawn

through the air–water interface to deposit the first layer, then rotated, and driven back through the interface to deposit the second layer. A solid–liquid interface cell (Figure 3.19B) was then assembled and purged with $D_2O$. After collecting NR data of the pure lipid bilayer, which takes about an hour and half, an aliquot of 5 μM protein in deuterated PBS was injected into the flow cell, allowed to equilibrate for 20 min, and NR data were collected again.

Neutrons entered the lateral face of the substrate and were scattered from the substrate–subphase interface. $D_2O$ provided scattering contrast between the substrate, hydrogen-rich bilayer, and subphase. Similar contrast conditions can also be obtained by using deuterated lipids in a subphase of $H_2O$, but no additional information relevant to this publication can be obtained by performing NR measurements in both the contrast conditions. Therefore, NR measurements were performed on hydrogenated lipid bilayers in a $D_2O$ subphase. During the experiments, the ratio of elastically scattered to incident neutrons, or reflectivity ($R$), was measured as a function of the momentum-transfer vector $Q_z$. Analysis of the NR data provided information about coherent scattering-length density (SLD) distribution normal to the sample.

SLD is a value unique to a particular chemical composition and is the sum of coherent scattering lengths of constituent elements divided by the volume that they occupy. The continuous function SLD often can be well approximated by a number of layers, or boxes, each with a constant and distinct SLD. Interlayer roughness can be taken into account using an error function centered at each interface (Chi et al., 2008). The incident neutron beam is refracted at each interface and a theoretical NR curve can be calculated using the Parratt recursion formula (Parratt, 1954). The measured and theoretical NR

curves are compared, and using genetic optimization and the Levenberg–Marquardt nonlinear least-squares method, the best least-squares fit, corresponding to the lowest $\chi^2$ value, is obtained (Nelson, 2006). The simplest SLD model that gave good fits of physical relevance was used to interpret the NR data.

### 3.6 Supplemental materials

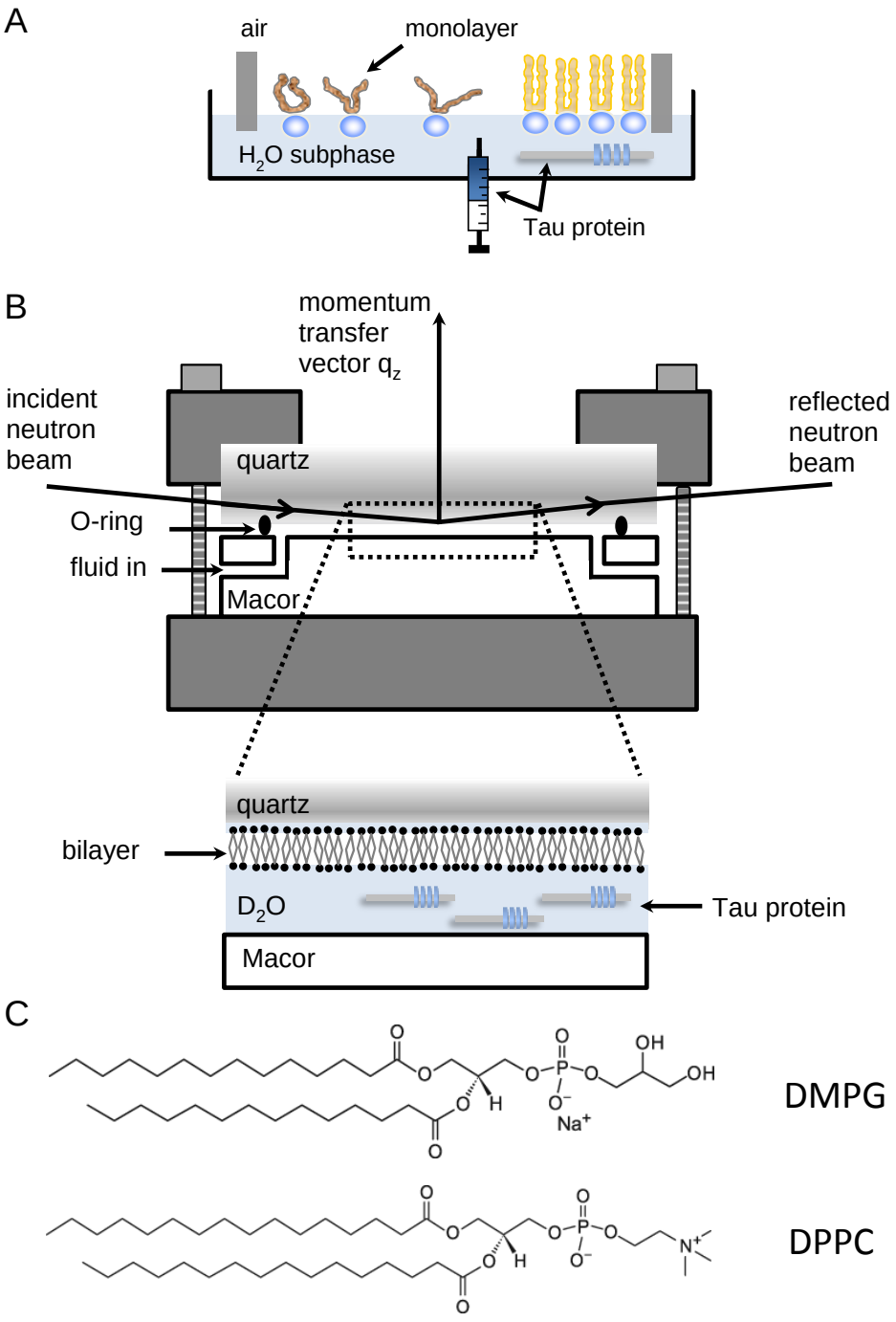


Figure 3.19 Supplementary: Schematics of (A) a Langmuir trough insertion assay, (B) a solid-liquid interface cell, and (C) the lipids used in the monolayer and bilayer experiments.

## 3.7 References


Als-Nielsen, J., Jacquemain, D., Kjaer, K., Leveiller, F., Lahav, M., & Leiserowitz, L. (1994). Principles and applications of grazing incidence X-ray and neutron scattering from ordered molecular monolayers at the air-water interface. *Physics Reports, 246*(5), 251-313.

Als-Nielsen, J., & Kjær, K. (1990). X-ray reflectivity and diffraction studies of liquid surfaces and surfactant monolayers. In T. Riste & D. Sherrington (Eds.), *Phase Transitions in Soft Condensed Matter* (Vol. 211, pp. 113-138): Springer US.

Barghorn, S., & Mandelkow, E. (2002). Toward a unified scheme for the aggregation of tau into Alzheimer paired helical filaments. *Biochemistry, 41*(50), 14885-14896.

Buée, L., Bussière, T., Buée-Scherrer, V., Delacourte, A., & Hof, P. R. (2000). Tau protein isoforms, phosphorylation and role in neurodegenerative disorders. *Brain Research Reviews, 33*(1), 95-130.

Chi, E. Y., Ege, C., Winans, A., Majewski, J., Wu, G., Kjaer, K., et al. (2008). Lipid membrane templates the ordering and induces the fibrillogenesis of Alzheimer's disease amyloid-β peptide. *Proteins: Structure, Function, and Bioinformatics, 72*(1), 1-24.

Chi, E. Y., Frey, S. L., Winans, A., Lam, K. L. H., Kjaer, K., Majewski, J., et al. (2010). Amyloid-² fibrillogenesis seeded by interface-induced peptide misfolding and self-sssembly. *Biophysical Journal, 98*(10), 2299-2308.

Chirita, C., Necula, M., & Kuret, J. (2003). Anionic micelles and vesicles induce tau fibrillization in vitro. *Journal of Biological Chemistry, 278*(28), 25644-25650.

Chirita, C. N., Congdon, E. E., Yin, H., & Kuret, J. (2005). Triggers of full-length tau aggregation: A role for partially folded intermediates. *Biochemistry, 44*(15), 5862-5872.

Cleveland, D. W., Hwo, S.-Y., & Kirschner, M. W. (1977). Physical and chemical properties of purified tau factor and the role of tau in microtubule assembly. *Journal of Molecular Biology, 116*(2), 227-247.

Danauskas, S. M., Li, D., Meron, M., Lin, B., & Lee, K. Y. C. (2008). Stochastic fitting of specular X-ray reflectivity data using StochFit. *Journal of Applied Crystallography, 41*, 1187-1193.

Demuro, A., Mina, E., Kayed, R., Milton, S. C., Parker, I., & Glabe, C. G. (2005). Calcium dysregulation and membrane disruption as a ubiquitous neurotoxic mechanism of soluble amyloid oligomers. *J Biol Chem, 280*(17), 17294-17300.

Dubey, M., Jablin, M. S., Smith, H., & Majewski, J. (2010). Investigations of surrogate cellular membranes using neutron reflectometry. *Acta Crystallographica Section D, Biological Crystallography, 66*, 1237-1243.

Dubey, M., Jablin, M. S., Wang, P., Mocko, M., & Majewski, J. (2011). SPEAR — ToF neutron reflectometer at the Los Alamos Neutron Science Center. *The European Physical Journal Plus, 126*(11), 1-11.

Ege, C., & Lee, K. Y. C. (2004). Insertion of Alzheimer's Aβ40 peptide into lipid monolayers. *Biophysical Journal, 87*(3), 1732-1740.

Elbaum-Garfinkle, S., Ramlall, T., & Rhoades, E. (2010). The role of the lipid bilayer in tau aggregation. *Biophysical Journal, 98*(11), 2722-2730.

Frost, B., Ollesch, J., Wille, H., & Diamond, M. I. (2009). Conformational diversity of wild-type Tau fibrils specified by templated conformation change. *J Biol Chem, 284*(6), 3546-3551.

Gendron, T. F., & Petrucelli, L. (2009). The role of tau in neurodegeneration. *Molecular Neurodegeneration, 4*(1), 13.

Goedert, M., Jakes, R., Spillantini, M. G., Hasegawa, M., Smith, M. J., & Crowther, R. A. (1996). Assembly of microtubule-associated protein tau into Alzheimer-like filaments induced by sulphated glycosaminoglycans. [10.1038/383550a0]. *Nature, 383*(6600), 550-553.

Gustke, N., Trinczek, B., Biernat, J., Mandelkow, E. M., & Mandelkow, E. (1994). Domains of tau protein and interactions with microtubules. *Biochemistry, 33*(32), 9511-9522.

Ihara, Y., Nukina, N., Miura, R., & Ogawara, M. (1986). Phosphorylated tau protein is integrated into paired helical filaments in Alzheimer's disease. *Journal of Biochemistry, 99*(6), 1807-1810.

Jeganathan, S., von Bergen, M., Brutlach, H., Steinhoff, H.-J., & Mandelkow, E. (2006). Global hairpin folding of tau in solution. *Biochemistry, 45*(7), 2283-2293.

Jeganathan, S., von Bergen, M., Mandelkow, E.-M., & Mandelkow, E. (2008). The natively unfolded character of tau and its aggregation to Alzheimer-like paired helical filaments. *Biochemistry, 47*(40), 10526-10539.

Jensen, T. R., & Kjaer, K. (2001). Structural properties and interactions of thin films at the air-liquid interface explored by synchrotron X-Ray scattering. In D. Möbius & R. Miller (Eds.), *Studies in Interface Science* (Vol. Volume 11, pp. 205-254): Elsevier.

Jones, E. M., Dubey, M., Camp, P. J., Vernon, B. C., Biernat, J., Mandelkow, E., et al. (2012). Interaction of tau protein with model lipid membranes induces tau structural compaction and membrane disruption. *Biochemistry, 51*(12), 2539-2550.

Kayed, R., Sokolov, Y., Edmonds, B., McIntire, T. M., Milton, S. C., Hall, J. E., et al. (2004). Permeabilization of lipid bilayers is a common conformation-dependent activity of soluble amyloid oligomers in protein misfolding diseases. *J Biol Chem, 279*(45), 46363-46366.

King, M. E., Gamblin, T. C., Kuret, J., & Binder, L. I. (2000). Differential assembly of human tau isoforms in the presence of arachidonic acid. [10.1046/j.1471-4159.2000.0741749.x]. *Journal of Neurochemistry, 74*(4), 1749-1757.

Knobler, C. M. (1990). Seeing phenomena in flatland: Studies of monolayers by fluorescence microscopy. *Science, 249*, 870-874.

Kosik, K. S., Joachim, C. L., & Selkoe, D. J. (1986). Microtubule-associated protein tau (tau) is a major antigenic component of paired helical filaments in Alzheimer disease. *Proceedings of the National Academy of Sciences, 83*(11), 4044-4048.

Kovacech, B., Skrabana, R., & Novak, M. (2010). Transition of tau protein from disordered to misordered in Alzheimer's disease. *Neurodegener Dis, 7*(1-3), 24-27.

Lee, J. C., & Timasheff, S. N. (1974). Partial specific volumes and interactions with solvent components of proteins in guanidine hydrochloride. *Biochemistry, 13*(2), 257-265.

Mandelkow, E., von Bergen, M., Biernat, J., & Mandelkow, E. M. (2007). Structural principles of tau and the paired helical filaments of Alzheimer's disease. *Brain Pathol, 17*(1), 83-90.

Morishima-Kawashima, M., Hasegawa, M., Takio, K., Suzuki, M., Yoshida, H., Watanabe, A., et al. (1995). Hyperphosphorylation of tau in PHF. *Neurobiology of Aging, 16*(3), 365-371.

Mylonas, E., Hascher, A., Bernado, P., Blackledge, M., Mandelkow, E., & Svergun, D. I. (2008). Domain conformation of tau protein studied by solution small-angle X-ray scattering. *Biochemistry, 47*(39), 10345-10353.

Nelson, A. (2006). Co-refinement of multiple-contrast neutron/X-ray reflectivity data using MOTOFIT. *Journal of Applied Crystallography, 39*, 273-276.

Parratt, L. G. (1954). Surface studies of solids by total reflection of X-rays. *Physical Review, 95*(2), 359-369.

Pedersen, J. S., & Hamley, I. W. (1994). Analysis of neutron and X-ray reflectivity data by constrained least-squares methods. *Physica B: Condensed Matter, 198*(1–3), 16-23.

Poorkaj, P., Bird, T. D., Wijsman, E., Nemens, E., Garruto, R. M., Anderson, L., et al. (1998). Tau is a candidate gene for chromosome 17 frontotemporal dementia. *Ann Neurol, 43*(6), 815-825.

Seelig, A. (1987). Local anesthetics and pressure: A comparison of dibucaine binding to lipid monolayers and bilayers. *Biochimica et Biophysica Acta, Biomembranes, 899*, 196-204.

Shkumatov, A. V., Chinnathambi, S., Mandelkow, E., & Svergun, D. I. (2011). Structural memory of natively unfolded tau protein detected by small-angle X-ray scattering. *Proteins: Structure, Function, and Bioinformatics, 79*(7), 2122-2131.

Soto, C. (2003). Unfolding the role of protein misfolding in neurodegenerative diseases. [10.1038/nrn1007]. *Nat Rev Neurosci, 4*(1), 49-60.

Spillantini, M. G., & Goedert, M. (1998). Tau protein pathology in neurodegenerative diseases. *Trends in Neurosciences, 21*(10), 428-433.

Treatments and Research. (2014). from http://www.alz.org/i-have-alz/treatments-and-research.asp

Trinczek, B., Biernat, J., Baumann, K., Mandelkow, E. M., & E., M. (1995). Domains of tau protein, differential phosphorylation, and dynamic instability of microtubules. *Molecular Biology of the Cell, 6*(12), 1887-1902.

von Bergen, M., Barghorn, S., Biernat, J., Mandelkow, E. M., & Mandelkow, E. (2005). Tau aggregation is driven by a transition from random coil to beta sheet structure. *Biochim Biophys Acta, 1739*(2-3), 158-166.

Weingarten, M. D., Lockwood, A. H., Hwo, S. Y., & Kirschner, M. W. (1975). A protein factor essential for microtubule assembly. *Proceedings of the National Academy of Sciences, 72*(5), 1858-1862.

Wille, H., Drewes, G., Biernat, J., Mandelkow, E. M., & Mandelkow, E. (1992). Alzheimer-like paired helical filaments and antiparallel dimers formed from microtubule-associated protein tau in vitro. *Journal of Cell Biology, 118*(3), 573-584.

Wilson, D. M., & Binder, L. I. (1997). Free fatty acids stimulate the polymerization of tau and amyloid beta peptides. In vitro evidence for a common effector of pathogenesis in Alzheimer's disease. *American Journal of Pathology, 150*(6), 2181-2195.

# CHAPTER 4 GREATER DISRUPTION OF LIPID MONOLAYERS WITH PRESENCE OF MODEL OSMOLYTE SUCROSE AFTER AB PROTEIN INSERTION

## 4.1 Osmolytes

Interaction between IDPs such as tau and lipid interfaces may be modulated by a variety of factors beyond the charge of the lipids contained in the membrane. One such factor that could influence protein folding and interaction with membranes is the presence of osmolytes, small co-solutes that influence and counterbalance the osmotic pressure of the cell and the cellular environment (Yancey et al., 1982). Living organisms utilize osmolytes to respond to the stresses of their environment, whether it be the harsh conditions such as high salt concentrations that extremophiles deal with or the human renal environment. The most common naturally occurring osmolytes include polyols (glucose and sucrose), urea and methylamines (Lee, 1981). Although osmolytes do not directly bind to proteins, they do influence the thermodynamics of protein folding by nonspecific interactions (Arakawa & Timasheff, 1985; Bolen, 2001; Harries & Rosgen, 2008).

Osmolytes such as sucrose are frequently used in solution chemistry to stabilize or denature proteins. Although it had been known for many years that the osmolyte urea denatures proteins (Limbourg, 1887; Spiro, 1900; Tanford, 1964), it was not until the early 1980s that the idea of small, non-organic osmolytes having the opposite, protective effect began to gain support (Arakawa & Timasheff, 1985; Hochachka et al., 2002; Yancey et al., 1982).

Sucrose is preferentially excluded over water from the protein surface, which exerts non-specific interfacial effects on proteins. This increases the surface tension of the

protein/solvent interface, driving the stabilization of protein structure as the protein conformation equilibrium is shifted to a more folded state (Figure 4.1). More specific discussion of the energetics involved has been described previously (Anaya, 2013).

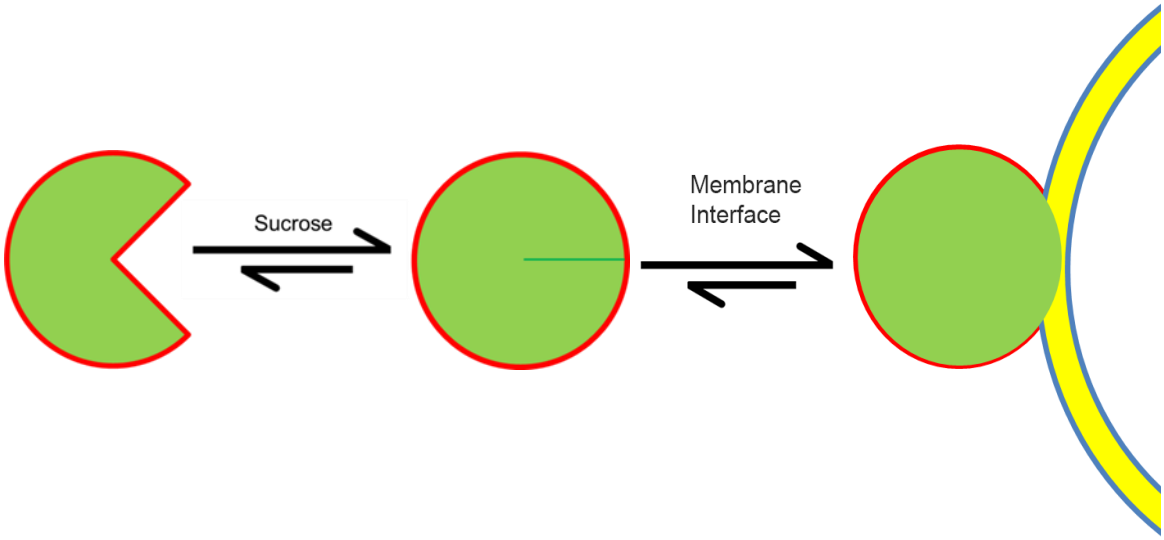


Figure 4.1 Schematic of the effect of preferential exclusion on protein conformation.

Sucrose shifts the protein conformation equilibrium towards a minimal exposed surface area (red). In the presence of interfaces, the protein will adsorb (air/subphase interface) or insert into a leaflet of a lipid membrane interface to further minimize solvent exposed surface area (Anaya, 2013).

## 4.2 Amyloid beta protein

The amyloid beta (Aβ) protein is one of two proteins known to misfold and aggregate in Alzheimer's disease (AD). Aβ is a fragment cleaved from the amyloid precursor protein (APP), an integral membrane protein (Figure 4.2). In the normal, physiological state Aβ takes on an α-helical conformation, while in the diseased state, Aβ takes on a β-sheet conformation. The misfolded proteins then aggregate and form extracellular plaques (Figure 4.2).

Previous studies conducted in our lab have shown that the osmolyte sucrose greatly enhances the interfacial activity of Aβ at an ideal air/subphase interface and in a model membrane system. Our studies here seek to reveal more about the interactions between Aβ protein, lipid monolayers and sucrose on a molecular level.

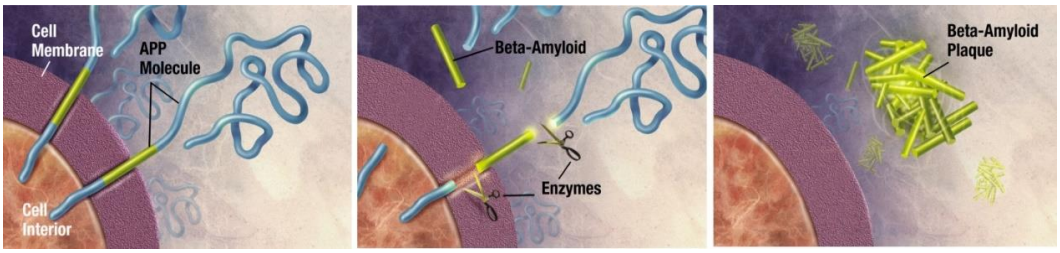


Figure 4.2 Enzyme action on APP crucial to formation of Aβ plaque.

Enzymes act on the APP (Amyloid precursor protein) and cut it into fragments of protein, one of which is called Aβ and is crucial in the formation of senile plaques in AD (Garrondo, 2008).

### 4.3 Materials and methods

Anionic 1,2-dimyristoyl-sn-glycero-3-[phospho-rac-(1-glycerol)] (DMPG) lipids were purchased from Avanti Polar lipids and used as received. DMPG was dissolved in 10 vol % methanol (MeOH) in chloroform. Lipid stock solutions ranging from 2 to 10 mg/mL were prepared and then diluted to 0.2 or 0.5 mg/mL for spreading solutions. All lipid solutions were stored at −20 °C in glass vials.

For our subphases of varying sucrose concentrations, we used sucrose purchased from VWR and purified water (Milli-Q system, Millipore, Bedford, MA). The Aβ used for all experiments was the 40 amino acid long version (Aβ40) and was synthesized using 9-fluorenylmethoxycarbonyl chemistry on an Applied Biosystems 433A Peptide Synthesizer (Foster City, CA) at the University of Chicago. Our Aβ protein samples were purified as previously described (Anaya, 2013) using high performance liquid chromatography (HPLC).

Langmuir trough experiments were carried out at room temperature (23º C). The troughs were filled with the desired subphase, and then lipids were spread on the top of the subphase. During the insertion experiments, protein was injected underneath the subphase surface.

X-ray scattering experiments were carried out at the BW1 beamline at HASYLAB, DESY (Hamburg, Germany) and at APS/Argonne U. Chicago/CARS. XR data gives information about the out-of-plane (perpendicular to the lipid film) electron density profile of the film averaged over the LE and LC phases. GIXD measurements give structural information on the in-plane (*i.e.*, in the plane of the monolayer) ordered (hence diffracting)

portion of the film. The presence of Bragg peaks in GIXD data indicates 2D ordered structures. The theory of XR and GIXD has been presented in detail elsewhere (Jens Als-Nielsen et al., 1994; J. Als-Nielsen & Kjaer, 1989).

## 4.4 Results

### 4.4.1 *GIXD measurements of DMPG monolayers on varying concentrations of sucrose subphase*

We spread DMPG to 14.5 mN/m, compressed to 25 mN/m, and then compressed the same monolayer again to 35 mN/m for all three subphases: 0, 0.1 and 1 M sucrose (Figure 4.3 and 4.4). These π's of 25 mN/m and 35 mN/m were chosen for their relevance to physiological conditions as the lipid packing density of a bilayer is reported to roughly correspond to that of a monolayer at ~30 mN/m (Ege & Lee, 2004; Seelig, 1987). The initial measurements taken at 25 mN/m only showed a Bragg peak for 1 M sucrose subphase (Figure 4.3).

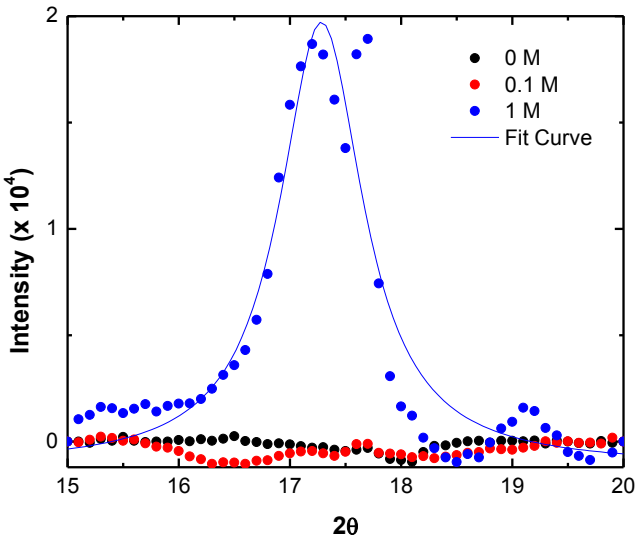


Figure 4.3 Initial GIXD measurements at 25 mN/m.

As illustrated in Figure 4.3, background subtracted intensity of DMPG monolayer at initial 25 mN/m pressure for 0 M (black), 0.1 M (red) and 1 M (blue) sucrose in subphase. A Lorentzian curve (blue line) can be fitted to the 1 M case.

Measurements taken at 35 mN/m (Figure 4.4) displayed Bragg peaks for both the 1 M and 0.1 M cases. There was also a weak signal at a smaller 2θ of ~16.5 which could indicate folded protein. The monolayer on the pure water (0 M sucrose) subphase caused a weak signal in the same angular location of the Bragg peak.

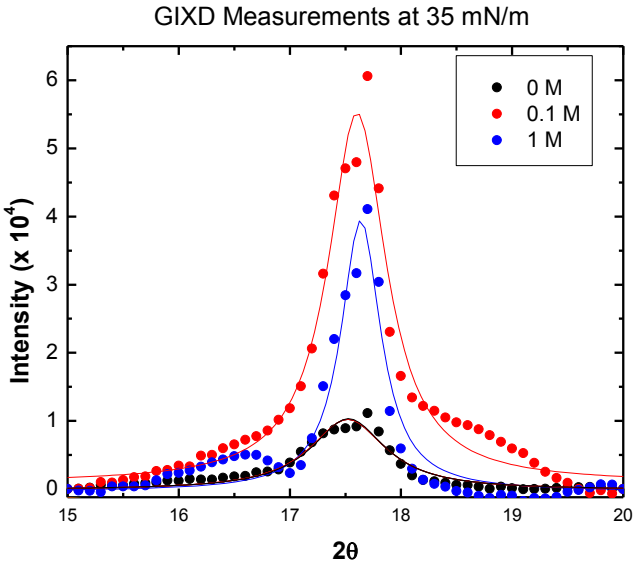


Figure 4.4 Background subtracted intensity of DMPG monolayer at 35 mN/m pressure for 0 M (black), 0.1 M (red) and 1 M (blue) sucrose in subphase.

### 4.4.2 *X-ray scattering measurements of Aβ insertion experiments into 0 M or 1 M sucrose subphases*

We also conducted insertion experiments injecting 500 nM Aβ underneath a DMPG monolayer spread onto a 0 M or 1 M sucrose subphase. For pure water subphase, we had to decrease the pressure, step-wise in increments of 1 mN/m, all the way from 25 mN/m to 14 mN/m before any area expansion was observed. X-ray reflectivity measurements were taken when the pressure of the DMPG monolayer stabilized to 25 mN/m (Figure 4.5) and following insertion of the Aβ protein (Figure 4.6) after decreasing the pressure to 14 mN/m. The distinctive double hump indicates the presence

of an ordered monolayer, while its disappearance indicates disruption of the ordered monolayer occurred after injection of protein.

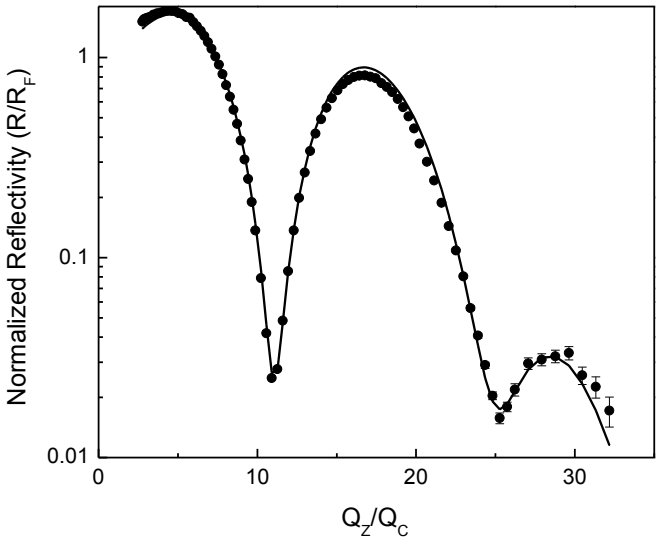


Figure 4.5 $R/R_F$ of DMPG monolayer on water at 25 mN/m and 23 °C.

In Figure 4.5, a model independent fit (solid line) of the XR data was obtained from StochFit which corresponds to the water normalized electron density distribution shown in Figure 4.7.

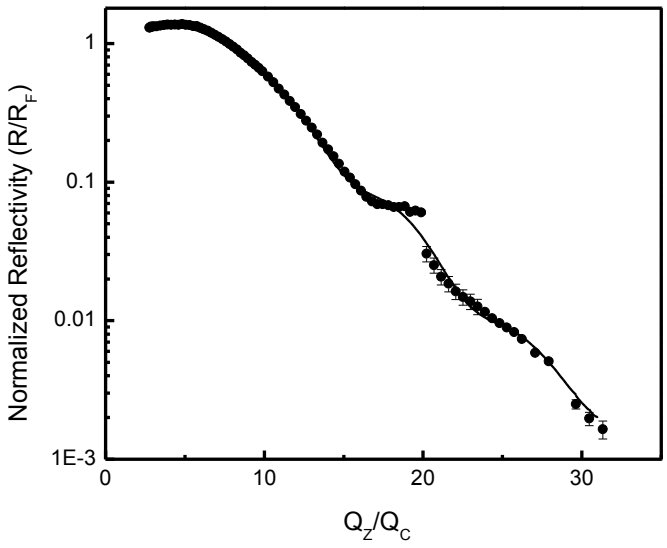


Figure 4.6 Fresnel normalized X- ray reflectivity data of the DMPG monolayer after insertion (at ~14 mN/m rather than 25 mN/m) of 500 nM Aβ on pure water at 23 °C.

In Figure 4.6, a model independent fit (solid line) of the XR data was obtained from StochFit which corresponds to the water normalized electron density distribution shown in Figure 4.7.

Analysis of the XR data before and after injection of protein, performed using the StochFit model (Danauskas et al., 2008), yielded $\rho/\rho_{H2O}$ distribution perpendicular to the air/water interface (Figure 4.7). They indicate the presence of the Aβ protein inside the monolayer after insertion. The black line contains two boxes, one for the headgroups (far left) and one for the tailgroups (far right) of the DMPG lipid. After Aβ insertion, the box on the left increases both in width and electron density, indicating the presence of more material in that location, such as the protein. The headgroup box decreases in electron

density as the lower density protein is included. There is also a slim amount of electron density to the right of the lipid, indicating a buildup of protein at the water-lipid interface.

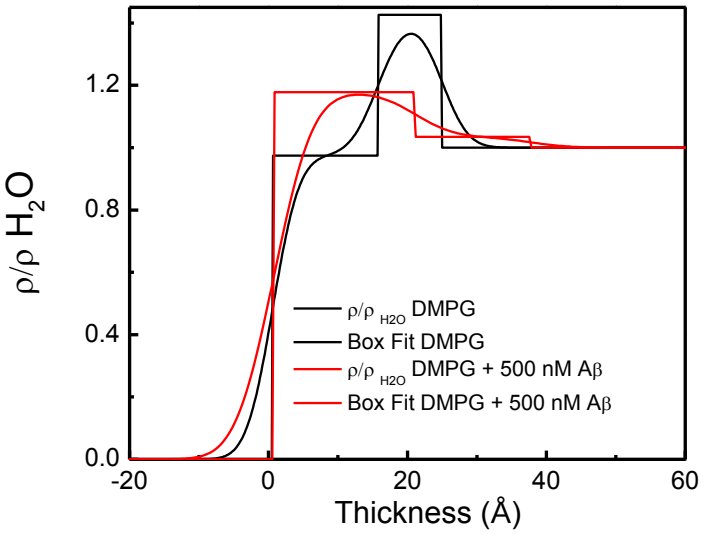


Figure 4.7 Electron densities and box fits of both DMPG on water (black) and DMPG + Aβ on water (red). Box model fits of the electron density profiles are also shown.

For the following experiments using a 1 M sucrose subphase, after injection of the protein we saw an immediate increase in area. The area increased so rapidly, in fact, that the feedback loop used on the trough to maintain a constant pressure was overloaded, and we initially saw a sharp spike in pressure before the trough corrected itself. The area then continually increased until the barrier was completely expanded.

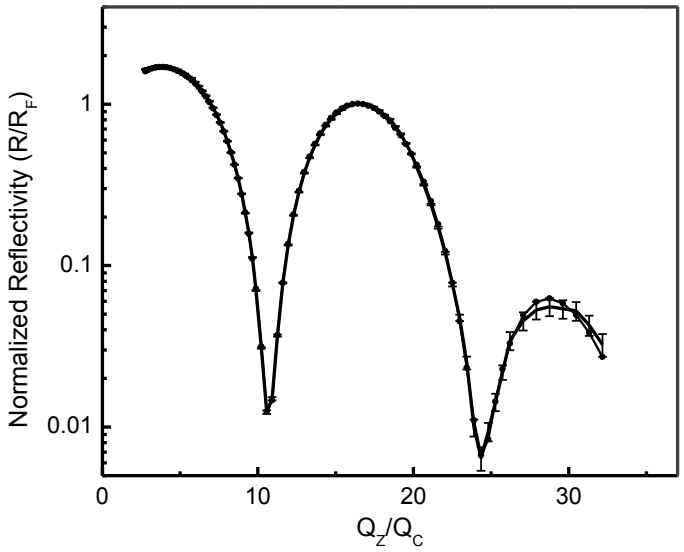


Figure 4.8 Fresnel normalized X-ray reflectivity of DMPG monolayer at 23 °C on a 1 M sucrose subphase.

In Figure 4.8, a model independent fit (solid line) of the XR data was obtained from StochFit which corresponds to the water normalized electron density distribution shown in Figure 4.10.

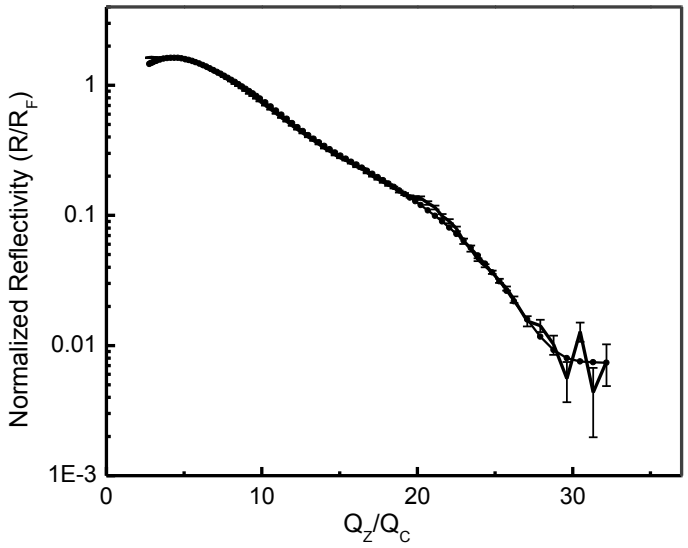


Figure 4.9 Fresnel normalized X- ray reflectivity data of the DMPG monolayer on 1 M sucrose subphase after insertion (at 25 mN/m) of 500 nM Aβ at 23 °C.

In Figure 4.9, a model independent fit (solid line) of the XR data was obtained from StochFit which corresponds to the water normalized electron density distribution shown in Figure 4.10.

The X-ray reflectivity data taken from the 1 M sucrose subphase case once again shows complete disruption of the monolayer on a molecular level, and in this instance did not require any lowering of the pressure for the protein to insert (Figure 4.8 and 4.9). The shifts in the boxfit model of ED again indicate the presence of the Aβ protein inside the monolayer after insertion, but in this case while maintaining a pressure of 25 mN/m. After

Aβ insertion, the box on the left increases both in width and electron density, indicating the presence of more material in that location, such as the protein. The headgroup box decreases significantly in electron density as the lower density protein is included. There is also, again, a small amount of electron density to the right of the lipid, indicating a buildup of protein at the water-lipid interface.

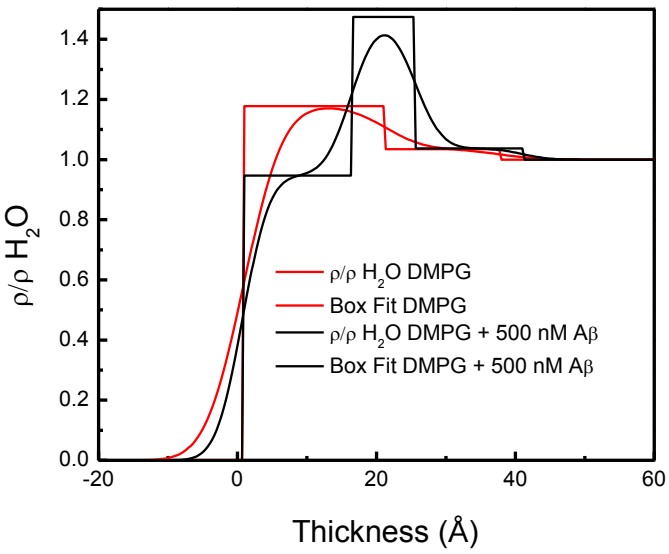


Figure 4.10 Electron densities and box fits of both DMPG on 1 M sucrose subphase (black) and DMPG + 500 nM Aβ on 1 M sucrose subphase (red).

## 4.5 Discussion

We observed that the DMPG lipid monolayer was more rigid when a higher level of sucrose was present in the subphase. At a higher concentration of sucrose, we observed a Bragg peak which indicated a greater degree of order in the lipid monolayer even at a low surface pressure of 25 mN/m. This same peak was not observed at 25 mN/m in the case of subphases which had 0 or 0.1 M sucrose (Figure 4.3). This data reinforces our lab's previous inference that the presence of sucrose increases the rigidity of lipid membranes (Anaya, 2013). The next experiment, compressing the monolayer to a pressure of 35 mN/m, demonstrated that at this higher pressure, Bragg peaks (and, thus, a greater degree of order) were observed in the subphases containing sucrose (Figure 4.4).

Subsequent experiments utilizing 0 and 1 M sucrose subphases with a DMPG monolayer demonstrated that while surface pressure had to be decreased for a DMPG monolayer on pure water before insertion was observed, insertion was instantaneous for the case where the subphase contained 1 M sucrose. This data is consistent with previous data from our lab which observed that sucrose enhanced the adsorption of Aβ to the air/subphase interface. Simultaneous X-ray scattering experiments revealed that the order of the monolayers was disturbed on a molecular level upon insertion of the Aβ protein. We also observed that even though the order of the DMPG monolayer increased with high sucrose concentration, the protein insertion increased as well.

## 4.6 Conclusions

The results of this study shed new light on interactions between the Aβ protein, lipid membranes, and protective osmolytes, but can also be more widely applicable. In the

presence of a protective osmolyte such as sucrose, anionic lipid monolayers are much more rigid. However, amyloid proteins such as Aβ insert even at higher monolayer pressures. This contradicts earlier findings with tau that protein insertion is less likely to occur at high pressures when a lipid monolayer is more ordered. We believe that because of the preferential exclusion of sucrose from the protein surface, the Aβ inserts into the membrane interface more readily in order to decrease the surface area exposed to a subphase with a high sucrose concentration.

### 4.7 References


Als-Nielsen, J., Jacquemain, D., Kjaer, K., Leveiller, F., Lahav, M., & Leiserowitz, L. (1994). Principles and applications of grazing incidence X-ray and neutron scattering from ordered molecular monolayers at the air-water interface. *Physics Reports, 246*(5), 251-313.

Als-Nielsen, J., & Kjaer, K. (1989 April 4 - April 14, 1989). *X-ray reflectivity and diffraction studies of liquid surfaces and surfactant monolayers.* Paper presented at the proceedings of the NATO Advanced Study Institute, Phase transitions in soft condensed Matter, Geilo, Norway.

Anaya, J. (2013). *Effects of Osmolytes Amyloid-beta Protein Surface Activity and Membrane Interaction.* University of New Mexico, Albuquerque.

Arakawa, T., & Timasheff, S. N. (1985). The stabilization of proteins by osmolytes. *Biophys J, 47*(3), 411-414.

Bolen, D. W. (2001). Protein stabilization by naturally occurring osmolytes. *Methods Mol Biol, 168*, 17-36.

Danauskas, S. M., Li, D., Meron, M., Lin, B., & Lee, K. Y. C. (2008). Stochastic fitting of specular X-ray reflectivity data using StochFit. *Journal of Applied Crystallography, 41*(6), 1187-1193.

Ege, C., & Lee, K. Y. C. (2004). Insertion of Alzheimer's A[beta]40 peptide into lipid monolayers. *Biophysical Journal, 87*(3), 1732-1740.

Garrondo.(2008).Amyloid-plaqueformation.Retrieved http://upload.wikimedia.org/wikipedia/commons/f/fb/Amyloid-plaque_formation-big.jpg

Harries, D., & Rosgen, J. (2008). A practical guide on how osmolytes modulate macromolecular properties. *Methods Cell Biol, 84*, 679-735.

Hochachka, P. W., Rupert, J. L., Goldenberg, L., Gleave, M., & Kozlowski, P. (2002). Going malignant: The hypoxia-cancer connection in the prostate. *Bioessays, 24*(8), 749-757.

Lee, J. C. T., S. N. (1981). The stabilization of proteins by sucrose. *J Biol Chem, 256*, 7193-7201.

Limbourg. (1887). *Pfliiger's Arch 41*(303).

Seelig, A. (1987). Local anesthetics and pressure: A comparison of dibucaine binding to lipid monolayers and bilayers. *Biochimica et Biophysica Acta (BBA) - Biomembranes, 899*(2), 196-204.

Spiro. (1900). *Zeitsch Physiol Chem, 80*(182).

Tanford, C. (1964). Isothermal unfolding of globular proteins in aqueous urea solutions. *Journal of the American Chemical Society, 86*(10), 2050-2059.

Yancey, P. H., Clark, M. E., Hand, S. C., Bowlus, R. D., & Somero, G. N. (1982). Living with water stress: Evolution of osmolyte systems. *Science, 217*(4566), 1214-1222.

# CHAPTER 5 EFFECT OF POLYMER CHAIN LENGTH ON MEMBRANE PERTURBATION ACTIVITY OF CATIONIC PHENYLENE ETHYNYLENE OLIGOMERS AND POLYMERS

(Parts of this chapter have been published in *Langmuir* and appear as Ying Wang, Emmalee M. Jones, Yanli Tang, Eunkyung Ji, Gabriel P. Lopez, Eva Y. Chi, Kirk S. Schanze, and David G. Whitten. 2011. Effect of Polymer Chain Length on Membrane Perturbation Activity of Cationic Phenylene Ethynylene Oligomers and Polymers, *Langmuir*, **21**: 10770-10775)

## Abstract

The biocidal compounds (OPEs and PPEs) examined in this study are cationic only, not amphoteric, but the investigation of their interaction with model membranes was conducted to learn more about possible changes in structure of the inserted compound as well as membrane perturbation ability. We examined changes in OPE and PPE characteristics and also lipid integrity, just as we previously studied the interaction of tau and lipid membranes by looking at changes in the structure of both the protein and the membrane. Studying the biocidal compounds serves as a parallel to the interaction which takes place between tau protein and lipid membranes. Whereas with tau we examined structural changes that manifested in β-sheet formation and general compaction of protein to form aggregate-competent intermediates, when examining the polymers we observed a change in structure that was exhibited in changes in photophysical properties from assays that I performed. We also examined methods of cytotoxicity by observing dye leakage from vesicles composed of various lipids when exposed to the polymers.

## 5.1 Introduction

Developing efficient and low-cost antimicrobial agents has been the focus of significant research efforts during the past decade.(Bryers, 2008; Zasloff, 2002) Significant progress has been made toward understanding the toxicity mechanism of naturally occurring antimicrobial peptides and preparing their synthetic mimics.(Gabriel et al., 2007) The main target of these compounds is believed to be the cell membrane, and importantly, these compounds can differentiate between mammalian and bacterial cell membranes (Brogden, 2005; Gabriel et al., 2007).

Our group has developed a series of poly(phenylene ethynylene)- (PPE-) based cationic conjugated polyelectrolyte (CPE) and oligo(phenylene ethynylene) (OPE) compounds that exhibit remarkable light-activated biocidal activity and moderate killing efficiency in the dark (Tang et al., 2009; Zhao et al., 2006). The light-activated biocidal activity of these compounds has been attributed to their ability to generate singlet $O_2$ after exposure to UV-visible light, and the dark killing activity is linked to their ability to disrupt bacterial cell wells and membranes and subsequently cause the death of the bacteria (Chemburu et al., 2008; Corbitt et al., 2009). As part of our investigation of the structure-function relationship of CPEs and OPEs, a series of CPEs and OPEs with the same backbone but a range of different chain lengths, in terms of numbers of repeat units (n) with n varying from 1 to 49, were synthesized (Figure 5.1). It has been proposed that CPEs and OPEs exert their toxicity by disrupting the bacterial membrane in the dark (Wang et al., 2010), so it is important to gain a fundamental understanding of the interactions of these compounds with lipid membranes. Because significant differences in lipid composition exist between prokaryotic and eukaryotic cell membranes (Graham, 1997), we also

examined the interactions of the CPEs and OPEs with lipid membranes of different compositions. Specifically, the principal phospholipids in mammalian plasma membranes are phosphatidylcholine (PC) and sphingomyelin (SM). High levels of cholesterol are also present in mammalian plasma membranes. In addition, the dominant phospholipids in bacterial cytoplasmic membrane are phosphatidylglycerol (PG), phosphatidylethanolamine (PE), and cardiolipin (Graham & Higgins, 1997). The CPEs and OPEs used in this study were cationic amphiphilic compounds with hydrophilic, positively charged side chains positioned along the rodlike hydrophobic PPE backbone (Figure 5.1). We employed several photophysical techniques to examine the interaction of the CPEs and OPEs with model membrane systems, including fluorescent dye-leakage assays and monolayer insertion assays. Our findings provide insights into the structural basis of the CPEs/OPEs' membrane perturbation ability and will enable the design of more effective antimicrobial agents.

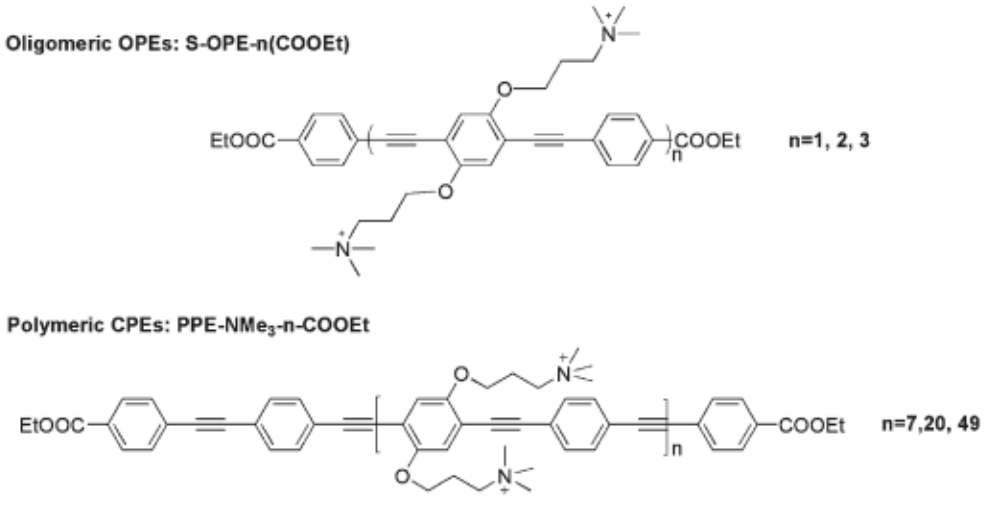


Figure 5.1 Structures of the OPEs [S-OPE-n(COOEt)] and CPEs (PPE-$NMe_3$-n-CooEt) used in this study where n denotes the number of repeat units.

## 5.2 Experimental methods

### 5.2.1 *Materials*

The antimicrobial compounds (Figure 5.1) used in this work were synthesized as reported elsewhere.(Ji et al., 2011; Tang et al., 2011) The concentrations of CPEs used in this study are based on repeat units, and the concentrations of OPEs used in this study are molar concentrations. 1,2-Dipalmitoyl-sn-glycero-3-phospho-(10-rac-glycerol) (sodium salt) (DPPG), 1,2-dihexadecanoyl-sn-glycero-3-phosphoethanolamine (DPPE), 1,2-dioleoyl-sn-glycero-3-phosphocholine (DOPC), *E. coli* total lipid extract, (Phase transition temperatures of the lipids used in this article:DPPG, 41 ºC; DPPE, 63 ºC; DOPC, -20 ºC; *E. coli* total lipid extract, N/A.) cholesterol, and lipid vesicle extrusion supplies were purchased from Avanti Polar Lipids (Alabaster, AL) and used as received. 5(6)-carboxyfluorescein (hereafter referred to as fluorescein) was purchased from Sigma-

Aldrich (St. Louis, MO). Superfine Sephadex G-25 was obtained from GE Healthcare Bio-Science (Piscataway, NJ). All other chemicals were purchased from Sigma-Aldrich. Ultrapure water was used throughout the study (Milli-Q, 18.2 MΩ $cm^{-1}$ resistivity).

### 5.2.2 *Photophysical measurements*

The large unilamellar vesicles (LUVs) were made in pure water by an extrusion procedure (Wang et al., 2010). Briefly, lipids dissolved in organic solvent were dried to form a lipid film. The dry lipid film was hydrated with pure water, subjected to four freeze-thaw cycles, and finally extruded with a 100-nm pore-size polycarbonate membrane. The hydrodynamic radii ($R_h$) of the vesicles were determined by dynamic light scattering (DLS,DAWNHELEOS II, Wyatt Technology Corporation, Santa Barbara, CA) (Ding et al., 2009). The vesicle and CPE/OPE mixtures were prepared in pure water and kept at a lipid-to-CPE/-OPE molar ratio of 50:1. The final lipid concentration was

0.2 mM. To assess changes in the compounds' conjugation lengths, absorbance spectra were measured using a microplate reader (SpectroMax M-5 microplate reader, Molecular Devices, Sunnyvale, CA). To assess changes in the hydrophobicity of the compounds' microenvironments, emission spectra were recorded with a spectrofluorometer (QuantaMaster 50 spectrofluorometer, Photon Technology International, Birmingham, NJ).

### 5.2.3 *Preparation of fluorescein-loaded vesicles and vesicle leakage assays*

Fluorescein-loaded LUVs were prepared by extrusion as previously described (Wang et al., 2010). A dry lipid thin film was first hydrated with 100 mM fluorescein in

water at pH 7 adjusted with NaOH) and then subjected to four freeze-thaw cycles and extrusion. Free fluorescein was removed from the dye-loaded vesicles by column filtration (Sephadex G-25 superfine). The mobile phase used was 200 mM NaCl containing 10 mM 2-[4-(2-hydroxyethyl)-1-piperazinyl]ethanesulfonic acid (HEPES) at pH 7 (buffer A). After separation, the phospholipid concentrations of the dye-loaded vesicle solutions were determined by the modified microprocedure of Bartlett (Bartlett, 1959). The hydrodynamic radii of the vesicles were determined as described above. Stability of the vesicle in the presence of a CPE or an OPE was evaluated by the dye-leakage assay at room temperature. As the vesicle membrane was perturbed by the CPE or OPE, dye was released, and the fluorescence emission intensity of the released dye was recorded at 520 nm (excitation at 485 nm) (SpectroMax M-5 microplate reader, Molecular Devices, Sunnyvale, CA). The CPEs and OPEs are not excited at this wavelength. Fluorescein leakage fractions were calculated as reported previously (Wang et al., 2010). The maximum fluorescence intensity was determined by adding 1 μL of 0.5 M Triton-X100 solution to a 100-μL sample to cause complete lysis of the vesicles, and this intensity was set as 1 in Figure 5.2 and 5.3 (below). All experiments were repeated at least twice, and the trends were highly reproducible.

### 5.2.4 *Lipid monolayer insertion assays*

Insertion of a CPE or an OPE into a lipid monolayer held at a constant surface pressure (Ding et al., 2009) was measured using a Teflon Langmuir trough equipped with a Wilhelmy plate and two identical mobile Delrin barriers (MicroMini Trough System, KSV Instruments Ltd., Espoo, Finland) (Ding et al., 2009). The water subphase volume was 50 mL, and the maximum working surface area was 100 $cm^2$.

Phospholipids dissolved in a 7:3 chloroform/methanol mixture were first spread at the air-water interface. The deposited lipids were left undisturbed for 15 minutes to allow the complete evaporation of the organic solvent. The lipids were then compressed to a target surface pressure ($\pi$) of 30 mN/m, a bilayer equivalent pressure (Seelig, 1987) and the surface pressure was kept constant through a feedback loop. An aliquot of CPE or OPE was then injected into the water subphase using a microsyringe without disturbing the monolayer. The final concentration of CPE or OPE in the subphase was 0.1μM. All experiments were carried out at room temperature. Favorable interactions between the CPEs/OPEs and phospholipids that led to the insertion of the compound into the lipid monolayer caused an expansion of the lipid monolayer surface area at constant pressure. The percentage surface area increase was calculated using the equation

$$\text{area increase } (\%) = \frac{A - A_0}{A_0} \times 100\%$$

where $A_0$ is the trough area before the injection of CPE/OPE and A is the trough area at time t after the addition of the CPE or OPE.

**5.3 Results and discussion**

Over the past decade, new synthetic amphiphilic antimicrobial agents with tunable structures have been reported (Rennie et al., 2005; Som & Tew, 2008)

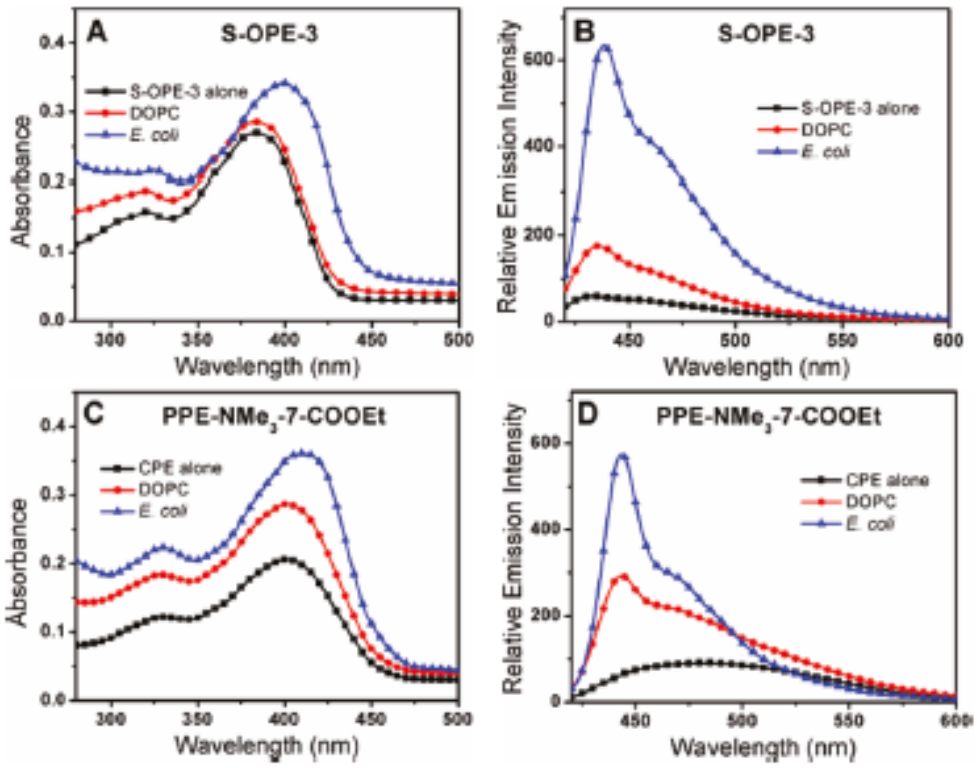


Figure 5.2 (A,C) Absorbance and (B,D) fluorescence emission spectra

Figure 5.2 shows spectra from oligomeric S-OPE-3(COOEt) and polymeric PPE-$NMe_3$-7-COOEt and their mixtures with different lipid vesicles in water at room temperature. The excitation wavelengths for S-OPE-3(COOEt) and PPE-$NMe_3$-7-COOEt are 383 and 401 nm, respectively.

One of the most remarkable features of these synthetic compounds is their high toxicity to bacterial cells and low hemolytic activity against human red blood cells. In addition, the antimicrobial ability of these molecules is related to their insertion or perturbation ability against bacterial cell walls and membranes. Herein, photophysical investigations, dye-leakage assays, and monolayer insertion assays were used to explore

the membrane perturbation abilities of a series of CPEs and OPEs that differ in their numbers of repeat units.

### 5.3.1 *Photophysical investigation*

Because the photophysical properties of CPEs and OPEs are highly dependent on their solution microenvironment (Tang et al., 2009; Zhao et al., 2006) a set of photophysical measurements was obtained to elucidate the changes of the microenvironments of the CPEs and OPEs upon coming into contact with lipid vesicles composed of either DOPC lipids (a mammalian cell membrane mimic) or *E. coli* total lipid extract (a bacterial cell membrane mimic). We previously showed that, in aqueous solutions, the OPEs are monomeric in the μM range (Ji et al., 2011). In contrast, the CPEs readily aggregate in aqueous solutions through intra- or interchain stacking of the conjugated backbone, and this type of aggregation dramatically decreases the fluorescence emission intensity of the CPEs compared to that of the OPEs (Zhao et al., 2006). Thus, the fluorescence emission intensities of the compounds were measured to probe changes in the aggregation state of the compounds in the presence of different lipid vesicles. Absorbance measurements were made to probe changes in conjugation length, or segment chromophores (Tang et al., 2011) of the compounds, whereby red shifts indicate increases of the conjugation length in the molecular backbone.

All investigated CPEs and OPEs were found to exhibit similar spectral changes, including absorbance spectral shifts and increases in emission intensity, upon incubation with the two types of vesicles; Figure 5.2 shows a set of representative absorbance and emission spectra for oligomeric S-OPE-3 and polymeric PPENMe$_3$-7-COOEt alone or

incubated with the two different vesicles. As shown, the absorbance maxima of both OPEs and CPEs underwent red shifts to different extents, with the *E. coli* total lipids inducing the largest changes (Figure 5.2A,C). The emission intensity of the OPEs and CPEs increased significantly in the presence of lipid vesicles, and the *E. coli* total lipids again induced the largest increases.

Parameters obtained from the photophysical characterizations of the CPE and OPE compounds are summarized in Table 5.1. Our data show that the maximum absorbance wavelengths of the OPEs in water increased with chain length, whereas the maximum absorbance wavelengths of the CPEs did not exhibit such a trend (Table 5.1). This is probably due to the ability of the long chains of the CPEs, which are longer than the average conjugation length of the segment chromophores (Tang et al., 2011) within the backbone, to form intra- and/or interchain aggregates (Amrutha & Jayakannan, 2008; Okuyama et al., 1984; Traiphol et al., 2010).

As shown in Table 5.1 and Figure 5.2, when the CPEs and OPEs were mixed with different model membranes, their photophysical properties changed dramatically. Specifically, *E. coli* total lipid extract vesicles induced significant red shifts in the absorbance maxima for all of the investigated CPE and OPE compounds, whereas DOPC vesicles induced little or no change. The red shifts could be partly due to segment planarization of the CPEs or OPEs from their interactions with the *E. coli* lipid membrane, thus extending the conjugation length of the CPEs and OPEs along their backbones.(Chen et al., 2000; James et al., 2006; Miteva et al., 2000). Moreover, the addition of lipid vesicles greatly increased the fluorescence emission intensity of both the CPEs and OPEs (Figure 5.2) suggesting that, when exposed to lipid membranes, the microenvironment of CPEs

and OPEs changed from an aqueous to a hydrophobic environment and, consequently, nonradiative processes were significantly reduced (Tang et al., 2009; Zhao et al., 2006). Meanwhile, the lipid vesicles induced blue shifts in the CPEs' emission spectra (Figure 5.2D and Table 5.1), implying that the conformation of the CPEs might have changed from an aggregated state to a more extended state and that this conformational change was facilitated by the lipid membranes (Kaur et al., 2007; Liu et al., 2008; Ngo et al., 2008; Tan et al., 2004). Overall, changes in spectral characteristics induced by the *E. coli* lipid vesicles were significantly larger than those induced by the mammalian-mimicking vesicles, indicating that the interactions of the CPE and OPE compounds with *E. coli* lipid vesicles were stronger and more extensive than those with the mammalian membrane mimic.

Table 5.1 Photophysical Characterization of the CPEs and OPEs in Different Solutions at Room Temperature

| | maximum absorbance wavelength[b] (nm) | | | maximum emission wavelength (nm) | | |
|---|---|---|---|---|---|---|
| antimicrobial agent | $H_2O$ | *E. coli* | DOPC | $H_2O$ | *E. coli* | DOPC |
| S-OPE-1(COOEt) | 359 | 370 | 360 | 433 | 436 | 434 |
| S-OPE-2(COOEt) | 377 | 395 | 379 | 437 | 436 | 434 |
| S-OPE-3(COOEt) | 383 | 399 | 383 | 431 | 436 | 436 |
| PPE-$NMe_3$-7-COOEt | 401 | 409 | 401 | 484[c] | 443 | 443 |
| PPE-$NMe_3$-20-COOEt | 404 | 415 | 406 | 479[c] | 444 | 445 |
| PPE-$NMe_3$-49-COOEt | 404 | 415 | 406 | 486[c] | 443 | 443 |

[a] DOPC and *E. coli* total lipid concentrations were 0.2 mM and 0.2 mg/mL, respectively. Lipid-to-CPE or -OPE ratio was 50:1. [b] Maximum absorbance wavelength of each compound in water selected as the excitation wavelength for all corresponding emission spectra. [c] Emission spectra of the CPEs in water were broad and flat.

Table 5.2 Vesicle Abbreviations and Their Corresponding Compositions, Sizes, and Overall Charges

| vesides | lipid composition | hydrodynamic radius (nm) | net surface charge |
|---|---|---|---|
| V-1 | 67:33 DOPC/cholesterol | 56 ± 5 | neutral |
| V-2 | *E. coli* total lipid | 61 ± 2 | negative |

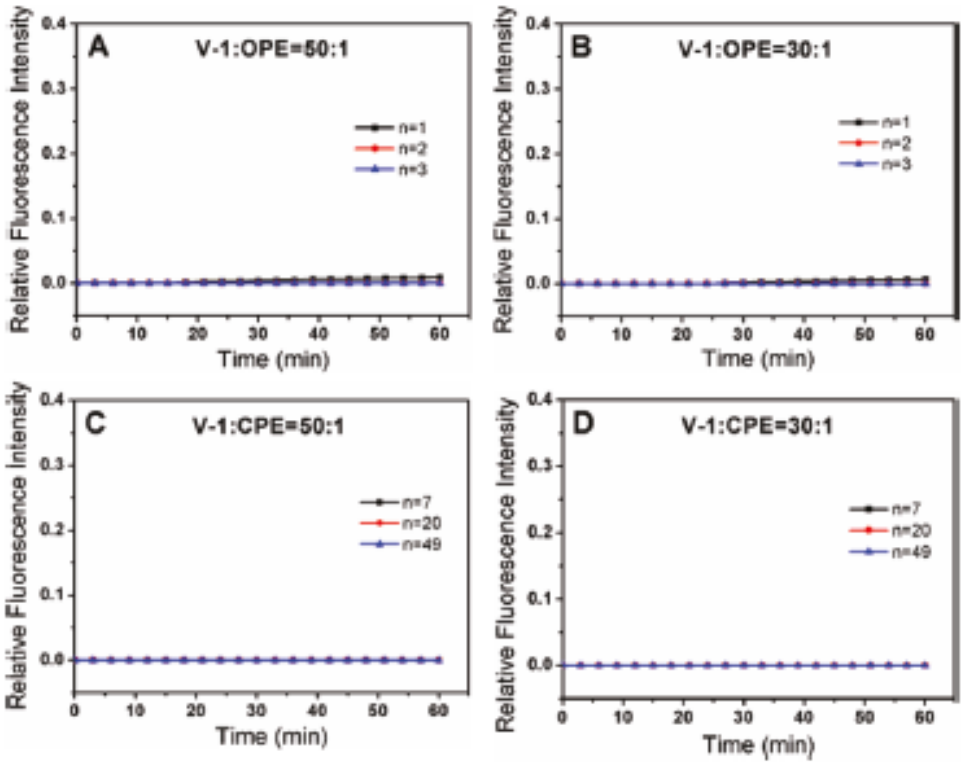


Figure 5.3 Fluorescein leakage profiles

In Figure 5.3 fluorescein leakage profiles from DOPC/cholesterol (67:33) vesicles (V-1) with the addition of a CPE or an OPE in buffer A at room temperature (excitation/emission wavelengths: 485/520 nm). Fluorescence from vesicles incubated alone was subtracted.

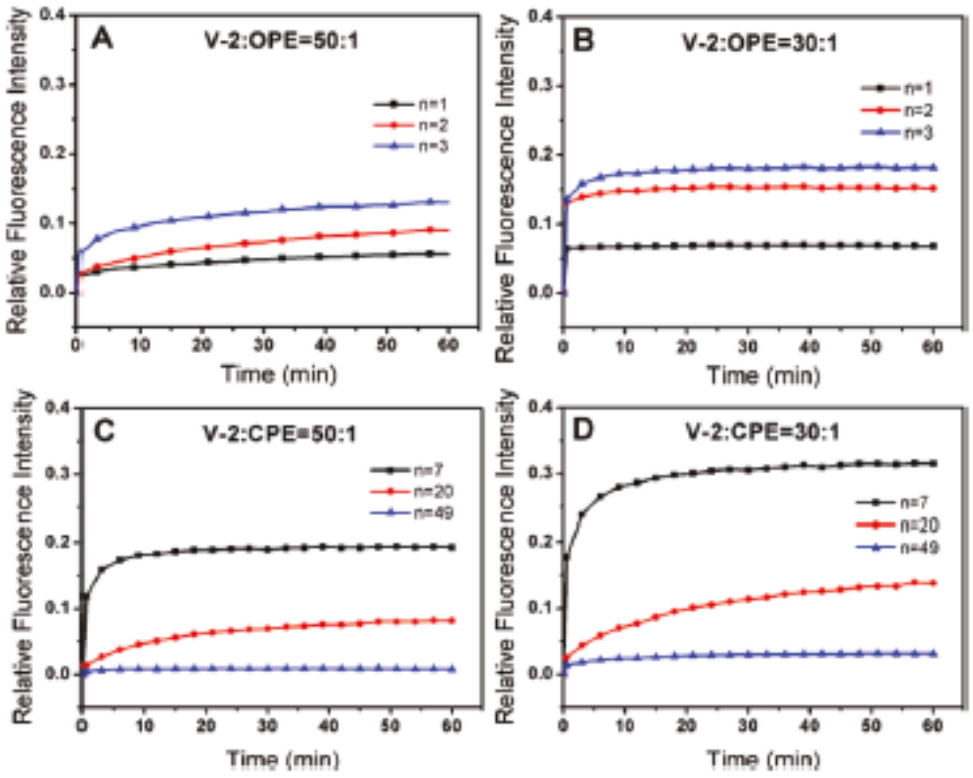


Figure 5.4 Fluorescein leakage profiles

In Figure 5.4 fluorescein leakage profiles from *E. coli* total lipid vesicles (V-2) with the addition of a CPE or an OPE in buffer A at room temperature (excitation/emission wavelengths: 485/520 nm). Fluorescence from vesicles incubated alone was subtracted.

Our results indicate that the amphiphilic CPEs and OPEs bind to lipid vesicles readily and that, upon binding, properties such as the conjugation length and aggregation state of the compounds change. The binding of the CPEs and OPEs to the lipid vesicles was further confirmed by increases in $R_h$ values of the vesicles after the addition of a CPE or an OPE to the vesicles; for example, $R_h$ of *E. coli* vesicles increased from 67 ± 3 nm to 75 ± 2 and 91 ± 3 nm upon the addition of S-OPE-2(COOEt) and PPENME3-20-COOEt, respectively. The binding of the antimicrobial agents to vesicles has been shown to be driven in part by electrostatic interactions. Favorable entropy increases by the release of interfacial water through the binding of CPE or OPE to membranes might also contribute to their high affinity toward membranes (Chen et al., 2000).

### 5.3.2 *Disruption of mammalian- and bacterial-membrane-mimicking vesicles.*

Vesicles of two different lipid compositions were prepared to mimic mammalian and bacterial cell membranes (Graham, 1997) (Table 5.2). V-1, composed of PC lipids and cholesterol, was used as a model for mammalian cell membranes. Figure 5.3 shows the fluorescein leakage profiles from V-1 vesicles incubated with the different CPEs and OPEs. In all cases, no dye release in excess of that of vesicles incubated alone was observed during the incubation period. Clearly, the antimicrobial molecules in the concentration range tested are inactive at disrupting the mammalian membrane mimic.

The binding of the antimicrobial agents to vesicles has been shown to be driven in part by electrostatic interactions. Favorable entropy increases by the release of interfacial water through the binding of CPE or OPE to membranes might also contribute to their high affinity toward membranes (Chen et al., 2000). Vesicles V-2, made from *E. coli* total lipid

extract, were used as a model for the bacterial membrane. As shown in Figure 5.4, all CPEs and OPEs tested induced dye leakage, indicative of membrane disruption against V-2 vesicles. Moreover, the extent of dye leakage was highly dependent on the molecular size and concentration of OPEs and CPEs (Figure 5.4). Increasing the chain length of the oligomers enhanced their membrane perturbation activity (Figure 5.4A, B). In contrast, the polymers showed the opposite trend: increasing the number of repeat units decreased the polymers' membrane perturbation ability (Figure 5.4C, D). The results from dye-leakage assays show that the CPEs and OPEs selectively perturb the bacterial membranes and that the membrane disruption ability is highly dependent on chain length. For the oligomers tested, increasing the chain length enhanced their ability to incorporate or perturb lipid membranes, which led to the leakage of dye molecules from inside the vesicles to the bulk phase. In contrast, increasing the chain length of polymers reduced their membrane perturbation ability, probably by enhancing their tendency to form aggregates through intra- and/or interchain stacking. As a result, the effective concentration of the polymers that could interact with the lipid vesicles was reduced. Additionally, formation of aggregates can also reduce the polymer's cooperativity in inducing membrane surface defects, which might proceed by a highly synergistic mechanism (Bechinger & Lohner, 2006; Orioni et al., 2009).

### 5.3.3 *Lipid monolayer insertion assays*

Monolayer insertion assays are often used to evaluate the interactions and membrane insertion abilities of naturally occurring antimicrobial peptides and synthetic biocidal agents (Ding et al., 2010; Ege & Lee, 2004). In the current study, insertion assays

of CPEs and OPEs into lipid monolayers at the air/water interface composed of DPPG and DPPE were carried out at constant surface pressure to evaluate the effect of chain length on membrane insertion ability. DPPE is zwitterionic and was used instead of DOPC for insertion assays because DPPE forms a more stable monolayer. Moreover, because DPPE and DPPG monolayers are both in the lipid-condensed phase under the experimental conditions, whereas DOPC would be in a liquid expanded phase, the effect of membrane fluidity or lipid packing will have minimal influence on the insertion results.

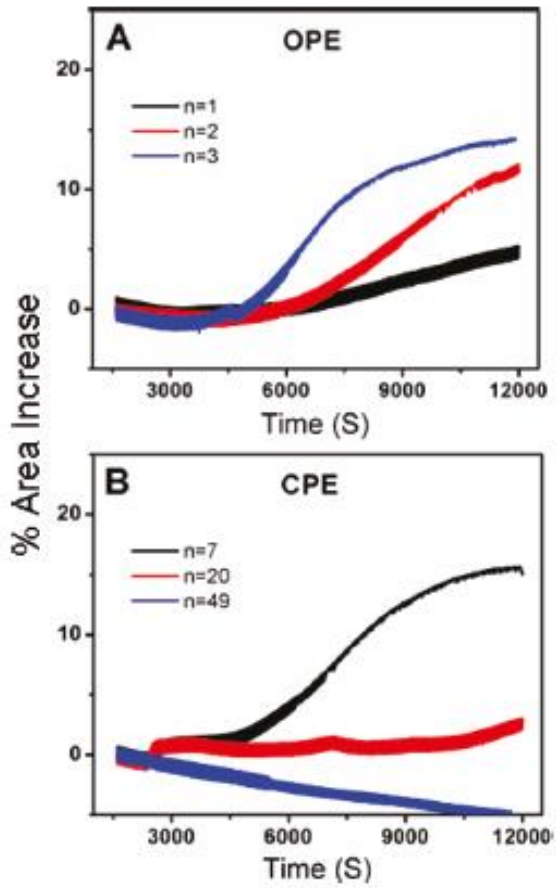


Figure 5.5 Insertion profiles of CPEs (0.1 μM) or OPEs (0.1 μM) into DPPG monolayers held at 30 mN/m on water at room temperature.

Figure 5.5 shows insertion isotherms of the CPEs and OPEs into DPPG monolayers held at 30 mN/m on water at room temperature. Note that CPEs and OPEs alone did not give rise to any surface pressure at the air/water interface (data not shown). The insertion results shown in Figure 5.5 are thus due to favorable interactions between DPPG monolayer and the CPEs or OPEs. Consistent with the results obtained from dye-leakage

assays, the CPEs and OPEs show repeat-unit-dependent monolayer insertion abilities. Specifically, increasing chain length increased the extent of insertion of OPE oligomers, whereas the opposite trend was observed for CPEs. The longest CPE, PPE-NMe3-49-COOEt, did not insert into the DPPG monolayer at 0.1μM. However, increasing the concentration to 0.5 μM resulted in extensive insertion (data not shown). In contrast, none of the CPEs or OPEs tested inserted into the lipid monolayers composed of the zwitterionic DPPE lipids (data not shown). Taken together, the results obtained from lipid monolayer insertion assays provide additional evidence for the size-dependent membrane perturbation ability of CPEs and OPEs and their selectivity toward negatively charged membranes.

### 5.4 Conclusions

Our study clearly demonstrates that cationic CPEs and OPEs exhibit affinity toward both mammalian- and bacterial-mimicking lipid membranes and that they selectively perturb bacterial model membranes. The dye-leakage assays reveal that all of the CPEs and OPEs investigated are inactive against model mammalian membranes in the concentration ranges tested. However, they show significant membrane perturbation activity against model bacterial membranes, and they readily insert into negatively charged lipid monolayers at the air/water interface. Moreover, the compounds exhibit chain-length-dependent membrane perturbation abilities, whereby increasing chain length increases the ability of the oligomers to incorporate into and perturb membranes, and the reverse trend was observed for the polymers. Taken together, these results indicate that there might be an optimum chain length for these PPE-based antimicrobial compounds that corresponds to the highest membrane perturbation efficiency. The results of the current study will serve

as a guide to design more efficient and nontoxic materials resistant to bacteria growth and biofilm formation.

Author Information

Corresponding Authors

*E-mail:Whitten@unm.edu (D.G.W.), evachi@unm.edu (E.Y.C.).

**Acknowledgment**

This research was financially supported by the Defense Threat Reduction Agency (Contract W911NF07-1-0079).

**5.5 References**

Amrutha, S. R., & Jayakannan, M. (2008). Probing the pi-stacking induced molecular aggregation in pi-conjugated polymers, oligomers, and their blends of p-phenylenevinylenes. *J Phys Chem B, 112*(4), 1119-1129.

Bartlett, G. R. (1959). Phosphorus assay in column chromatography. *J Biol Chem, 234*(3), 466-468.

Bechinger, B., & Lohner, K. (2006). Detergent-like actions of linear amphipathic cationic antimicrobial peptides. *Biochim Biophys Acta, 1758*(9), 1529-1539.

Brogden, K. A. (2005). Antimicrobial peptides: Pore formers or metabolic inhibitors in bacteria? *Nat Rev Microbiol, 3*(3), 238-250.

Bryers, J. D. (2008). Medical biofilms. *Biotechnol Bioeng, 100*(1), 1-18.

Chemburu, S., Corbitt, T. S., Ista, L. K., Ji, E., Fulghum, J., Lopez, G. P., et al. (2008). Light-Induced biocidal action of conjugated polyelectrolytes supported on colloids. *Langmuir, 24*(19), 11053-11062.

Chen, L., Xu, S., McBranch, D., & Whitten, D. (2000). Tuning the properties of conjugated polyelectrolytes through surfactant complexation. *Journal of the American Chemical Society, 122*(38), 9302-9303.

Corbitt, T. S., Ding, L., Ji, E., Ista, L. K., Ogawa, K., Lopez, G. P., et al. (2009). Light and dark biocidal activity of cationic poly(arylene ethynylene) conjugated polyelectrolytes. *Photochem Photobiol Sci, 8*(7), 998-1005.

Ding, L., Chi, E. Y., Chemburu, S., Ji, E., Schanze, K. S., Lopez, G. P., et al. (2009). Insight into the mechanism of antimicrobial poly(phenylene ethynylene) polyelectrolytes:

interactions with phosphatidylglycerol lipid membranes. *Langmuir, 25*(24), 13742-13751.

Ding, L., Chi, E. Y., Schanze, K. S., Lopez, G. P., & Whitten, D. G. (2010). Insight into the mechanism of antimicrobial conjugated polyelectrolytes: lipid headgroup charge and membrane fluidity effects. *Langmuir, 26*(8), 5544-5550.

Ege, C., & Lee, K. Y. C. (2004). Insertion of Alzheimer's A[beta]40 peptide into lipid monolayers. *Biophysical Journal, 87*(3), 1732-1740.

Gabriel, G. J., Som, A., Madkour, A. E., Eren, T., & Tew, G. N. (2007). Infectious disease: Connecting innate immunity to biocidal polymers. *Mater Sci Eng R Rep, 57*(1-6), 28-64.

Graham, J. M., & Higgins, J. A. (1997). *Membrane analysis*: Bios Scientific Publishers.

James, P. V., Sudeep, P. K., Suresh, C. H., & Thomas, K. G. (2006). Photophysical and theoretical investigations of oligo(p-phenyleneethynylene)s: effect of alkoxy substitution and alkyne-aryl bond rotations. *J Phys Chem A, 110*(13), 4329-4337.

Ji, E., Parthasarathy, A., Corbitt, T. S., Schanze, K. S., & Whitten, D. G. (2011). Antibacterial activity of conjugated polyelectrolytes with variable chain lengths. *Langmuir, 27*(17), 10763-10769.

Kaur, P., Yue, H., Wu, M., Liu, M., Treece, J., Waldeck, D. H., et al. (2007). Solvation and aggregation of polyphenylethynylene based anionic polyelectrolytes in dilute solutions. *J Phys Chem B, 111*(29), 8589-8596.

Liu, Y., Ogawa, K., & Schanze, K. S. (2008). Conjugated polyelectrolyte based real-time fluorescence assay for phospholipase C. *Anal Chem, 80*(1), 150-158.

Miteva, T., Palmer, L., Kloppenburg, L., Neher, D., & Bunz, U. H. F. (2000). Interplay of thermochromicity and liquid crystalline behavior in poly(p-phenyleneethynylene)s: π−πi interactions or planarization of the conjugated backbone? *Macromolecules, 33*(3), 652-654.

Ngo, A. T., Karam, P., Fuller, E., Burger, M., & Cosa, G. (2008). Liposome encapsulation of conjugated polyelectrolytes: toward a liposome beacon. *J Am Chem Soc, 130*(2), 457-459.

Okuyama, K., Hasegawa, T., Ito, M., & Mikami, N. (1984). Electronic spectra of tolan in a supersonic free jet: large-amplitude torsional motion. *The Journal of Physical Chemistry, 88*(9), 1711-1716.

Orioni, B., Bocchinfuso, G., Kim, J. Y., Palleschi, A., Grande, G., Bobone, S., et al. (2009). Membrane perturbation by the antimicrobial peptide PMAP-23: A fluorescence and molecular dynamics study. *Biochim Biophys Acta, 1788*(7), 1523-1533.

Phase transition temperatures of the lipids used in this article:DPPG, 41 ºC; DPPE, 63 ºC; DOPC, -20 ºC; E. coli total lipid extract, N/A.

Rennie, J., Arnt, L., Tang, H., Nusslein, K., & Tew, G. N. (2005). Simple oligomers as antimicrobial peptide mimics. *J Ind Microbiol Biotechnol, 32*(7), 296-300.

Seelig, A. (1987). Local anesthetics and pressure: A comparison of dibucaine binding to lipid monolayers and bilayers. *Biochimica et Biophysica Acta (BBA) - Biomembranes, 899*(2), 196-204.

Som, A., & Tew, G. N. (2008). Influence of lipid composition on membrane activity of antimicrobial phenylene ethynylene oligomers. *J Phys Chem B, 112*(11), 3495-3502.

Tan, C., Atas, E., Muller, J. G., Pinto, M. R., Kleiman, V. D., & Schanze, K. S. (2004). Amplified quenching of a conjugated polyelectrolyte by cyanine dyes. *J Am Chem Soc, 126*(42), 13685-13694.

Tang, Y., Hill, E. H., Zhou, Z., Evans, D. G., Schanze, K. S., & Whitten, D. G. (2011). Synthesis, self-assembly, and photophysical properties of cationic oligo(p-phenyleneethynylene)s. *Langmuir, 27*(8), 4945-4955.

Tang, Y., Zhou, Z., Ogawa, K., Lopez, G. P., Schanze, K. S., & Whitten, D. G. (2009). Synthesis, self-assembly, and photophysical behavior of oligo phenylene ethynylenes: from molecular to supramolecular properties. *Langmuir, 25*(1), 21-25.

Traiphol, R., Potai, R., Charoenthai, N., Srikhirin, T., Kerdcharoen, T., & Osotchan, T. (2010). Effects of chain conformation and chain length on degree of aggregation in assembled particles of conjugated polymer in solvents–nonsolvent: A spectroscopic study. *Journal of Polymer Science Part B: Polymer Physics, 48*(8), 894-904.

Wang, Y., Tang, Y., Zhou, Z., Ji, E., Lopez, G. P., Chi, E. Y., et al. (2010). Membrane perturbation activity of cationic phenylene ethynylene oligomers and polymers: Selectivity against model bacterial and mammalian membranes. *Langmuir, 26*(15), 12509-12514.

Zasloff, M. (2002). Antimicrobial peptides of multicellular organisms. *Nature, 415*(6870), 389-395.

Zhao, X., Pinto, M. R., Hardison, L. M., Mwaura, J., Müller, J., Jiang, H., et al. (2006). Variable band gap poly(arylene ethynylene) conjugated polyelectrolytes. *Macromolecules, 39*(19), 6355-6366.

# CHAPTER 6 X-RAY REFLECTIVITY AND DIFFRACTION STUDIES OF INTERACTION BETWEEN ADHESION/GROWTH-REGULATORY GALECTIN-1 AND DPPE:GM1 LIPID MONOLAYER AT THE AIR/WATER INTERFACE


## Abstract

Another protein and membrane interaction which we examined was between galectin and a lipid membrane containing the ganglioside GM1. We looked at the changes to both the protein and the membrane on a molecular scale using X-ray scattering techniques as a parallel to the experiments we performed using tau protein and lipid membrane. I modeled the X-ray reflectivity data from the insertion experiments to observe where the Gal-1 protein inserted in a 8:2 DPPE:GM1 lipid monolayer. The galectin protein Gal-1 and the lipid membrane itself also undergo structural changes upon the protein's insertion.


## 6.1: Introduction

Cell surface gangliosides are receiving increasing attention as constituents of microdomains within the plasma membrane and as contact sites for carbohydrate receptors (lectins), especially bacterial toxins such as the pentameric lectin part of the cholera toxin (Ctx) (Kopitz, 2009; Ledeen & Wu, 2009; Pontier & Schweisguth, 2012; Wennekes et al., 2009). Recently, the ganglioside GM1, the Ctx binder, has also been identified as physiological counter receptor for members of the family of human galectins, tissue lectins sharing the b-sandwich fold and a sequence signature with a central tryptophan residue (Kaltner & Gabius, 2012; Solis et al., 2014). Functionally, proto-type (homodimeric)

galectin-1 (Gal-1) exerts growth control via GM1 binding on human neuroblastoma (SK-N-MC) cells *in vitro* and on activated T effector cells (Fajka-Boja et al., 2008; Kopitz et al., 2012; Kopitz et al., 2010; Ledeen et al., 2012; Lencer & Saslowsky, 2005; Wang et al., 2009; Wu et al., 2011). As reported for bacterial $Ab_5$ toxins, the ganglioside is involved in rapidly internalizing Gal-1 measured in T leukemic (Jurkat) cells (Fajka-Boja et al., 2008; Lencer & Saslowsky, 2005). However, membrane reactivity between the cholera toxin and the human lectin will not necessarily cause the same post-binding mechanisms: only the human lectin is a growth regulator for the neuroblastoma cells (Kopitz et al., 2012). Obviously, topological aspects of association are different, prompting us to initiate the analysis of galectin binding to a GM1-containing model surface.

In addition to cellular uptake and routing as well as impact on growth, the study of association to the surface of trypsinized erythrocytes has revealed an effect on membrane properties such as fluidity and osmofragility that may depend on a change in quaternary structure of Gal-1 upon entering the hydrophobic environment (Gupta et al., 2006). Of note, in an aprotic solvent the lectin has been demonstrated to form a dimer of the homodimer with a cylindrical shape (He et al., 2003). This evidence directed us to start our study with examining the possibility of an insertion of this potent effector into the lipid monolayer.

## 6.2 Materials and methods

### 6.2.1: *Materials*

1,2-Dihexadecanoyl-*sn*-glycero-3-phosphoethanolamine (DPPE) and ganglioside GM1 (brain, ovine-ammonium salt, powder) were purchased from Avanti Polar Lipids (Alabaster, AL) and used without further purification (Figure 6.1). Stock solutions of each sphingo(glycol)lipid (~5 mg/ml) were first prepared by dissolving the lipid in chloroform containing 9 vol% methanol and 1 vol% water to a concentration of ~ 5 mg/ml. Lipid monolayer spreading solutions (0.3 mg/ml) containing 80 mol% DPPE and 20 mol% GM1 (8:2 DPPE:GM1) were then prepared and stored at -20 °C in glass vials until use. Human Gal-1 was obtained by recombinant production, purified by affinity chromatography as a crucial step and rigorously controlled for purity (by two-dimensional gel electrophoresis and mass-spectrometric fingerprinting) and for bioactivity (by haemagglutination and assays for growth inhibition) (Amano et al., 2012; Andre et al., 2007; Ledeen et al., 2012).

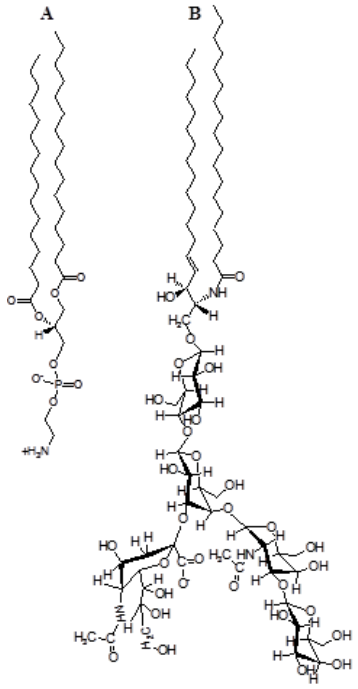


Figure 6.1 Molecular structures of the sphingolipids DPPE (A) and GM1 (B) used.

### 6.2.2: *Constant pressure lipid monolayer insertion assay*

To examine the galectin's interaction with lipid membranes, the insertion of the protein into a mixed DPPG and GM1 lipid monolayer at the air/buffer interface under constant surface pressure was carried out in a Langmuir trough (Chi et al., 2007) at the BW1 (undulator) beam line at the HASYLAB synchrotron source (Hamburg, Germany) ( Majewski et al., 1995). A schematic of the experimental set-up of the constant pressure protein insertion assay carried out in a Langmuir trough is shown in the Supplementary Material, Figure 6.7. The temperature-controlled trough at the dedicated liquid surface diffractometer was equipped with a Wilhelmy plate balance that measures surface pressure at the air/buffer interface and a movable hydrophobic Teflon barrier that controls the trough

surface area. The trough was first filled with approximately 240 mL of subphase buffer (20 mM PBS at pH 7.2 containing 16.2 mM $Na_2HPO_4$, 4 mM $KH_2PO_4$, 154 mM NaCl, and 1% $NaN_3$) at 20 °C. A solution of mixed lipids (8:2 DPPE:GM1 90:9:1 chloroform:methanol:water) was then spread at the air/buffer interface. The system was allowed to equilibrate for 15 minutes to ensure the complete evaporation of the organic solvent, after which the lipid monolayer was compressed to a target surface pressure of 20 mN/m and this pressure was kept constant for the remainder of the experiment *via* a feedback loop (Figure 6.7A). X-ray scattering data (described in more detail below) was then collected on the lipid film at 20 mN/m and 20 °C. Then, an aliquot of Gal-1 (5 mg dissolved in 1 ml PBS buffer) was injected into the buffer subphase of the trough and allowed to equilibrate with the lipid monolayer (Figure 6.7B). The galectin concentration in the trough subphase was approximately 21 μg/ml. Since the lipid monolayer surface pressure was kept constant, insertion of Gal-1 into the lipid monolayer resulted in an expansion of the lipid monolayer surface area (Figure 6.7C). Thus monolayer surface area expansion is taken as a measure of productive protein-membrane interactions. X-ray scattering data were taken 5 ($t_1$) and 13 ($t_2$) hours after injection of Gal-1-containing solution.

### 6.2.3: *X-ray scattering measurements*

To elucidate the molecular-scale structure of the Gal-1 – lipid monolayer film, complementary grazing-incidence X-ray diffraction (GIXD) and X-ray reflectivity (XR) data were collected before (*e.g.*, lipid membrane alone) and two time points after ($t_1$ and $t_2$) placing Gal-1 underneath the 80:20 DPPE:GM1 lipid monolayer. The X-ray

beam that illuminates the sample has a wavelength (λ) of 1.30± 0.02 Å (9510 eV) and a power of *ca*. 0.3 mW. To reduce scattering background and to minimize oxidative X-ray beam damage to the protein-lipid film, the trough container was purged for 30-40 minutes with helium. As an additional precaution against damage by radiation, the trough was translated by 0.025 mm in the horizontal direction after every step during GIXD scans and by 2 mm during XR scans.

GIXD measurements provide in-plane (*i.e.*, in the plane of the monolayer) structural information on the crystalline diffracting portion of the film. In general, the lipid-condensed (LC) phase in Langmuir monolayers can be described as 2D powers with 2D-crystallites that are azimuthally and randomly oriented on the subphase surface. The reciprocal space of GIXD patterns from the crystalline portion of the monolayer arise from a 2D array of *Bragg rods*, which extend parallel to the vertical component, $q_z$, of the scattering vector, $q$ (Als-Nielsen & Kjær, 1990; Kjær, 1994). To maximize surface sensitivity for the GIXD measurements, the monochromatic X-ray beam was adjusted to strike the surface at an incident grazing angle of 0.11°, which is 85% of the critical angle for total external reflection (Eisenberger & Marra, 1981). The dimensions of the footprint of the incoming X-ray beam on the liquid surface were approximately 2x50 $mm^2$. Diffracted intensities were collected using a one-dimensional position-sensitive detector (PSD, OEM-100-M, Braun; Garching, Germany), as a function of the vertical scattering angle and has a measuring window of $\Delta q_z \approx 0.9$ $Å^{-1}$. A Soller collimator was mounted in front of the PSD, which gave the horizontal resolution of the detector of $\Delta q_{xy} = 0.0084$ $Å^{-1}$. The scattered intensity was measured by scanning over a range of the horizontal scattering vector component, $q_{xy} \approx \frac{4\pi}{\lambda}\sin\left(\frac{2\theta_{xy}}{2}\right)$, where $2\theta_{xy}$ is the angle

between the incident and diffracted beam projected onto the horizontal plane, and $\lambda$ is the wavelength of the X-ray beam. Such a scan, integrated over the whole window of the position sensitive detector (PSD), yields the *Bragg peaks*. Simultaneously, the scattered intensity recorded in channels along the PSD, but integrated over the scattering vector in the horizontal plane across a Bragg peak, produces $q_z$-resolved scans called *Bragg rod profiles*. The intensity distribution along a Bragg rod can be analyzed in terms of a model of the molecular conformation, packing and orientation, to yield, *e. g.*, information on the direction and magnitude of the molecular tilt in the crystalline part of the amphiphilic film. In this work, lipid tails were modeled by a cylinder of constant electron distribution. Adjustable parameters, then, were the tilt angle of the cylinder from vertical, the lateral tilt direction, the length, $L_c$, of the cylinder (*i.e.*, the length of the part of the molecule which scatters coherently), and the vertical root-mean-square displacement, $\sigma_z$ (Debye-Waller factor), in the crystallites. Analysis of the *Bragg peaks* yields *d*-spacing and coherence length (*i.e.*, average size) of the 2D crystallites in the film at the air/buffer interface.

While GIXD measurements afford structural information on the in-plane crystalline portion of the film, XR measurements yield information about the out-of-plane (vertical) monolayer structure, laterally averaged over both crystalline and amorphous portions (Als-Nielsen et al., 1994; Jensen & Kjaer, 2001). For XR measurements, an additional slit is used to exclude diffuse scattered background around the reflected beam. This slit, together with a scintillation detector having a thin vertical measuring window

($\Delta q_Z \approx 0.02$ Å$^{-1}$), is mounted on an elevator situated on a diffractometer arm which is pivoted around a vertical axis through the sample center. Detailed information on the electron density variation in the vertical direction, laterally averaged over both the ordered

and disordered parts of the film, can be obtained from the deviation of the measured specular XR from Fresnel's law (Als-Nielsen & Kjær, 1990; Kjær, 1994).

## 6.3 Results

### 6.3.1 *Gal-1 insertion into DPPE:GM1 monolayer*

During the lipid monolayer insertion assay, monolayer surface area was recorded and the percent area expansion ($\%\Delta A / A$) was calculated using the equation $\%\Delta A / A = 100\left(\frac{A - A_i}{A_i}\right)$, where $A_i$ is the trough area of the monolayer at 20 mN/m and 20 °C before the injection of Gal-1-containing solution and $A$ is the trough area at time *t* after applying the protein. The isotherm and insertion data are summarized in Figure 6.2, revealing a productive interaction.

As shown in Figure 6.2B, Gal-1 inserted into the monolayer immediately after starting the experiment by injection into the buffer subphase and steadily continued to do so during the seven hours. The area per molecule shown here reflects the average area per lipid molecule, accounting for both ordered (LC) and disordered (liquid-expanded) phases. Note that the "bilayer-equivalent surface pressure", *i.e.*, the pressure at which monolayer lipid packing density mimics those in a lipid bilayer, has been reported to be in the range of 30-33 mN/m (Seelig, 1987). An insertion assay at a constant surface pressure of 30 mN/m had first been carried out. However, because no lectin insertion into the lipid monolayer was observed at this pressure, the surface pressure was lowered to 20 mN/m for the subsequent experiment, during which protein insertion occurred as reported here.

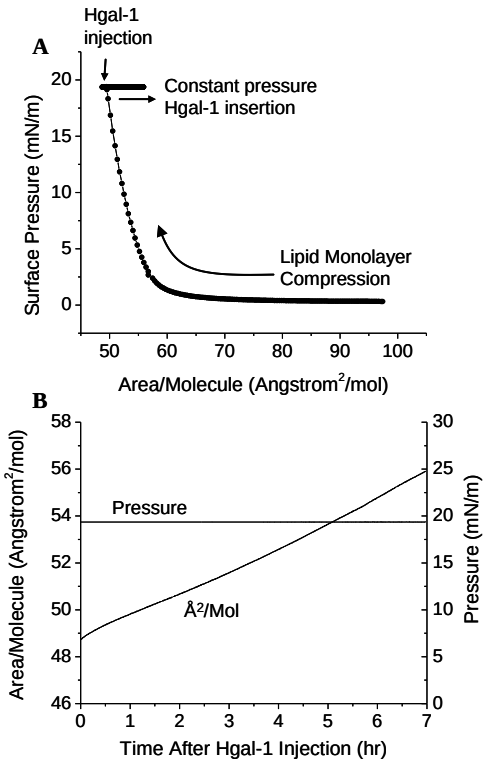


Figure 6.2 Isotherm (A) and insertion (B) of Gal-1 into a 8:2 DPPE:GM1 monolayer held at 20 mN/m at 20 °C.

### 6.3.2 *Structure of the Gal-1 – lipid monolayer film at the air/buffer interface*

By combining the methods of GIXD and XR, the in-plane and out-of-plane structures of the lipid film and location of the lectin at the lipid film interface were elucidated. Figure 6.3 shows a contour plot of the GIXD data for the mixed 8:2 DPPE:GM1 monolayer with both $q_{xy}$ and $q_z$ resolved. Very similarly shaped contour plots for the monolayer after lectin insertion were observed, although absolute intensities of the plots differed (data not shown). Figure 6.4 shows GIXD data projected on the $q_{xy}$ and on $q_z$ axis, yielding *Bragg peaks* and *Bragg rods*, respectively. The time points five ($t_1$) and 13 ($t_2$) hours corresponded to approximately 14% and 20% area expansion of the lipid monolayer. The rate of area

expansion due to lectin insertion was approximately 2%/hr. Note that Gal-1 insertion did not reach equilibrium after 13 hours – a plateau in area/molecule versus time was not observed.

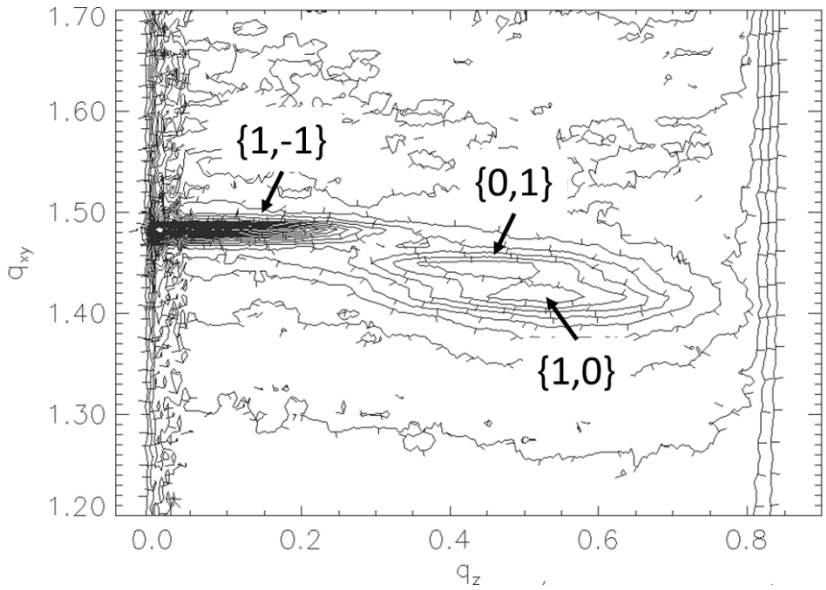


Figure 6.3 Reciprocal space contour plot, , of DPPE:GM1 monolayer at 20 mN/m and 20 °C.

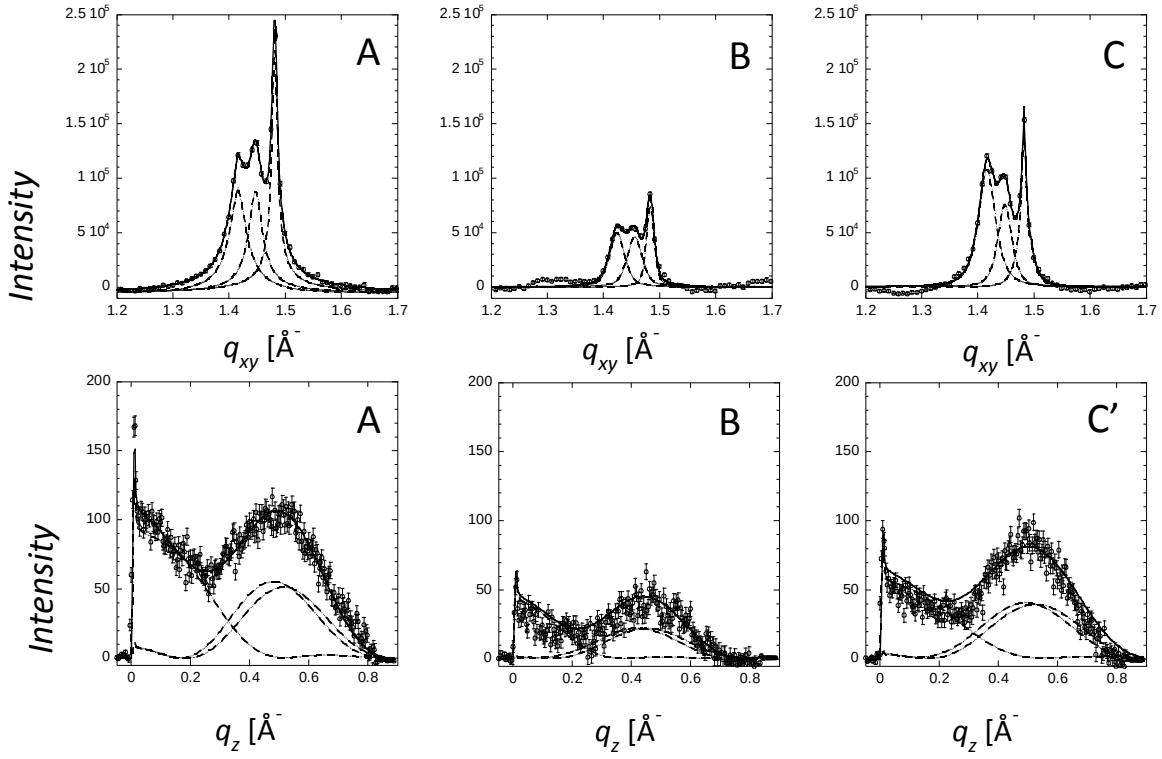


Figure 6.4 The integrated GIXD (*Bragg peaks*) data of the lipid film.

Figure 6.4 illustrates the integrated GIXD (*Bragg peaks*) data of the lipid film before (A), five hours (B) and 13 hours (C) after applying Gal-1. The two time points corresponded to approximately 14% and 20% area expansion of the lipid monolayer. The diffraction pattern was fitted using the sum of three Voigt profiles (solid line) and de-convoluted into separate peaks (dashed lines) corresponding to each of *{1,0}, {0,1}* and *{1,-1}* Bragg peaks. Bragg peaks were obtained by integrating over the (-0.05 Å-1 $\leq q_z \leq$ 0.8 Å-1). (A', B', C') Sum of the three *{1,0}, {0,1}, {1,-1} Bragg rods* corresponding to DPPE:GM1, $t$ = 5hrs and $t$ = 13hrs after injection of Gal-1. By integrating over the

($1.35\ Å^{-1} \leq q_{xy} \leq 1.55\ Å^{-1}$) region, the Bragg rods were fitted (solid line) by approximating the coherently scattering part of the alkyl tail by a cylinder of constant electron density. Each of the separate Bragg rods are shown as dashed lines in the figure.

The diffraction patterns obtained for a DPPE:GM1 monolayer at 20 mN/m and 20 °C before and after applying Gal-1 are shown in Figure 6.3 and Figure 6.4, the resulting structural parameters are summarized in Table 6.1 and Table 6.2. The diffraction obtained for the mixed DPPE-GM1 before Gal-1 injection is similar to previously published data (Miller et al., 2008; Watkins et al., 2011).

For each of the systems measured, three Bragg peaks were observed at $q_{xy} \sim 1.42$, 1.45, and 1.48 $Å^{-1}$. The presence of three Bragg peaks is indicative of an oblique 2D cell. For each of the system the integrated intensities of the three Bragg peaks ($-0.05\ Å^{-1} \leq q_z \leq 0.8\ Å^{-1}$) were approximately the same (see dashed lines in Figure 6.4) in agreement with the multiplicity rule. The three peaks can be indexed as $\{1,0\}$, $\{0,1\}$ and $\{1,-1\}$. The calculated *d*-spacing values (*d-spacing* = $2\pi/q_{xy}$), $d_{10}$, $d_{01}$, and $d_{1\text{-}1}$, give rise to the dimensions and of the unit vectors $|\mathbf{a}|$ , $|\mathbf{b}|$ and the angle between them $\gamma$ for the primitive 2D unit cell, with as well the area per two alkyl chains, are summarized in Table 6.1.

Assuming that the monolayer consists of perfect 2D crystallites of an average dimension $L_{xy}$ (the lateral *coherence length*) in the crystallographic direction $\{h, k\}$ with no preferred azimuthal orientation, the Scherrer formula (Guinier, 1963) can be used to calculate the coherence length in the three crystallographic directions using the equation $L_{xy} \approx 0.9[2\pi/ FWHM_{\text{intrinsic}}(q_{xy})]$ *{h, k}*. As the corresponding full width at half maximum (*FWHM*) of the three peaks exceeds the instrumental resolution of

$FWHM_{resol}(q_{xy})$ = 0.0084Å$^{-1}$, the intrinsic FWHM can be obtained using the equation $FWHM_{intrinsic}(q_{xy}) = [FWHM_{meas}(q_{xy})^2 - FWHM_{resol}(q_{xy})^2]^{1/2}$. From this analysis, the lateral coherence lengths for the three peaks, $L_{10}$ , $L_{01}$, and $L_{1-1}$, were calculated and summarized in Table 6.2. As a reference, a distance of 500 Å encompasses approximately 100 alkyl chains or a crystalline domain 50 lipids across.

The combined *Bragg rod* profile of the *{0,1}*, *{1,0}* and *{1,-1}* reflections, shown in Figure 6.4 A', B', C', was produced by integrating the scattering data through the $1.35\ Å^{-1} \leq q_{xy} \leq 1.55\ Å^{-1}$ region of the three peaks. Analysis of the Bragg rod profiles was done by approximating the lipid alkyl tails as tilted cylinders with constant electron density and length $L_c$ (Als-Nielsen et al., 1994). Results are summarized in Table 6.1. As shown in Figure 6.4, the diffraction patterns from the DPPE:GM1 and DPPE:GM1 + Gal-1 ($t_2$ = 13 hrs) monolayers are similar, indicating that in the ordered phase, they have similar area per lipid molecule (43.5Å$^2$), alkyl tails tilt (~21.45± 0.15° from the surface normal), and azimuthal angle (10.8 ± 0.3° from the nearest neighbor defined by the vector ***a*+*b*).** However, the length of the cylinder with constant electron density used to model the intensity distribution along the Bragg rods, $L_c$, was 18.9 for pure DPPE:GM1 *vs.* 17.3 Å at $t_2$. This suggests that Gal-1 interaction with DPPE:GM1 caused a small (1.5 Å) vertical displacement in the lipid packing. Additionally, at $t_2$ the $L_{1-1}$ coherence length increased from 500 to 760 Å, suggesting improvement in packing of the lipid tails along this crystallographic direction (Table 6.2).

The diffraction from DPPE:GM1 + Gal-1 at $t_1$ = 5 hours is different from the so far presented cases of pure lipids (no protein) or 13 hours after lectin application. Although the length of the cylinder, $L_c$, was the same as in the case of the DPPE:$GM_1$ monolayer

before Gal-1 insertion (18.9 Å), which suggested no out-of-plane lipid displacements, the area per molecule decreased to 43.1 $Å^2$, and alkyl tails tilt and azimuthal angle decreased to 19.4° and 2.6°, respectively. The $L_{1-1}$ coherence length also decreased from 500 to 380 Å, suggesting a reduction in the positional registry between the lipid tails along this crystallographic direction (Table 6.2).

With the insertion of Gal-1, the intensity of the diffraction peaks decreased to about 35% at $t_1$ compared to that of lipids alone, indicating that crystalline order in lipids has been partially disrupted. As indicated, this appeared as transient phenomenon, partial recovery of the amount of ordered phase as the integrated intensities increased to 70% at $t_2$ = 13 hours. Of note, such a result has not been previously observed for the number of protein-membrane systems we have studied to date. Although the cause of this recovery of ordered phase is unclear, it is evident that the initial association of Gal-1 with the LC phase of the lipid membrane was followed by reorganization and/or relaxation of the system such that liquid-condensed phase reformed, *e.g.*, clustering and oligomerization of membrane-associated Gal-1. The increased LC phase with incubation time could also be caused by large-scale heterogeneities, e.g., lipid phases and protein may not have been uniformly distributed in the film. This is rather unlikely since we have never observed such phenomena.

Interestingly, no diffraction signal was observed in the low $q_{xy}$ region (0.05 - 1.0 $Å^{-1}$, 120 Å > *d-spacing* >6 Å) corresponding with higher *d*-spacings of the measured spectra (data not shown). Therefore, we can conclude that neither Gal-1 nor pentasaccharide headgroups of GM1 form regular arrays of sufficient size to be detectable by GIXD.

Table 6.1 Summary of Parameters Obtained from Analysis of GIXD data

| **20 mN/m, 20°C** | | **DPPE:GM1** | **DPPE:GM1 Gal-1 $t_1$ = 5hrs** | **DPPE:GM1 Gal-1 $t_2$ = 13hrs** |
|---|---|---|---|---|
| **Distorted Hexagonal Unit Cell** | **a (Å)** | 4.91 ± 0.01 | 4.89 ± 0.01 | 4.90 ± 0.01 |
| | **b (Å)** | 5.01 ± 0.01 | 5.00 ± 0.01 | 5.01 ± 0.01 |
| | **γ (degrees)** | 117.1 ± 0.4 | 118.0 ± 0.4 | 117.7 ± 0.4 |
| **Area per molecule ($Å^2$)** | | 43.5 ± 0.1 | 43.1 ± 0.1 | 43.5 ± 0.1 |
| **Integrated Intensity (%)** | | 100 | 35 | 70 |
| **Coherence Length, $L_c$ (Å)** | | 18.9 ± 0.5 | 18.9 ± 0.5 | 17.3 ± 0.5 |
| **Tilt Angle $t$ (°)** | | 21.6 ± 1.0 | 19.4 ± 1.0 | 21.3 ± 1.0 |
| **Tilt dir. from NN, non-symmetry (°)** | | 11.1 ± 1.0 | 2.6 ± 2.0 | 10.5 ± 1.0 |
| **$\sigma$ (Å)** | | 0.9 ± 0.2 | 0.94 ± 0.2 | 0.84 ± 0.2 |

$L_c$ is the length of the coherently scattering part of the alkyl tail measured along its backbone. Tilt angle is measured from the surface normal. The tilt angle is measured between direction of nearest neighbor and the projection of the alkyl tail on the subphase

surface. Nearest neighbor (NN) is along $a + b$, where $a$ and $b$ are the 2D unit cell vectors**.** $\sigma$ is the vertical Debye-Waller factor or root mean-square molecular displacement normal to the surface.

Table 6.2 In-plane Coherence Lengths Obtained from GIXD Data

| 20 mN/m, 20ºC | In-Plane Bragg Peaks Coherence Length, $L_{xy}$ (Å) ± 10 Å | | |
|---|---|---|---|
| | $L_{01}$ | $L_{10}$ | $L_{1\text{-}1}$ |
| DPPE:GM1 | 160 | 190 | 500 |
| DPPE:GM1 + Gal-1, $t_1$ = 5hrs | 180 | 180 | 380 |
| DPPE:GM1 + Gal-1, $t_2$ = 13hrs | 160 | 200 | 760 |

Length, $L_{xy}$, is the in-plane coherence length; an average size of the 2-D "crystalline" islands.

Whereas GIXD measurements probe only the crystalline portion of the hydrocarbon chains in the footprint of the X-ray beam, XR provides averaged structural information from both the 2D-crystalline and amorphous parts of the monolayer along the direction perpendicular to the lipid film. The reflectivity data was analyzed using an optical matrix method (StochFit) (Danauskas et al., 2008), assuming that the mixed monolayers formed

homogeneous thin films. This is justified since previous Brewster angle and fluorescent microscopy studies show that the components mix, rather than phase separate (Miller et al., 2008; Watkins et al., 2011). Following the StochFit procedure (Danauskas et al., 2008) the electron density distribution, normalized to that of water, along the subphase surface normal was approximated by a large number slabs, each with a constant electron density, interconnected by error functions. In this model-independent fitting procedure, the electron density of each slab was varied to optimize a mathematical construct to obtain the smooth functional form of the electron density distribution which results in the best fit (lowest $\chi^2$ values) to the measured XR data. Twelve slabs were sufficient to adequately model XR profiles obtained from this study. The top row of Figure 6.5 shows XR data (red circles) along with the best fits (solid and dashed black lines) based on electron density distributions presented in the *bottom row* by color solid lines.

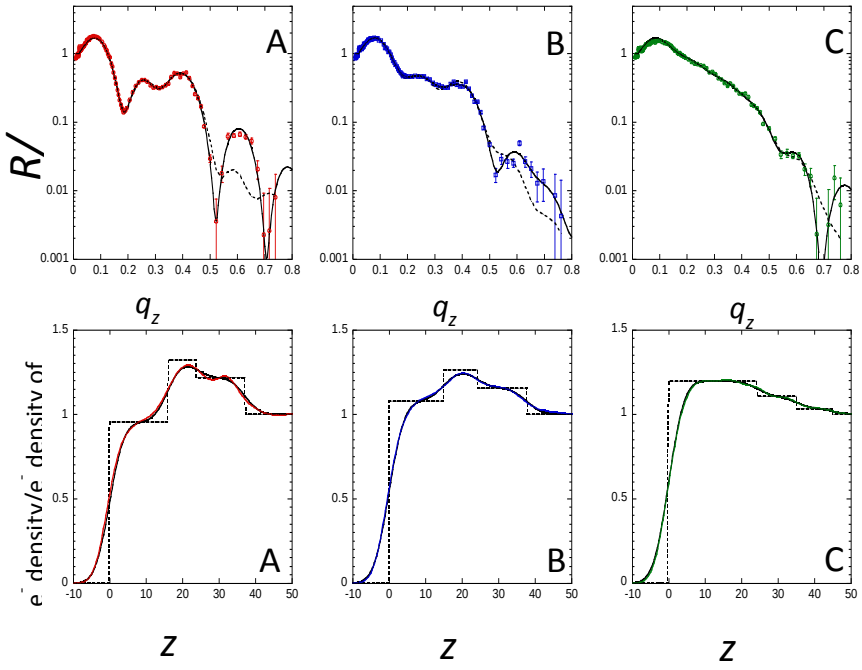


Figure 6.5 Fresnel normalized X-ray reflectivity (top row) and normalized electron density distribution (bottom row) of the DPPE:GM1 lipid films.

Figure 6.5 illustrates Fresnel normalized X-ray reflectivity (*top row*) and normalized electron density distribution (*bottom row*) of the DPPE:GM1 lipid films before (A and A') and at $t_1$ = 5 hours after Gal-1 injection (B, B'), and $t_1$ = 13 hours after Gal-1 injection (C, C'). Measured data is represented as symbols, and lines (solid and dashed) represent fits corresponding to the electron density profiles shown in A', B' and C'. The electron densities $\rho(z)$ are normalized to the electron density of buffer subphase ($\rho_{subphase}$ 0.335 $e^{-}/Å^{-3}$). Error bars for the reflectivity data represent statistical errors in these measurements.

As shown in Figure 6.5, insertion of the lectin induced substantial changes in the reflectivity profiles of the lipid monolayer (Figure 6.5A-C). Not surprisingly, electron density profiles from the model independent fitting of XR data also appeared to undergo significant changes with insertion (solid profiles in Figure 6.5A', 6.5B', and 6.5C'). In order to gain a better physical understanding of structural changes of the DPPE:GM1 monolayer upon interactions with Gal-1, the electron density profiles obtained from the model independent StochFit procedure were de-convoluted into three boxes (or slabs) of constant electron densities (dashed, step-like electron density distributions shown in *bottom row* of Figure 6.5). This the model-dependent fitting of the XR data. Applying roughness (or smearing) to the step-like model-dependent profiles resulted in the electron density distributions (solid black lines in the bottom row) almost indistinguishable from the original distribution from the model independent fits (solid color lines). The new electron density profiles can be used to calculate the XR (dashed lines, *top row*). These new fits, based on only three slabs, differ from model independent fits only at high momentum transfer vectors, $q_z$. Such a simple, but physically reasonable model allows for

better understanding of the evolution of the system and provides a mean to approximate the location of Gal-1 at the interface. As shown in Figure 6.5A', and in agreement with previously published studies (Majewski et al., 2001; Miller et al., 2008; Watkins et al., 2011), the mixed DPPE:GM1 monolayer can be adequately modeled by three slabs - one for the GM1 headgroups and water, one for the mixed DPPE and GM1 headgroup region, and another for the acyl tails of both lipids. The same scheme of slabs were found to adequately model the XR data at both time points after the injection of Gal-1 into the subphase (Figure 6.5B', 6.5C').

A few qualitative observations can be made directly from the reflectivity profiles in Figure 6.5. When the lectin was present in the subphase, the XR interference fringes became less distinguished. This is indicative of an increased disorder (along surface normal) imposed on perfectly aligned DPPE:GM1 monolayer by lectin presence. Electron density profiles of the membrane before and after lectin insertion are overlaid and presented in Figure 6.6A for direct comparison. It is immediately visible that interaction with Gal-1 molecules results in pronounced changes in the electron density distribution across the air-liquid interface. The initial three distinct slabs composed of tails/DPPE:GM1-heads/GM1-heads structure becomes less stratified and more electrons are present towards the air interface, *i.e.* in the alkyl chain region with the addition of Gal-1. Increasing incubation time, and thereby the extent of Gal-1 insertion, resulted in a monotonic increase of the electron density in the lipid tail region (0 to 20 Å from the air interface) and decease in the headgroup regions (approximately 20 to 40 Å towards the liquid subphase). These changes are more apparent when the differences between $t_1$ and $t_2$ electron density profiles and that of the lipids alone are calculated and plotted (Figure 6.6B).

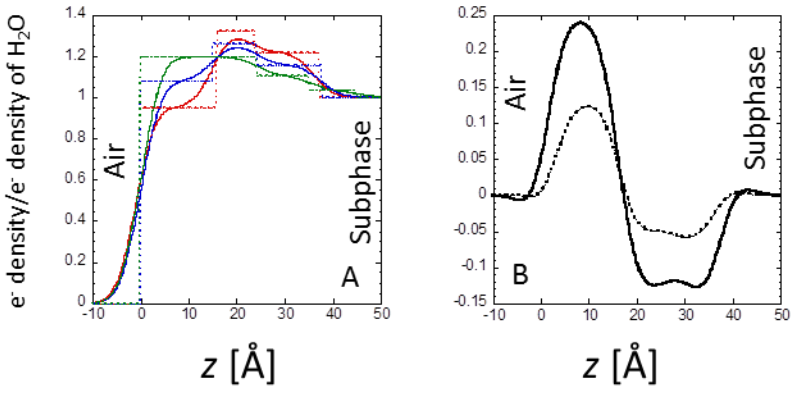


Figure 6.6 Comparison of normalized electron density distribution for

Figure 6.6 illustrates in **A**: Comparison of normalized electron density distribution for DPPE-GM1 monolayer (red) and at $t_1$ = 5 hours (blue) and $t_2$ = 13 hours (green) after Gal-1 injection. Dashed and solid lines represent the electron densities from the three slab model that is un-smeared and smeared, respectively. The electron densities $\rho(z)$ are normalized to the electron density of liquid subphase ($\rho_{subphase}$ 0.335 $e^-/Å^{-3}$). **B**: Differences between the electron density profiles of DPPE:GM1 monolayer and Gal-1 associated lipid monolayer at $t_1$ = 5 hours (dashed line) and $t_2$ = 13 hours (solid line) after Gal-1 injection.

The integration of the area under the step-like profiles (dashed lines in Figure 6.5A', B', and C') provides information on the total number of electrons per $Å^2$ in the footprint of the X-ray beam. Despite the increase of the area per molecule (Figure 6.2B) and therefore decrease in the number of DPPE:GM1 lipids in the footprint of the X-ray beam, the number

of electrons increased from 14.0 $e^-/Å^2$ for DPPE:GM1, to 14.5 and 17.2 $e^-/Å^2$ at $t_1$ = 5 hrs and $t_2$ =13 hrs, respectively. These changes correspond to 4% and 23% increases in the number of electrons. Such enhancement can only be explained by the presence of lectin in the lipid monolayer. When corrected by the 14% and 20% increase in area per molecule due to lectin insertion, the rises in electron density were increased to 19% and 48% at $t_1$ and $t_2$, respectively. Therefore, at the final stage of the measurement ($t$ = 13 hours), 50% electron density increase can be attributed to the presence of Gal-1 in the monolayer.

## 6.4 Conclusions

X-ray scattering data of DPPE–GM1 mixed monolayers at the air–buffer interface before and after injection of lectin have been presented. We studied a 80:20 mol% DPPE:GM1 monolayer before and after injection of solution of 21 μg/ml into the subphase at the constant surface pressure of 20 mN/m and temperature of 20 ºC. Similar to previously published data (Majewski et al., 2001), no phase separation of DPPE and GM1 components or lateral domain formation in these mixtures was detected. The GIXD results indicate that insertion of lectin into the lipid monolayer affects the lipid-ordered (LC) phase of the monolayer, but in a very peculiar way. Upon interaction with Gal-1, the packing arrangement of alkyl chains was only slightly changing (Table 6.1). However, the amount of the LC phase after five hours of incubation first decreased to 35% of the original value, then subsequently increased to 70% after 13 hours of incubation. The oblique 2D unit cell dimensions and size of the crystallite domains of the pure DPPE:GM1 monolayer and at $t$ = 13 hours after Gal-1 injection remained similar. However, for the intermediate time of $t$ = 5 hours, the changes in the packing of the alkyl tails (and overall intensity of the

scattering) were very pronounced and suggest that there might be an initial stage of strong interaction after which the Gal-1 molecules oligomerize, become more soluble and leave the gel phase or, alternatively, assume different conformation *vis-à-vis* the ordered lipids which lead to decreased interactions. The changes in the GIXD pattern indicate that Gal-1 molecules have a tendency to interact with ordered monolayer phase. The average distance between the lipid head groups in the LC phase is approximately 10 Å (twice the value of the 2D cell dimensions, Table 6.1) and the average distance between GM1 headgroups for the 80:20 DPPE:GM1 mixture is ~30 Å. Therefore, it is expected that protein residues separated by such distances will predominantly influence these interactions.

The XR measurements show very pronounced changes in the electron density distribution along the line perpendicular to the monolayer. Prior to injection of Gal-1-containing solution, the electron density distribution obtained from XR measurements shows that the DPPE headgroups and the proximal headgroups of ganglioside GM1 line up in the 2D monolayer plane. The bulkier, branched portion of the pentasaccharide headgroup extends further into the water subphase, minimizing lateral interactions. The ganglioside's sugar headgroup is easily detectable in the reflectivity profiles for $t = 0$ and $t = 5$hours.

Based on the measured electron density distributions (Figure 6.6), there is clear evidence of Gal-1 penetration into the hydrophobic tail region of the lipid monolayer and/or staggering of the headgroups. XR results indicate a significant increase in the number of electrons in the monolayer despite of the increase in area per lipid molecule due to monolayer expansion. The excess of electrons can only be attributed to presence of Gal-1 molecules at the interface. The resulting electron density distributions (Figure 6.6 A, B)

indicate that, along the direction of surface normal, the length scale of ~ 40 Å is affected by the protein. There is also clear evidence that insertion of the Gal-1 is also influencing the hydrophobic portion (alkyl tail region) of the monolayer. Despite a strong impact on electron density distribution of the DPPE:GM1 monolayer by interactions with Gal-1, no clear evidence of location of the molecules in a regular strata below the monolayer was observed. The low $q_{xy}$ GIXD studies did not detect any in-plane ordered structures of *d*-spacings shorter than 120 Å. That indicates no in-plane ordering of Gal-1 into regular 2D arrays. The interaction of Gal-1 and DPPE:GM1 monolayer is very surface pressure dependent. At the pressure of 30 mN/m, we observed no protein insertion into the monolayer.

Contrary to the XR results, the GIXD obtained after 13 hours of Gal-1 incubation showed only small changes in the gel phase of the monolayer. Thus we can deduce that the protein molecules are predominantly interacting with the liquid-expanded phase. This is also supported by the fact that at higher surface pressures (when the amount of the ordered phase is increasing) no evidence of interaction has been observed.

**Acknowledgements**

The Los Alamos Neutron Science Center at the Los Alamos National Laboratory is funded by the US Department of Energy under Contract W-7405-ENG-36. We would also like to acknowledge EC funding (GLYCOPHARM, contract no. 317297), HASYLAB for beamtime and Dr. B. Struth for help with the reflectivity and grazing incidence diffraction experiments.

## 6.5 Supplementary materials

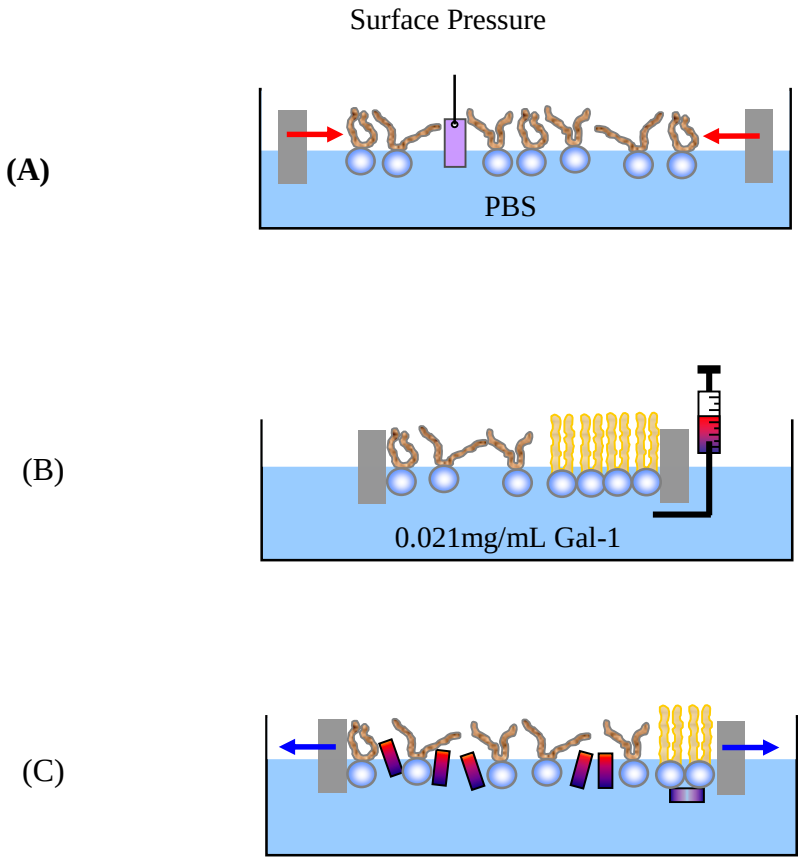


Figure 6.7 Schematics of compression, injection and expansion in trough

**Figure 6.7(A)**: Compression of lipid monolayer to 20 mN/m.

A Wilhelmy plate surface pressure sensor was used to measure the surface pressure ($\pi$) of the lipid monolayer, which is related to the surface tension of the film ($\gamma$) at the air/water interface.

**Figure 6.7(B)**: Injection of Gal-1 into the subphase.

The protein was injected into the subphase underneath the barriers using an L-shaped syringe needle to minimize disturbances to the lipid monolayer.

**Figure 6.7(C)**. Expansion of the lipid monolayer due to the insertion of Gal-1.

Monolayer surface area was recorded and the area expansion was calculated as $\Delta A/A = (A-A_i)/A_i$, where A is the surface area at time t and $A_i$ is the surface area of the monolayer when first compressed to 20 mN/m.

## 6.6 References


Als-Nielsen, J., Jacquemain, D., Kjaer, K., Leveiller, F., Lahav, M., & Leiserowitz, L. (1994a). Principles and applications of grazing incidence X-ray and neutron scattering from ordered molecular monolayers at the air-water interface. *Physics Reports, 246*, 251-313.

Als-Nielsen, J., Jacquemain, D., Kjaer, K., Leveiller, F., Lahav, M., & Leiserowitz, L. (1994b). Principles and applications of grazing incidence X-ray and neutron scattering from ordered molecular monolayers at the air-water interface. *Physics Reports, 246*(5), 251-313.

Als-Nielsen, J., & Kjær, K. (1990). X-ray reflectivity and diffraction studies of liquid surfaces and surfactant monolayers. In T. Riste & D. Sherrington (Eds.), *Phase Transitions in Soft Condensed Matter* (Vol. 211, pp. 113-138): Springer US.

Amano, M., Eriksson, H., Manning, J. C., Detjen, K. M., Andre, S., Nishimura, S., et al. (2012). Tumour suppressor p16(INK4a) - anoikis-favouring decrease in N/O-glycan/cell surface sialylation by down-regulation of enzymes in sialic acid biosynthesis in tandem in a pancreatic carcinoma model. *FEBS J, 279*(21), 4062-4080.

Andre, S., Sanchez-Ruderisch, H., Nakagawa, H., Buchholz, M., Kopitz, J., Forberich, P., et al. (2007). Tumor suppressor p16INK4a--modulator of glycomic profile and galectin-1 expression to increase susceptibility to carbohydrate-dependent induction of anoikis in pancreatic carcinoma cells. *FEBS J, 274*(13), 3233-3256.

Chi, E. Y., Frey, S. L., & Lee, K. Y. C. (2007). Ganglioside GM1-mediated amyloid-beta fibrillogenesis and membrane disruption. *Biochemistry, 46*(7), 1913-1924.

Danauskas, S. M., Li, D., Meron, M., Lin, B., & Lee, K. Y. C. (2008). Stochastic fitting of specular X-ray reflectivity data using StochFit. *Journal of Applied Crystallography, 41*, 1187-1193.

Eisenberger, P., & Marra, W. C. (1981). X-ray diffraction study of the Ge(001) reconstructed surface. *Physical Review Letters, 46*(16), 1081-1084.

Fajka-Boja, R., Blasko, A., Kovacs-Solyom, F., Szebeni, G. J., Toth, G. K., & Monostori, E. (2008). Co-localization of galectin-1 with GM1 ganglioside in the course of its clathrin- and raft-dependent endocytosis. *Cell Mol Life Sci, 65*(16), 2586-2593.

Guinier, A. (1963). *X-ray diffraction in crystals, imperfect crystals, and amorphous bodies*. San Francisco: W. H. Freeman.

Gupta, R. K., Pande, A. H., Gulla, K. C., Gabius, H. J., & Hajela, K. (2006). Carbohydrate-induced modulation of cell membrane. VIII. Agglutination with mammalian lectin galectin-1 increases osmofragility and membrane fluidity of trypsinized erythrocytes. *FEBS Lett, 580*(6), 1691-1695.

He, L., Andre, S., Siebert, H. C., Helmholz, H., Niemeyer, B., & Gabius, H. J. (2003). Detection of ligand- and solvent-induced shape alterations of cell-growth-regulatory human lectin galectin-1 in solution by small angle neutron and x-ray scattering. *Biophys J, 85*(1), 511-524.

Jensen, T. R., & Kjaer, K. (2001). Structural properties and interactions of thin films at the air-liquid interface explored by synchrotron x-ray scattering. In D. Mobius & R. Miller (Eds.), *Novel Methods to Study Interfacial Layers* (Vol. 11, pp. 205-254). Amsterdam: Elsevier Science.

Kaltner, H., & Gabius, H. J. (2012). A toolbox of lectins for translating the sugar code: the galectin network in phylogenesis and tumors. *Histol Histopathol, 27*(4), 397-416.

Kjær, K. (1994). Some simple ideas on x-ray reflection and grazing-incidence diffraction from thin surfactant films. *Physica B: Condensed Matter, 198*(1-3), 100-109.

Kopitz, J. (2009). Glycolipids. In H. J. Gabius (Ed.), *The sugar code : fundamentals of glycosciences* (pp. 177-198). Weinheim; Chichester: Wiley-VCH ; John Wiley [distributor].

Kopitz, J., Ballikaya, S., Andre, S., & Gabius, H. J. (2012). Ganglioside GM1/galectin-dependent growth regulation in human neuroblastoma cells: Special properties of bivalent galectin-4 and significance of linker length for ligand selection. *Neurochem Res, 37*(6), 1267-1276.

Kopitz, J., Bergmann, M., & Gabius, H. J. (2010). How adhesion/growth-regulatory galectins-1 and -3 attain cell specificity: Case study defining their target on neuroblastoma cells (SK-N-MC) and marked affinity regulation by affecting microdomain organization of the membrane. *IUBMB Life, 62*(8), 624-628.

Ledeen, R. W., & Wu, G. (2009). Neurobiology meets glycosciences. In H. J. Gabius (Ed.), *The sugar code : fundamentals of glycosciences* (pp. 495-516). Weinheim; Chichester: Wiley-VCH ; John Wiley [distributor].

Ledeen, R. W., Wu, G., Andre, S., Bleich, D., Huet, G., Kaltner, H., et al. (2012). Beyond glycoproteins as galectin counterreceptors: Tumor-effector T cell growth control via ganglioside GM1 [corrected]. *Ann N Y Acad Sci, 1253*, 206-221.

Lencer, W. I., & Saslowsky, D. (2005). Raft trafficking of AB5 subunit bacterial toxins. *Biochim Biophys Acta, 1746*(3), 314-321.

Majewski, J., Kuhl, T. L., Kjaer, K., & Smith, G. S. (2001). Packing of ganglioside-phospholipid monolayers: An X-ray diffraction and reflectivity study. *Biophysical Journal, 81*(5), 2707-2715.

Majewski, J., Popovitz-Biro, R., Bouwman, W. G., Kjaer, K., Als-Nielsen, J., Lahav, M., et al. (1995). The structural properties of uncompressed crystalline monolayers of

alcohols CnH2n+1 OH (n = 13–31) on water and their role as ice nucleators. *Chemistry – A European Journal, 1*(5), 304-311.

Miller, C. E., Majewski, J., Watkins, E. B., & Kuhl, T. L. (2008). Part I: An X-ray scattering study of cholera toxin penetration and induced phase transformations in lipid membranes. *Biophysical Journal, 95*(2), 629-640.

Miller, C. E., Majewski, J., Watkins, E. B., Weygand, M., & Kuhl, T. L. (2008). Part II: Diffraction from two-dimensional cholera toxin crystals bound to their receptors in a lipid monolayer. *Biophysical Journal, 95*(2), 641-647.

Pontier, S. M., & Schweisguth, F. (2012). Glycosphingolipids in signaling and development: From liposomes to model organisms. *Dev Dyn, 241*(1), 92-106.

Seelig, A. (1987). Local anesthetics and pressure: A comparison of dibucaine binding to lipid monolayers and bilayers. *Biochimica et Biophysica Acta, Biomembranes, 899*, 196-204.

Solis, D., Bovin, N. V., Davis, A. P., Jimenez-Barbero, J., Romero, A., Roy, R., et al. (2014). A guide into glycosciences: How chemistry, biochemistry and biology cooperate to crack the sugar code. *Biochim Biophys Acta*.

Wang, J., Lu, Z. H., Gabius, H. J., Rohowsky-Kochan, C., Ledeen, R. W., & Wu, G. (2009). Cross-linking of GM1 ganglioside by galectin-1 mediates regulatory T cell activity involving TRPC5 channel activation: Possible role in suppressing experimental autoimmune encephalomyelitis. *J Immunol, 182*(7), 4036-4045.

Watkins, E. B., Miller, C. E., Majewski, J., & Kuhl, T. L. (2011). Membrane texture induced by specific protein binding and receptor clustering: active roles for lipids in cellular function. *Proceedings of the National Academy of Sciences, 108*(17), 6975-6980.

Wennekes, T., van den Berg, R. J., Boot, R. G., van der Marel, G. A., Overkleeft, H. S., & Aerts, J. M. (2009). Glycosphingolipids--nature, function, and pharmacological modulation. *Angew Chem Int Ed Engl, 48*(47), 8848-8869.

Wu, G., Lu, Z. H., Gabius, H. J., Ledeen, R. W., & Bleich, D. (2011). Ganglioside GM1 deficiency in effector T cells from NOD mice induces resistance to regulatory T-cell suppression. *Diabetes, 60*(9), 2341-2349.

# CHAPTER 7 CONCLUSIONS AND FUTURE DIRECTIONS

We have gained numerous insights from our studies into the interactions of tau protein and other ampholytic molecules with lipid membranes. We have observed the possible toxicity mechanism of disruption of membranes as well as the templating and misfolding of the agents. These observed mechanisms are consistent with the known toxicity of the ampholytic tau protein's interaction with the lipid membrane. We have learned about the interactions of tau with a variety of interfaces, including the hydrophobic air/water interface and anionic lipid membranes. Significantly, the interaction with the anionic lipid membrane affects both the structure of the tau protein, inducing compaction and misfolding, and the lipid membrane, causing instability and possible permeability. Examination of hyperphosphorylation and domain composition of tau has also yielded promising results, suggesting which domains of the protein are responsible for its abnormal functions.

In the future, further physiologic components such as osmolytes will continue to be added to these models. More complex models that are directly analogous to the *in vivo* cell membrane could, in turn, lead to not only possible treatments and testing for pathologic conditions caused by tau protein aggregation, but also to a better understanding of the physiology of the normal interaction of other intrinsically disordered proteins with the cell membrane. The data which has been collected is also being applied to the creation and validation of computer models of ampholyte/lipid membrane interaction which are currently underway in our laboratory. These computerized models may allow us to gain further understanding of complex interactions that cannot be easily or practically replicated using a physical model.